HUMAN MUSCLE STRUCTURE-FUNCTION RELATION IN-VIVO USING MAGNETIC RESONANCE IMAGING MODALITIES

by

Agah Karakuzu

B. Sc. Biomedical Engineering, Erciyes University, 2013

Submitted to the Institute of Biomedical Engineering
in partial fulfillment of the requirements
for the degree of
Doctor
of
Philosophy

Boğaziçi University
2022

HUMAN MUSCLE STRUCTURE-FUNCTION RELATION IN-VIVO USING MAGNETIC RESONANCE IMAGING MODALITIES

APPROVED BY:

Prof. Dr. Can A. Yücesoy (Thesis Advisor)	.....
Prof. Dr. Cengizhan Öztürk	.....
Prof. Dr. Usha Sinha	.....
Assoc. Prof. Dr. Özgür Kocatürk	.....
Assoc. Prof. Dr. Emine Ülkü Sarıtaş Çukur	.....

DATE OF APPROVAL: 19 September 2022

ACKNOWLEDGMENTS

Dr. Can A. Yücesoy for giving me the opportunity to start my academic career at BME Biomechanics Laboratory in 2013, which was an amazing environment to expose myself to various tasks from academic writing, to designing and conducting MRI experiments, trying to apply for a phase II cllinical trial, or more interestingly, hitting the road at 5am to collect intraoperative data. No matter what the outcome was from these endeavours, I did my best to follow their infamous piece of advice: "don't loose your cool". As the years went by, I came to realize that this applies to the life in general even more than it does to academia, and I believe that I still know where my cool is. Even though we had disagreements from time to time, they all ended up with me admiring their foresight on whatever the issue was. Receiving a pat on the back by Dr. Yücesoy is one of the greatest feelings of accomplishment I had as a graduate researcher, and I hope that this thesis amounts to that.

Uluç Pamuk for being the greatest and the most genius colleague I have ever had on both sides of the Atlantic. I don't think I will ever meet another biomedical researcher who has a background in physics, yet is better than most engineers that I know in solving practical problems. If it was not for Uluç who picked me up among a few canditates applied to work with Dr. Yucesoy, I would end up in a different lab, and probably have a totally different career path that could not lead me to where I am today. If my contributions to science are ever to take the MRI world by the storm, it is his unfathomable wingspan that started it all. Thank you Uluç! I am glad we crossed paths, my dearest labmate forever.

Generations come and generations go, but the legendary BME team remains forever: Bengü Aktaş, Sezin Eren Demirbüken, Gökce Kasacı, Samet Kocatürk, Özgen Özturk Öncel, Öznur Demir Oğuz, Selin Yalvarmış, Arda Arpak, Ahu Nur Türkoğlu, Filiz Ateş, Pınar Öz, Özgür Kaya, Murat Can Mutlu, Mustafa Kemal Ruhi, Murat Tümer and Uluç Pamuk. From 2013 to 2016, those were memorable years we spent

together. Be it at the BME or at the North the 4th. Whenever I listen to the Paradise City by Gun's and Roses, I harken back to the days when South Campus was the definition of its lyrics. We all went separate ways, and that definition was flipped to its antonym with one bad news at a time. I hope one day we will reunite in South Campus to share that heartwarming sense of belonging again, breathing in the athmosphere restored with merit and science by true Bogazici intellects. With these expectations, I dedicate this thesis to my advisor Dr. Yucesoy, to all my professors and dear friends from BME, and to all unforgettable memories whe shared.

Dr. Esin Öztürk Işık for their endless support, wisdom and patience in guiding me through the maze of MRI. Sometimes a few keywords amount to a thousand sentences. "Hidden parameters, Agah, that's the problem", was that key for me, handed out by Dr. Öztürk Işık. I don't know why Dr. Öztürk Işık was not my thesis progress committee member for all these years, but I know that they are an irreplaceable member of my academic progress committee.

Dr. Cengizhan Öztürk, Dr. Özgür Kocatürk and Dr. Burak Acar for sharing their valuable insights and expertise for the progress of this thesis, and Dr. Usha Sinha and Dr. Emine Ülkü Sarıtaş Çukur for agreeing to be on my defense jury.

I am grateful to Drs. Usha and Shantanu sinha for providing 2D VE-PC and 4D CS flow data that finally enabled us to perform a cross-modality validation, which has been a pipedream for many years. I am looking forward to collaborating with their research team in the years to come.

Special thanks go to Arda Arpak for his support in co-processing of the data provided by Drs. Sinha's research team and for eye-opening conversations on demons, I mean the algorithm.

This study was supported by The Scientific and Technological Research Council of Turkey (TÜBİTAK) under grants 111E084 (Can A. Yücesoy), 113S293 (Can A. Yücesoy).

Uluç Pamuk, Arda Arpak, Orkun Akcan, Cemre Su Kaya, Ahu Nur Türkoğlu, Filiz Ateş, Doğukan Ahmet Keleş, Ayça Aklar Çörekçi, Seda Yıldız, Alican Onur Çankaya, Göktuğ Şanlı for being excellent labmates.

Last, but not the least, I want to express my deepest gratitude to my family Çiğdem Karakuzu, Melih Karakuzu, Elif Eda Karakuzu Karacaoğlan for their belief in what I was doing while being away from home, pushing buttons on my keyboard.

ACADEMIC ETHICS AND INTEGRITY STATEMENT

I, Agah Karakuzu hereby certify that I am aware of the Academic Ethics and Integrity Policy issued by the Council of Higher Education (YÖK) and I fully acknowledge all the consequences due to its violation by plagiarism or any other way.

Name :

Signature:

Date:

ABSTRACT

HUMAN MUSCLE STRUCTURE-FUNCTION RELATION IN-VIVO USING MAGNETIC RESONANCE IMAGING MODALITIES

Non-uniform muscle deformation has become a frequent finding in biomechanics research, using imaging modalities operating at different resolution levels from sarcomeres to fascicles. Mainly due to technical limitations, interpretations of these findings are detached from a theoretical foundation that considers the muscle with mechanical links to its surrounding. To enable this vital consideration, this thesis aims at developing and testing the validity of a multimodal MRI method that bridges the understanding between non-uniform mechanical deformations and their myofascial origins, in-vivo. 1) Supplemented with DTI tractography, registration-based fiber direction deformations and principal strains on NVTs characterized the myofascial loads in relation to the strain heterogeneity pattern in active muscle (proximally shortened (up to 22%), distally lengthened (up to 108%) fascicles). Inter-subject deviations from the general pattern were in agreement with subject specific anatomy. 2) A multiverse analysis was performed on the tuning parameters of the demons registration algorithm to assess the validity of strain distribution pattern against algorithmic choices. Results showed that the overall deformation pattern was immune to such perturbations, yet the strains amplitudes underwent significant changes. 3) To add orthogonal information to the myofascial origin assessment and validation of strain distributions, quantitative and velocimetry MRI were used. T1 mapping showed promising results in associating microstructural content with the strain distribution pattern. SR patterns from 2D VE-PC showed weak similarities with registration-based principal strains, whereas those from compressed sensing 4D-PC showed much better agreement. Collectively, these studies show a way forward for the understanding of in-vivo muscle structure function relationship with implications for muscle physiology in health and disease.

Keywords: Magnetic Resonance Imaging (MRI); Diffusion Tensor Imaging (DTI); Myofascial loads; quantitative MRI; Velocimetry; Validation

ÖZET

İNSAN KASININ YAPI VE FONKSİYON İLİŞKİSİNİN MANYETİK REZONANS GÖRÜNTÜLEME MODALİTELERİ KULLANILARAK İN-VIVO DEĞERLENDİRİLMESİ

Çeşitli görüntüleme yontemleri kullanılarak yürütülen biyomekanik çalısmalarda, heterojen gerinim dağılımı yaygın bir bulgu haline gelmiştir. Ancak, bu bulguların yorumlanmasında, kasın çevresi ile olan mekanik bağlantılarını gözeten bir yaklaşım benimsenememektedir. Bu nedenle, mevcut tez çalismasi, heterojen kas deformasyonlarının miyobağdokusal kokenlerini arastırmayı sağlayacak çok modaliteli bir MRG yönteminin geliştirilmesini ve geçerliliğinin test edilmesini hedeflemektedir. 1) DTG traktografisi desteğiyle, görüntü çakistirma temelli fiber yönlü deformasyonlar ve NVY üzerinde hesaplanan hakim gerinimler, miyobağdokusal yükleri gerinim heterojenitesinin örüntüsü dahilinde nitelendirildi (%22'ye varan proksimal kısalma ve %108'e varan distal uzama). Örüntüye uymayan gerinim dağılımlari, NVY'lerin kişisel anatomik farklılıkları ile açıklandı. 2) Gerinim dağılım örüntüsünün geçerliliği, demons görüntü çakıştırma yöntemine ait algoritmik seçimler karşısında çalışıldı. Elde edilen sonuçlar, bu parametrelerin fiber yönlü gerinim örüntüsünün değil; ancak genliklerinin anlamlı bir belirleyeni olduğunu ortaya koydu. 3) T1 haritalama yöntemi, gerinim dağılım örüntüsü ile doku mikroyapisal içerik arasındaki ilintiye cevap teşkil edebilecek bulgular sağladı. 2B velosimetre MRG ile elde edilen gerinim hız haritaları, görüntü çakıstırma temelli gerinimlerle zayıf benzerlik gösterdi; ancak sıkıştırılmış algılama temelli 4B velosimetre ile yapılan karşılaştırmalar daha mukayese edilebilir örüntüler ortaya koydu. Sonuç olarak bu çalısmalar, insan kas yapı ve fonksiyon ilişkisinin anlaşılması icin etkin bir in-vivo yöntem ortaya koymustur. Bu yöntemlerle elde edilecek bulguların, sağlıklı ve patolojik kas fizyolosine yeni bir bakış açısı getirebilecek önemli implikasyonlar sunması beklenmektedir.

Anahtar Sözcükler: Difüzyon Tensör Görüntüleme (DTG); Manyetik Rezonans Görüntüleme (MRG); Miyobağdokusal yükler; Kantitatif MRG; Velosimetre;Validasyon

TABLE OF CONTENTS

ACKNOWLEDGMENTS iii
ACADEMIC ETHICS AND INTEGRITY STATEMENT vi
ABSTRACT vii
ÖZET ix
LIST OF FIGURES xv
LIST OF TABLES xxv
LIST OF SYMBOLS xxvi
LIST OF ABBREVIATIONS xxviii
1. OVERVIEW 1
1.1 Seed, Soil and Force Transmission: A Wholistic Look at the Muscle Function 1
1.2 Non-invasive Musculoskeletal Biomechanics Imaging 5
1.3 Combined MRI-DTI Method for In-Vivo Soft Tissue Mechanics 7
1.3.1 Voxel-wise strain tensor calculation using demons algorithm . . 8
1.3.2 Reconstructing fascicles and probing the tissue microstructure using diffusion imaging 9
1.3.3 Calculation of fiber direction strains 11
1.3.4 Non-rigid registration for tissue morphometry has a track record of accomplishment 12
1.4 Earlier use and success of Demons algorithm in calculating tissue deformations 14
1.5 Aims of the Thesis 17
1.6 Thesis Overview 18
1.6.1 Magnetic resonance and diffusion tensor analyses indicate heterogeneous strains along human medial gastrocnemius fascicles caused by submaximal plantarflexion 18
1.6.2 In-vivo along muscle strain heterogeneity is not affected by image registration parameters: robustness testing of combined magnetic resonance and diffusion tensor imaging method 19

1.6.3 Velocimetry and quantitative MRI for cross-validation, generalizability and microstructural origin assessment of fiber direction strains as calculated by demons non-rigid registration 19
1.7 List of Publications Produced From the Thesis 20
1.7.1 Journal publications 20
1.7.1.1 First author 20
1.7.1.2 Not first author 20
1.7.2 Conference Proceedings 21
1.7.2.1 First author 21
1.7.2.2 Not first author 22
2. MAGNETIC RESONANCE AND DIFFUSION TENSOR IMAGING ANALYSES INDICATE HETEROGENEOUS STRAINS ALONG HUMAN MEDIAL GASTROCNEMIUS FASCICLES CAUSED BY SUBMAXIMAL PLANTARFLEXION ACTIVITY 25
2.1 Introduction 25
2.2 Methods 27
2.2.1 Subjects 27
2.2.2 Experimental protocol and image acquisition 27
2.2.3 Calculation of deformations 30
2.2.4 Estimation of errors and repeatability 32
2.2.4.1 Strain artifacts caused by hardware-based noise 32
2.2.4.2 Test-retest repeatability 32
2.2.4.3 Error strains caused by the algorithm 33
2.2.4.4 Statistics 33
2.3 Results 33
2.4 Discussion 40
3. IN-VIVO ALONG MUSCLE FASCICLE STRAIN HETEROGENEITY IS NOT AFFECTED BY IMAGE REGISTRATION PARAMETERS: ROBUSTNESS TESTING OF COMBINED MAGNETIC RESONANCE-DIFFUSION TENSOR IMAGING METHOD 45
3.1 Introduction 45
3.2 Methods 48

3.2.1 Parameter analysis using the reference data 48
3.2.2 Data analysis workflow 49
3.2.3 Statistical analyses 50
3.2.3.1 Median fiber direction strains at different muscle parts 50
3.2.3.2 Preprocessing 50
3.2.3.3 Ridgeline kernel density plots 51
3.2.3.4 Hierarchical shift function analysis 51
3.2.3.5 Number of significantly different pair-wise comparisons 51
3.2.3.6 Reproducibility 52
3.3 Results 52
3.4 Discussion 62
3.4.1 Effects of employing different data analysis workflows 62
3.4.2 General effects of tuning parameters on strain amplitudes 63
3.4.3 Effects of tuning parameters on strain distribution pattern . . . 65
3.4.4 Biomechanical mechanism and implications of muscle fiber direction strain heterogeneity 66
3.5 Conclusion 67
4. VELOCIMETRY AND QUANTITATIVE MRI FOR CROSS-VALIDATION, GENERALIZABILITY AND MICROSTRUCTURAL ORIGIN ASSESSMENT OF FIBER DIRECTION STRAINS AS CALCULATED BY DEMONS NON-RIGID REGISTRATION 69
4.1 Introduction 69
4.1.1 Supplementing in-vivo mechanical analyses with qMRI 71
4.1.1.1 Relaxometry imaging 72
4.1.1.2 Diffusion imaging 73
4.1.1.3 Magnetization transfer imaging 74
4.2 Methods 76
4.2.1 Data acquisition 76
4.2.2 Data processing 83
4.3 Results 84
4.3.1 Generalizability and qMRI experiment 84
4.3.2 Velocimetry experiment 91

4.4 Discussion 96
4.4.1 Generalizability and qMRI experiment 96
4.4.2 Velocimetry experiment 98
5. GENERAL DISCUSSION 102
APPENDIX A. MAGNETIC RESONANCE AND DIFFUSION TENSOR IMAGING ANALYSES INDICATE HETEROGENEOUS STRAINS ALONG HUMAN MEDIAL GASTROCNEMIUS FASCICLES CAUSED BY SUBMAXIMAL PLANTARFLEXION ACTIVITY 103
A.0.1 Mean fiber direction strains of different tracts and its relevance 103
APPENDIX B. IN-VIVO ALONG MUSCLE FASCICLE STRAIN HETEROGENEITY IS NOT AFFECTED BY IMAGE REGISTRATION PARAMETERS: ROBUSTNESS TESTING OF COMBINED MAGNETIC RESONANCE-DIFFUSION TENSOR IMAGING METHOD 105
APPENDIX C. VELOCIMETRY AND QUANTITATIVE MRI FOR CROSS VALIDATION AND MICROSTRUCTURAL ORIGIN ASSESSMENT OF FIBER DIRECTION STRAINS AS CALCULATED BY DEMONS NON RIGID REGISTRATION 106
C.1 Generalizability and qMRI experiment 107
C.2 Velocimetry experiment 108
C.2.1 On the difference between VE-PC strain rates and registration-based strains 108
REFERENCES 112

LIST OF FIGURES

Figure 1.1 Schematic illustration of the combined MRI-DRTI method to calculate fiber direction strain distributions, exemplifying the deformation in passive medial gastrocnemius (GM) muscle between flexed (undeformed) and extended (deformed) knee joint configurationss. 7

Figure 1.2 Diffusion Tensor Imaging (DTI) tractography of human medial gastrocnemius (GM) muscle. a) GM fascicles (red) are visualized within the reconstructed surface mesd model (gray) of the muscle. b) Spatial distribution of nodal fractional anisotropy (FA) values. c) Coronal anatomical image showing the crossection of the FA-mapped GM fascicles. 10

Figure 2.1 (a) Subject position in the undeformed (relaxed) and deformed (15% MVC) states was constant. The body was positioned prone on the patient table in the bore of the MRI machine. A custom made MRI compatible fixation device was used to fix the ankle angle at 90°. The foot pedal located in this device is equipped with an MRI compatible dynamometer (Biopac TSD121B-MRI, CA, USA) to measure the MVC level during scanning. An MRI compatible monitor allowed subjects to adjust and maintain activation at the target level. A piece of Velcro under the heel and strapping over the ankle allowed ?xation of the ankle angle. To locate the knee joint in extended position, a piece of Velcro was attached to the patella and a corresponding piece of Velcro was placed on the MRI table. (b) A sagittal-oblique anatomical MR image, aligned with the longitudinal axis of the GM (indicated in turquoise). (c) A matching diffusion weighted image (DWI) set is superimposed semi-transparently on the corresponding position of the GM. The region between the white dashed lines marks the longitudinal boundaries of the collected DWI. (d) The tracked GM fascicles (indicated in black) in the section considered are shown. 29

Figure 2.2 Fiber direction strain distributions occurring due to the original (a), and the repeat (b) protocols. The left panels show the anterior and the right panels show the posterior view of the tracked GM fascicles. The GM volume studied was divided into ten muscle parts (P4-1, M1-2 and D1-4) per each 10% volume along the proximo-distal length. These muscle parts are indicated using dotted lines, where P4, D4 and M1-2 represent the most proximal distal and mid parts, respectively. 35

Figure 2.3 Box and whisker plots for (a) error strains and (b) strains along the GM fibers caused by 15% MVC effort. The horizontal line inside each box represents the median strain value; the upper and lower edges of each box itself represent upper and lower quartiles respectively (i.e., the 75th and 25th percentiles), and lines extending from each end of the box (whiskers) indicate the peak values of the principal strains plotted. (c) Distribution of fiber direction strains of different nodes for the pooled data from all subjects. 36

Figure 2.4 Effects of 15% MVC isometric submaximal plantar-flexion activity on GM fascicles and neurovascular tracts for subjects A-C. Fiber direction strain values are mapped on tracked GM fascicles (the leftmost and mid panels show the anterior, and the rightmost panel shows the posterior view) per subject. The mid and the rightmost panels also show the superficial (dark gray) and deep (light gray) NVTs and the continuity of these structures with the GM tissues. The intersections of the NVTs with the GM fascicles are highlighted. The insets (dashed boxes) focus on muscle regions showing high fiber direction strain amplitudes indicating fascicle lengthening. The first principal strains calculated for those NVT sites are visualized using glyphs to indicate presence of myofascial loads. The direction of each glyph is determined by the corresponding Eigen vector. The length of each glyph is proportional to the size of local peak strain. The larger color bars on the left report the fiber direction strains and the smaller ones on the right reports the first principal strains on the NVT structures per subject. 38

Figure 2.5 Effects of 15% MVC isometric submaximal plantar-flexion activity on GM fascicles and neurovascular tracts for subjects D-E. Fiber direction strain values are mapped on tracked GM fascicles (the leftmost and mid panels show the anterior, and the rightmost panel shows the posterior view) per subject. The mid and the rightmost panels also show the superficial (dark gray) and deep (light gray) NVTs and the continuity of these structures with the GM tissues. The intersections of the NVTs with the GM fascicles are highlighted. The insets (dashed boxes) focus on muscle regions showing high fiber direction strain amplitudes indicating fascicle lengthening. The first principal strains calculated for those NVT sites are visualized using glyphs to indicate presence of myofascial loads. The direction of each glyph is determined by the corresponding Eigen vector. The length of each glyph is proportional to the size of local peak strain. The larger color bars on the left report the fiber direction strains and the smaller ones on the right reports the first principal strains on the NVT structures per subject. 39

Figure 3.1 Serial distribution of local fiber direction strains (ε) along tracked fascicles of the medial gastrocnemius (GM) on knee extension are visualized across participants (participants A-E, rows) and for tuning parameters where α equals σ ($C^{\alpha=\sigma}$, columns). Horizontal color-bars show min-max (turquoise), range (white) and zero-crossing (yellow) of the respective ε distributions. Dashed white lines indicate 10 muscle parts along with corresponding tags and categorical color palettes. 53

Figure 3.2 Annotated heatmaps plot median fiber direction strain values at each muscle part ($\tilde{\varepsilon}_{part}^{\langle\alpha,\sigma\rangle}$) across all tuning parameter configurations ($C^{\langle\alpha,\sigma\rangle}$, columns). The color scales are adjusted independently per tuning parameter combination to inspect the consistency of proximo-distal $\tilde{\varepsilon}_{part}^{\langle\alpha,\sigma\rangle}$ patterns against parameter changes. The $C^{\alpha=\sigma}$ pairs are indicated by white quotation marks for the reader's convenience. 55

Figure 3.3 Kernel density ridgeline plots of modified z-score distributions across all the tuning parameter combinations ($z^{\langle\alpha,\sigma\rangle}$) are displayed for the P4, M1, and D4 muscle parts (rows) of the participants B-D (columns). The horizontal axis limits of each panel are determined individually by the min-max across all the density plots. 56

Figure 3.4 Number of significant post-hoc comparisons across muscle parts are shown for the tuning parameter combinations as annotated heatmaps per participant. The color scales are adjusted to min-max of 0-9, as the maximum possible number of significant post-hoc differences for 10 groups is 9 (i.e., one muscle part can be significantly different than all the remaining 9 muscle parts at the most). 57

Figure 3.5 Steps of hierarchical shift function (HSF) analysis illustrated for the difference between $C^{\langle 4,4\rangle}$ and $C^{\langle 10,10\rangle}$ in participant C: (a) An individual shift function (SF) of muscle part D4 (right) is constructed based on the quantile differences (yellow circles) in association with the location of compared quantile pairs (beige bars) in $z_{D4}^{\langle 4,4\rangle}$ and $z_{D4}^{\langle 10,10\rangle}$ distributions (green swarmplots). (b) Individual SFs are constructed for each muscle part and overlaid by vertically aligning their quantile differences (right). The quantile difference at q5 approximately equals to the difference between $z_{part}^{\langle 4,4\rangle}$ and $z_{part}^{\langle 10,10\rangle}$ (left) for a given muscle part. (c) Fishbone plot showing muscle part comparisons by white circles at (20% trimmed) means of quantile differences and confidence intervals of the corresponding one-sample t-test. 59

Figure 3.6 Hierarchical shift function (HSF) plots are shown for the differences between the binary pairings of modified z-score distributions where α equals σ (rows) per participant (columns). Panels contain 10 colored shift functions (SF), one for every muscle part. Each SF is plotted by the quantile differences of compared tuning parameter pairs ($z_{1st}^{\alpha=\sigma}$ - $z_{2nd}^{\alpha=\sigma}$) against the quantiles of the first pair ($z_{1st}^{\alpha=\sigma}$). The bold white SF outlines the quantile differences in muscle parts by trimmed means (white markers) and confidence intervals (CI). The y-axis limits are the same (from -3 to 3) to allow easy visual comparison across the panels. Inclusion of the null value of 0 in a CI indicates no significant effect for the respective decile differences. 61

Figure 4.1 Sagittal plane images from 3D volumes acquired using different sequences and by altering specific parameters for the qMRI experiement. Inset figure (upper right) shows the relation between input/output data and respective information for each image by their placement on the layout. 78

Figure 4.2 Schematic illustration of the data structure acquired for the cross-modality validation of the demons-generated-strain distribution. a) Velocity-encoded phase-contrast (VE-PC) data acquired during repetitive 15% MVC isometric plantarflexion. b) Undeformed (relaxed) and deformed (15% MVC sustained isometric plantarflexion) high-resolution anatomical datasets acquired using 3D spoiled gradient-echo (SPGR) sequence. 81

Figure 4.3 Medial gastrocnemius (GM) muscle fibers reconstructed using new acquisition parameters and tractography pipeline. Densely packed streamlines are representative of the muscle structure and present across the longitudinal coverage of the FOV of diffusion weighted volume. Tracts were transparently colored at random to provide a better sense of orientation. 85

Figure 4.4 Serial fiber direction strains are visualized on the tracked fascicles of the medial gastrocnemius (GM) muscle for paired alpha (rows) and sigma (columns) combinations. 86

Figure 4.5 Lower triangle: Scatter plots for the paired alpha-sigma combinations ($C^{\langle\alpha,\sigma\rangle} \mid \forall_{\alpha=\sigma} \in \{4,6,8,10\}$) of mean fiber direction strains ($\bar{\varepsilon_f}$). Pairs underwent at least one sign swap among these pairs are shown by yellow markers, green otherwise. Upper triangle: Shift function plots for the same alpha-sigma combinations are given in the lower triangle. These plots show 9 markers to represent intervals from 10 deciles. Horizontal axis gives the first pair, whereas vertical axis represents differences between the deciles of pairs. Vertical lines crossing each marker represent confidence intervals (CI) of the respective decile. Inclusion of zero (horizontal dashed line) indicates that the compared deciles are not significantly different (green). Significantly different deciles are indicated by yellow vertical line. Note that distributions are z-score normalized. Therefore 5th marker from the beginning corresponds to the mean decile. Remaining markers to its right and left represent strain deciles above and below the mean decile. 87

Figure 4.6 Heatmap of the normalized mean squared errors calculated between the registered (transformed undeformed state) image and the deformed state image for all parameter combinations. 88

Figure 4.7 An axial slice of the quantitative T1, MTR and MTsat maps. 89

Figure 4.8 Serial and mean distributions of fiber direction strains (obtained at $C^{\langle 6,6 \rangle}$), T1, magnetization transfer saturation index (MTsat) and radial diffusivity (RD). 90

Figure 4.9 Positive eigenvalues of the strain rate tensor plotted throughout the contraction cycle (22 frames) at the proximal (red), medial (green) and distal (blue) regions of the medial gastrocnemius. Negative eigenvalues (SR_{fiber}) upon plantarflexion are shown (top row) for 8 out of 22 frames, corresponding to the contraction phase (approximately from 3th to the 10th frame). 91

Figure 4.10 Positive eigenvalues of the strain rate tensor plotted throughout the imaging cycle (22 frames) at the proximal (red), medial (green) and distal (blue) regions of the medial gastrocnemius. Positive eigenvalues ($SR_{in-plane}$) upon plantarflexion are shown (top row) for 8 out of 22 frames, corresponding to the contraction phase (approximately from 3th to the 10th frame). 92

Figure 4.11 Side-by-side comparison of (left) the negative eigenvalue map of the SR (SR_{fiber}) from 2D VE-PC (the peak plantarflexion phase of cyclic 15% isometric contraction) and (right) third principal strains calculated from the non-rigid demons registration of 3D SPGR images (relaxed vs on sustained 15% isometric plantarflexion). Note that the slice location of the demons-based strain map (right) was set manually to mimic that of VE-PC. 93

Figure 4.12 Side-by-side comparison of (left) the positive eigenvalue map of the SR ($SR_{in-plane}$) from 2D VE-PC (the peak plantarflexion phase of cyclic 15% isometric contraction) and (right) first principal strains calculated from the non-rigid demons registration of 3D SPGR images (relaxed vs on sustained 15% isometric plantarflexion). Note that the slice location of the demons-based strain map (right) was set manually to mimic that of VE-PC. 94

Figure 4.13 Comparison of deformation patterns between highly accelerated 4D compressed sensing (CS) flow acquisition and demons-based strains. a) Negative eigenvalue map of the SR (SR_{fiber}) and b) Negative eigenvalue map ($SR_{in-plane}$) from 4D CS PC. c) Third and d) first principal strains from demons-based strain quantification. 95

Figure 4.14 Comparison of 4D compressed sensing (CS) flow magnitude reconstructed image (left, 2x2x5mm) and turboFLASH T1w high-resolution (right, 1mm iso) images. 100

Figure A.1 Parallel distribution of fiber direction strains for each subject. Mean fiber direction strains of different tracts are mapped on a reference cross-sectional slice separately for each subject. The reference slice is chosen so as to maximize the fiber representation within the muscle cross section. Negative values represent shortening and positive values represent lengthening. Strain limits are not normalized to reflect individual parallel distribution differences. 104

Figure B.1 hjgfd 105

Figure C.1 Split-violin plot matrix visualizing the serial fiber direction shortening (red) and lengthening (turquoise) distributions yielded by paired alpha (rows) and sigma (columns) combinations. Suspected outliers (1.5 interquartile range far from the median) were represented by markers, whereas outliers were discarded from violin plots. 107

Figure C.2 (a) Box and whisker plots for magnetization transfer ratio (MTR) distribution in medial gastrocnemius (GM), lateral gastrocnemius (GL), soleus (SOL), tibialis anterior (TA) and peroneus (PER) muscles. (b) Axial cross-section of MTR map. (c) Region of interest (ROI) masks. Small interquartile ranges indicate low variability in the distribution of MTR vales in axial cross-sections for all ROIs. All target muscles appear to have a quite similar mean MTR value with noticeable number of outliers. 108

Figure C.3 Illustration of the difference between Lagrangian and Eulerian mesh descriptions. In Lagrangian coordinates, the relative position of material points (blue dots) remain stationary against the grid locations (black dots on the mesh) as the material deforms. In other words, the material coordinates are fixed, the mesh deforms with the material. In Eulerian coordinates, the material coordinates (blue dots) change in time, whereas the grid locations (black dots) remain constant. 110

LIST OF TABLES

Table 2.1	Anthropometric Data	27
Table 2.2	MR and DT imaging parameters.	30
Table 2.3	Fiber direction strains (mean ± SD) in different muscle parts for the repeatability test.	34
Table 2.4	Fiber direction strains (mean ± SD) in different muscle parts.	37
Table 4.1	Acquisition parameters for the generalizability and qMRI experiment including structural and difusion-weighted sequences.	79
Table 4.2	Acquisition parameters for the generalizability and qMRI experiment including field mapping.	80
Table 4.3	Acquisition parameters for the 2D VE-PC sequence.	82
Table 4.4	Acquisition parameters for the 4D compressed-sensing (CS) PC sequence.	82
Table 4.5	Descriptive statistics (mean±SD) for the quantitative MRI parameters (T1, MTsat and MTR) are given for lower leg muscles of gastrocnemius medialis and lateralis (GM, GL), soleus (SOL), tibialis anterior (TA) and peroneus (PER).	89
Table 4.6	Standardized beta coefficients (β) and standard errors (SE) from the multiple linear analysis to test the predictive effect of the quantitative MRI parameters over the mean fiber direction lengthening ($\bar{\varepsilon_{f+}}$) and shortening ($\bar{\varepsilon_{f-}}$).	90

LIST OF SYMBOLS

T	Tesla
Hz	Hertz
cm	centimeter
mm	millimeter
mm^2	square millimeter
mm^3	cubic millimeter
μm	micrometer
s	second
kg	kilogram
$^\circ$	degree
v_{enc}	velocity encoding
$\otimes$	cross-product
N	Newton
I	unit tensor
F	deformation gradient tensor
E	strain tensor
E_1	first principal strain
E_3	third principal strain
V	volume
dV, ΔV	volume change
L_{opt}	optimum muscle length
CI	confidence interval
α	demons algorithm's normalization factor
σ	standard deviation of the demons smoothing kernel
z	modified z-score
ε	fiber direction strain
q_n	the nth quartile of a statistical distribution
$C^{\langle\alpha,\sigma\rangle}$	tuning parameter configuration for a given α and σ

$C^{\alpha=\sigma}$	tuning parameter configuration where α equals σ
$\tilde{\varepsilon}_{part}^{\langle\alpha,\sigma\rangle}$	median fiber direction strain for a given α and σ
$z_{part}^{\langle\alpha,\sigma\rangle}$	modified z-score distribution for a given α and σ
$z_{part}^{\alpha=\sigma}$	modified z-score distribution where α equals σ
J	Jacobian determinant
B_1	RF transmit field
π	pi
ϵ	strain
ϵ_f	along-fiber strain

LIST OF ABBREVIATIONS

EMFT	Epimuscular Myofascial Force Transmission
MRI	Magnetic Resonance Imaging
qMRI	Quantitative Magnetic Resonance Imaging
DTI	Diffusion Tensor Imaging
DWI	Diffusion Weighted Imaging
FEM	Finite Element Modeling
LFMM	Linked Fiber-Matrix Mesh
MTJ	MyoTendinous Junction
KT	Kinesio Tape
ECM	Extra-Cellular Matrix
CV	Coefficient of Variation
CS	Compressed Sensing
EDL	Extensor Digitorum Longus muscle
GM	Gastrocnemius muscle Medial head
SOL	Soleus muscle
TA	Tibialis Anterior muscle
MVC	Maximum Voluntary Contraction
PC	Phase-Contrast
MRA	Magnetic Resonance Angiography
DENSE	Displacement ENcoding with Stimulated Echoes
Turbo FLASH	Turbo Fast Low-Angle Shot
ss-EPI	single shot-Echo Planar Imaging
FA	Fractional Anisotropy
RD	Radial Diffusivity
MT	Magnetization Transfer
MTR	Magnetization Transfer Ratio
MTsat	Magnetization Saturation Index
qMT	Quantitative Magnetization Transfer

T1	Longitudinal Relaxation Time Constant
T2	Transverse Relaxation Time Constant
SR	Strain Rate
2D	Two-Dimensional
3D	Three-Dimensional
SD	Standard Deviation
NVT	Neuro-Vascular Tract
US	UltraSound

1. OVERVIEW

1.1 Seed, Soil and Force Transmission: A Wholistic Look at the Muscle Function

The views on how in-vivo musculoskeletal force is transmitted to determine the muscle function draw surprisingly close parallels to the hypotheses that shaped the modern research methods in cancer treatment. Regarded as one of the most outstanding scientific concepts, the cancer seed and soil hypothesis nicely captures some of the key aspects of considering skeletal muscles within their surroundings to understand how they function, namely epimuscular myofascial force transmission (EMFT) [2]. As the seed and soil hypothesis predates the EMFT by over a century and its implications have already been widely established in developing treatment strategies [3], this section will start with a brief look at its concept.

The paradigm shift in cancer metastasis research started in 1889 with the postulation of the seed and soil hypothesis by Stephen Paget [4]. In hindsight, the key argument of this seminal hypothesis appears too reasonable to be flouted: the biologic events involved in the spread of malignancy does not take place at random, instead they are determined by a unique interaction between the tumor ("the seed") and organ microenvironments ("the soil"). On the other hand, the traditional approach to metastasis research was focused merely on the seed to explain why they proliferate in multiple locations. Given that seeds necessitate an arable soil for growth, de-linking them from where they naturally exist (i.e., studying the cancer cells in isolation) missed out on crucial information in a life-or-death race against the clock. Unfortunately, this traditional approach remained as mainstay of the cancer research, until the seed and soil hypothesis was challenged by Ewing in 1928.

Offering a coarser explanation, the anatomical/mechanical hypothesis attributed the metastasis on the organization of the circulatory structures and the rate in which the organs were hit by cancerous cells traveling within the vascular and lymphatic pathways [5]. As an epitome of the importance of having competing hypothesis on the scientific progress, Ewing's explanations triggered a wave of research on this matter. Soon later, several studies presented strong sevidence in support of the seed and soil hypothesis [6, 7], highlighting that what is considered as random biological processes are highly likely to be complex effect mechanisms we simply fail to understand. This realization has set the cancer research on a new course.

Today's modern oncology does not regard these hypotheses as mutually exclusive: anatomical structures responsible for circulation indeed play an important role in the transportation of malignancy to the remote organs, yet the growth of metastasis eventually comes down to the interaction between the cancerous tissue and organ microenvironments [5]. The recent consensus is that the relationship between the function and structure prevails in a continuum of scales, and the complex interaction between the tumor and its environment does determine the characteristics of the metastasis. In other words, the seed should be studied in presence of its soil (Paget) without overlooking the importance of the larger landscape structures that intrinsically function to supply them (Ewing).

Like the anatomical/mechanical view on cancer metastasis, the classical approach to musculoskeletal biomechanics argues that the force generated by sarcomeres (the seed) is transmitted to the bones solely by myotendinous pathways. This considers skeletal muscles as independent mechanical actuators that are isolated from their surroundings. Even though myotendinous pathways carry over considerable portion of the generated force to the joints, ascribing muscle function only to a mechanical equilibrium between the muscle and tendinous structures is an oversimplification. As a result, this view assumes that skeletal muscle undergoes uniform length changes with equal amount force transmitted to both ends [8].

In-vivo muscle operates within a fascial integral system in which the collagenous

network is tied together continuously at all levels (the soil). The epimysia of adjacent muscles are linked [9]. Furthermore, collagen reinforced neurovascular tracts (NVT) are also continuous with this network that links neighboring and distant muscles, allowing direct intermuscular interactions [10, 11]. Not only muscular, but also non-muscular structures have also been shown to provide a pathway for force transmission [12]. The transmission of the force via these structures (e.g. intermuscular septum, interosseal membrane and bones) is described as extramuscular force transmission. Finally, mechanical loads exerted by both inter- and extramuscular mechanical interactions can be transmitted inside of the muscle, as the muscle fibers are connected to the fascial integrity via the extracellular matrix (ECM), along their full peripheral surface [13]. As a result, inter- and extramuscular mechanical interactions can alter the force balance within the muscle fibers, collectively defined as EMFT [2].

To address the effects of EMFT on muscle function, many studies were carried out using finite element modeling, animal experiments and intraoperative experiments. Several studies were carried out using a finite element model [14], which is specifically designed to study mechanical interactions between muscle fiber and ECM domains. These theoretical studies focused on the effect of both isolated and combined epimuscular connections during activation in altered muscle lengths [15, 16, 17], muscle relative position change [15], surgical procedures [18], and botolinum-toxin (BTX) application [19, 20]. Results from in-situ animal experiments [17, 20] were in good agreement with those from modeling studies, implying heterogeneous sarcomere length distribution. Clinically highly relevant findings from intraoperative experiments with spastic cerebral palsy patients revealed that spastic muscle can show normal mechanics and epimuscular interactions have a critical role in the determination of the impeded joint range of force exertion [21]. Collectively, all these studies indicate that EMFT has major effects on the muscle function.

Being guided by the history of cancer research summarized above, overlooking the importance of the EMFT (i.e., the importance of the soil) for in-vivo muscle function is more likely to slown down the development of effective treatment strategies for musculoskeletal diseases rather than being helpful for advancing our understand-

ing. For example, in the treatment of spastic muscle, widely adopted methods include BTX administration and surgical procedures such as myotomy. These approaches are based on killing the seed, i.e., incapacitating the force production of the sarcomeres. Interestingly, both methods have been shown to have unintented downstream [22] or longitudinal effects [23]. On the other hand, animal studies have demonstrated that disturbing the soil, i.e., modifying the extramuscular connections of a skeletal muscle can notably reduce muscle's undesired contribution to the joint torque with more precise targeting [24] Nevertheless, the potential practical outcomes are yet to be realized in clinical settings. Another important example is the assumptions on the inner workings of the sarcomere. Although it has been long accepted that the active muscle force emerges from actin and myosin myofilaments sliding past each other depending on the cytosolic levels of calcium [25, 26], a recent body of studies have reported that the titin is also involved in the force regulation due to its calcium-dependent mechanical properties [27, 28, 29, 30, 31, 32, 33]. Incorporating this three-filament paradigm of muscle contraction into a linked fiber-matrix mesh FEM, it has been shown that active state titin restricts the sarcomere lengthing nonuniformly within a fascicle [34]. Coupled with the contributions from myofascial loading, the eventual non-uniform sarcomere length distribution becomes a primary determinant of muscle's length of force generation [35].

Nevertheless, conveying consistent research that examines the skeletal muscle without de-linking it from its in-vivo surroundings comes with its own set of technical challenges. This is mostly because the measurement methods typically call for interfering with the integrity of a targeted muscle or muscle groups. Fortunately, magnetic resonance imaging (MRI) offers a powerful non-invasive method to study in-vivo muscle in a decently large field-of-view, with the added benefits of an arsenal of contrasts mechanisms that can inform us about the structure, kinetic and mechanical properties, and even about tissue microstructure. The following section provides a brief overview on the use of MRI in the study of musculoskeletal biomechanics.

1.2 Non-invasive Musculoskeletal Biomechanics Imaging

Principal advances in studying in-vivo musculoskeletal biomechanics have come in the fields of ultrasound (US) and magnetic resonance imaging (MRI). Recent developments in US have mostly focused on the real-time quantification of tissue stiffness. Exploiting the use of propagation of shearwaves in soft tissue, ultasonographic fast measurements can give a measure of tissue stiffness in terms of shear wave velocity [36]. For example, this technique was utilized to study association between the tissue stiffness and activation level [37]. In addition to US, MRI has also ability to perform elastographic measurements with the help of an external mechanical perturbation of the target tissue [38]. On the other hand, recent multi-parametric quantitative MRI applications those aiming at in-vivo histology provide even more intriguing measurements, such as the determination of macromolecular content. In the last year, different combinations of diffusion and quantitative MRI techniques have been employed in an attempt to quantify collagen content in eye [39], breast [40], cortical bone and tendon [41] and cartilage [42]. Although such techniques are not applied on skeletal muscle yet, future research is warranted in the determination of in-vivo collagen content in muscular structures.

The appeal of the forthright measurement of in-vivo mechanical properties and structural content of the skeletal muscle is obvious. However, a complete assessment further requires in-vivo quantification of architectural parameters and deformation characteristics. Fortunately, there are tailored MRI and US techniques available to satisfy this requirement. Planar sonographic measurements were commonly taken as a basis to calculate fiber length, curvature and pennation angle in various passive and active conditions [43, 44, 45, 46]. Such measurements become more even popular during the following years, emphasizing the importance of a non-invasive quantification in evaluating muscle function. A decade later, Bojsen-Moller et al. have presented a novel approach by calculating relative displacements between the triceps surae muscles upon the changes in knee joint angle and selective stimulation [47, 48]. They showed evidence for the presence of a differential displacement between the Soleus and Gastrocnemius muscles, raising a question concerning the efficiency of 2D US measurements. Despite

the accepted validity of such measurements in biomechanical imaging [31], Rana et al have shown that planar measures can hardly be regarded as an assured basis for a comprehensive estimation of in-vivo muscle mechanics [49]. Their findings from 3D US reconstructions have shown that the majority of the previous US measurements have missed out highly critical mechanical interactions.

MRI on the other hand, enables multiplanar data acquisition with superior soft tissue contrasts and without the need for repositioning. Therefore, it is highly suitable for encoding soft tissue motions that cannot be captured by US in all spatial dimensions, which opens the way for volumetric quantification of strain. Tissue displacement in MRI is resolved by velocimetry encoding based approaches, which are spin tagging (e.g. displacement encoded stimulated echoes, (DENSE)) and phase contrast (PC) techniques. Spin tagging methods track the signal voids occurring due to tissue motion on the prescribed grid locations and provide displacement information at those labeled points. This data can be used with respect to the muscle deformation [50]. The PC technique provides velocity information for each voxel in the field of view [51], which makes it possible to quantify 3D displacements on a single plane. Nevertheless, with the advent of highly-undersampled non-cartesian acquisition and reconstruction methods [52, 53], it has become possible to study muscle contraction using 3D time-resolved velocity-encoded PC data [54]. Nearly a fourfold reduction in scan time has enabled the study of muscle activation under higher maximum voluntary contraction (MVC) than ever before, as it requires a considerably less number of consistent contractions [55]. In that study, Malis et al. (2020) have reported non-uniform strain rate distribution along the muscle fiber direction in triceps surate muscles at varying MVC, resolved across 50 temporal frames of the isometric contraction-relaxation cycle [56]. This opens a whole new avenue for using MRI in new experimental settings by tapping into the tradeoff between the high spatial and temporal resolution, such as monitoring muscle motion on nerve stimulation and in-vivo characterization of the force-strain temporal correlation patterns [55]. Given that it is less demanding on the MVC, accelerated acquisition expands the research gamut of musculoskeletal pathologies to recruit the patients who cannot sustain higher levels of muscle activity (e.g., Duchenne muscular dystrophy).

Despite these recent advancements, applications of the velocimetry techniques still remain peculiar to certain experimental (e.g., dynamic) conditions in musculoskeletal research. In addition, such advanced acquisition sequences are not easily available to the most imaging sites. On the other hand, deformable image registration techniques offer a more accessible means to quantify deformation between deformed and undeformed anatomical image sets that are not necessarily captured during muscle activation [57]. Forming the foundation of in-vivo strain quantification technique utilized by our study group, Demons registration has been commonly used for this purpose [58, 59]. When applied on 3D high-resolution anatomical image sets, voxel wise strain tensors can be calculated in an arbitrary frame of reference [57, 60, 61]. However, information contained by strain tensor is physiologically relevant when expressed with respect to the muscle fiber direction. Fortunately, versatile nature of the MRI can be leveraged to localize fiber directions with the employment of diffusion tensor imaging (DTI). The following section dwells on the methodological aspects of the combined MRI-DTI method for the assessment of in-vivo musculoskeletal mechanics.

1.3 Combined MRI-DTI Method for In-Vivo Soft Tissue Mechanics

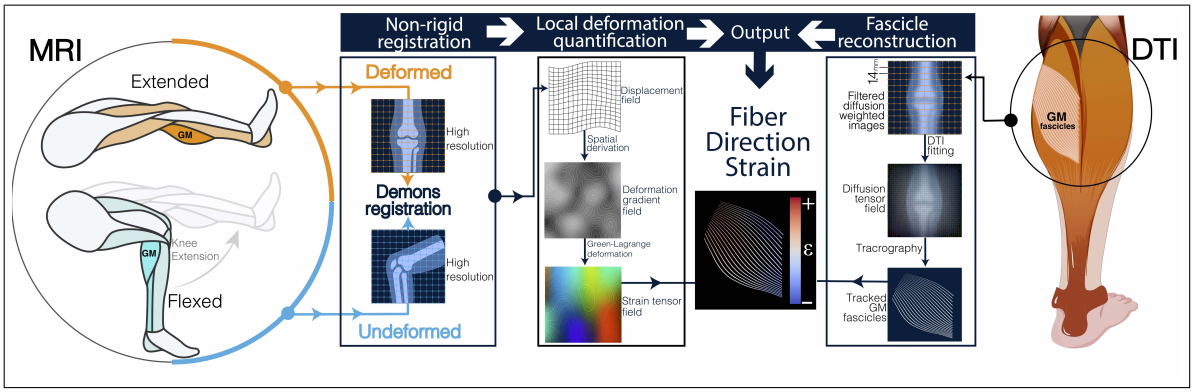

Figure 1.1 Schematic illustration of the combined MRI-DRTI method to calculate fiber direction strain distributions, exemplifying the deformation in passive medial gastrocnemius (GM) muscle between flexed (undeformed) and extended (deformed) knee joint configurationss.

1.3.1 Voxel-wise strain tensor calculation using demons algorithm

Demons non-rigid image registration takes two images as input and generates a displacement field that maps each undeformed state voxel $P(X, Y, Z)$ onto each deformed state voxel $P(x, y, z)$. Since both anatomical image sets were acquired using a high-resolution 3D MRI sequence (Figure 1.1), each voxel in the displacement field obtained represents a vector ($\vec{u}$) in 3D Cartesian coordinates:

$$\vec{u} = \begin{pmatrix} u_1 \\ u_2 \\ u_3 \end{pmatrix} = \begin{pmatrix} x - X \\ y - Y \\ z - Z \end{pmatrix} = P(x, y, z) - P(X, Y, Z) \tag{1.1}$$

Using the displacement field determined, the deformation gradient matrix F is obtained by arranging the derivatives of the position vectors of the undeformed and deformed configurations in Jacobian format as follows:

$$F = \begin{pmatrix} F_{11} & F_{12} & F_{13} \\ F_{21} & F_{22} & F_{23} \\ F_{31} & F_{32} & F_{33} \end{pmatrix} = \frac{\partial(x, y, z)}{\partial(X, Y, Z)} = \begin{pmatrix} \frac{\partial x}{\partial X} & \frac{\partial x}{\partial Y} & \frac{\partial x}{\partial Z} \\ \frac{\partial y}{\partial X} & \frac{\partial y}{\partial Y} & \frac{\partial y}{\partial Z} \\ \frac{\partial z}{\partial X} & \frac{\partial z}{\partial Y} & \frac{\partial z}{\partial Z} \end{pmatrix} \tag{1.2}$$

Lagrangian description of the displacement gradient matrix ($\triangle u$) is computed as follows:

$$\triangle u = F - I \tag{1.3}$$

where I is a 3x3 identity matrix.

Finally, local deformations in Cartesian coordinates are quantified by calculating Green-Lagrange strain tensor (E) as follows:

$$E = \frac{1}{2}(F^T F - I) = \frac{1}{2}(\triangle u + \triangle u^T) + (\triangle u \triangle u^T) \tag{1.4}$$

where T denotes the transposition operator.

1.3.2 Reconstructing fascicles and probing the tissue microstructure using diffusion imaging

Streamline tractography is a commonly used technique in the treatment of the DT-MRI data to probe underlying geometric pathways. This tracking knowns to fail reconstructing representative tracts in the presence of complex fiber architecture due to within-voxel direction dispersions [62]. This has been one of the long standing challendes in the reliability of tracking white-matter tracts [63]. However, solutions to even such problems have been developed such as acquiring multishell diffusion data at higher b-values, which aims at resolving multiple intravoxel fiber orientations by higher order signal expansions [64, 65] or mesoscopic biophysical models [66, 67, 68]. On the other hand, streamline tractography performs well if the physical arrangements of the fibers within the anatomy of interest are not complex [69]. Skeletal muscles are a good example to this, as the principal axis of diffusion is dominated by a single direction, where the fibers do not cross or converge [70, 71]. Nevertheless, the signal to noise ratio (SNR), the trade-off between increasing the number of excitations vs encoding more diffusion directions, the b-value optimization (typically around 500 s/mm^2) and confounding T2 changes (e.g., muscle injury or high intensity exercise) are among the core factors that determine the accuracy of DTI indices in the muscle [72], as well as the intramuscular fat infiltration [73]. To form an opinion about the uncertainty of tractography is to analyze the distribution of Fractional Anisotropy (FA), as lower FA values lead to higher errors in the calculation of the principal eigenvector of the

diffusion tensor that encodes the orientation of the myofibers [74]:

$$FA = \sqrt{\frac{3}{2}} \frac{\sqrt{((\lambda_1 - \bar{\lambda}) + (\lambda_2 - \bar{\lambda}) + (\lambda_3 - \bar{\lambda}))}}{\sqrt{\lambda_1^2 + \lambda_2^2 + \lambda_3^2}} \tag{1.5}$$

where $\bar{\lambda}$ is the average of eigenvalues $(\lambda_1, \lambda_2, \lambda_3)$ of the diffusion tensor. FA takes a value between 0 and 1, and specifies what fraction of the diffusion directionality is restricted within a voxel.

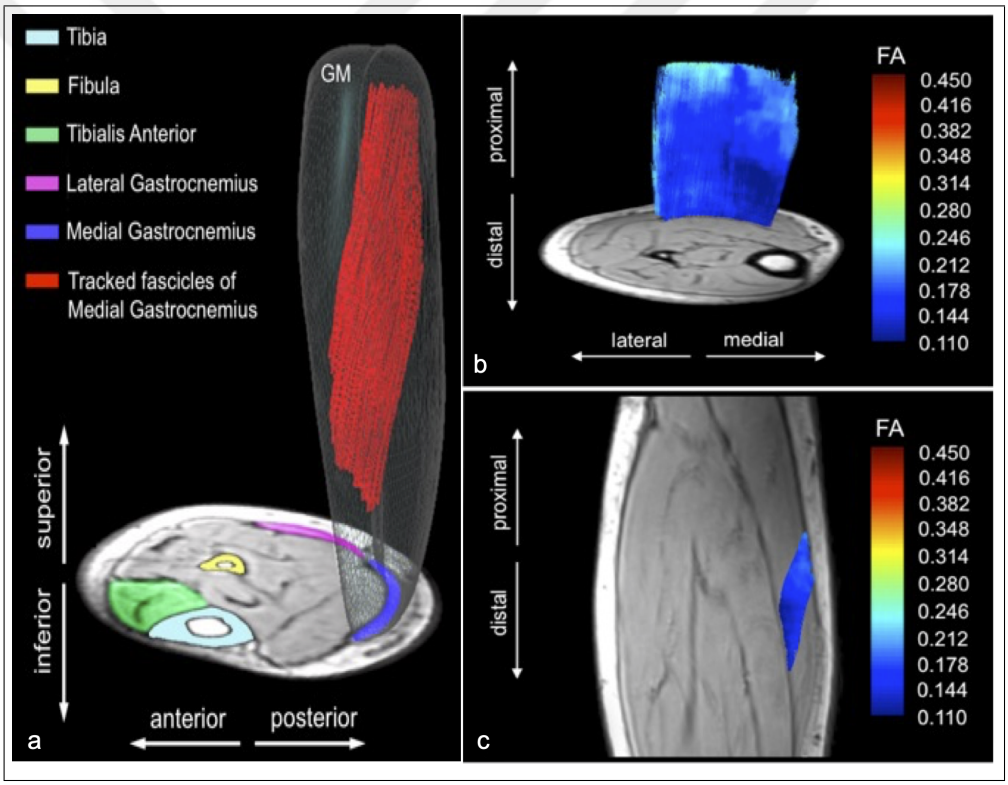

Figure 1.2 Diffusion Tensor Imaging (DTI) tractography of human medial gastrocnemius (GM) muscle. a) GM fascicles (red) are visualized within the reconstructed surface mesd model (gray) of the muscle. b) Spatial distribution of nodal fractional anisotropy (FA) values. c) Coronal anatomical image showing the crossection of the FA-mapped GM fascicles.

Note that in structures with simple fiber orientation distribution, a high spatial variation in FA distribution is unlikely. For example, white matter of the human brain has a quite wide FA distribution ranging from 0.1 to values as high as 0.9 [75], whereas

human thigh muscles show a much lower FA variation. For example, a mean FA value of 0.27 and 0.18 with a very small standard deviation (0.02 and 0.03) has been reported for human lateral and medial gastrocnemius muscles, respectively [76]. The spatial distribution of FA values in Figure 1.2 agrees well with these expectations (0.213 ± 0.019). Similarly, the FA values reported for the skeletal muscle vary around 0.2 [77, 69]. This is mostly because these studies employed spin-echo based acquisitions with short diffusion times, resulting in a mean square displacement that is shorter than the average fiber length [78]. When performed using stimulated echoes, longer diffusion times can be achieved for the skeletal muscle without considerable SNR penalty, which is the case for spin-echo based DTI. As a result, higher FA values, e.g., up to 0.5 in GM, can be achieved in skeletal muscle. Nevertheless, the variation still remains low [79]. Since the in-vivo validation of musculoskeletal DTI tractography 2002 [80], it has been applied in several studies to reveal cytoarchitecture in passive muscle deformation [81, 82, 83], muscle damage [84, 85], pathology [73, 86], muscle activation [87, 76], exercise [88] and to investigate anthropological differences [89]. In conclusion, DTI tractography is a powerful tool for probing 3D orientation of in-vivo muscle fibers wihen the acquisition protocols are optimized pertinently.

1.3.3 Calculation of fiber direction strains

Voxelwise strain tensors calculated by demons algorithm as described in Section 1.3.1 express the deformation in an arbitrary frame of reference. Even though eigen composition and strain invariants can be used to calculate principal and shear strains, physiologically relevant deformation occurs along the muscle fiber direction. It is worth nothing that the orientation of muscle fibers does not neccesarily align with the direction pointed by the eigen vector of the highest principal strain. To supplement voxelwise strain tensors with the relevant information, vector expression of the direction muscle fiber direction ($\vec{t}$) can be given as a normalized tangent vector between two successive fiber tract nodes. Next, a fiber direction strain coefficient (ε_f) is obtained at each tract node by aligning strain tensor to the direction specified by corresponding $\vec{t}$ vector as follows:

$$\varepsilon_f = \vec{t}^T E \vec{t} \tag{1.6}$$

where T is the transposition operation and E is the strain tensor. To obtain strain scalars at the corresponding off-grid tract nodes, tensor interpolation methods can be applied.

1.3.4 Non-rigid registration for tissue morphometry has a track record of accomplishment

Recognized as one of the most groundbreaking methods in the computational neuroanatomy, deformation-based morphometry defines the coupled use of registered images and the deformation fields obtained by the registration itself [90]. This approach has been being extensively used for the longitudinal and across-subject evaluation of the relative positions of the structures in the brain [91]. Drawing upon deformation based morphometry, tensor-based morphometry calculates the spatial derivate of the deformation field to extract information to characterize differences in the local shape of brain structures. These applications of continuum mechanical approaches on in-vivo anatomical images has become such popular in the realm of brain imaging that the work by Ashburner and Friston [90] became the most cited article in the history of neuroimaging. Today, collection of these methods is recognized by almost every computational neuroscience researcher in the world under the name of the open software package that implements them, statistical parameter mapping, i.e., the SPM [92].

Surprisingly, the concept of characterizing mechanical deformation through a non-linear registration is not such widely accepted by the biomechanics community, despite the higher acclimatization of the field to the continuum mechanical calculations. Quite the contrary, it spurred some controversy [93], in part due to lesser popularity of non-rigid registration in the biomechanics literature. Nevertheless, this approach has proven track record of application, dating back to almost two decades ago. For exam-

ple, Fox et al. (2001) used the Jacobian determinant of the deformation field obtained by non-linear registration to assess brain atrophy in Alzheimer?s disease patients with a follow-up period up to 8 years [91]. Obviously, as it is possible to quantify Jacobian determinant, it is also possible to derive Green-Lagrange strain tensor from the deformation field to inform voxels about the length changes, which ensures that principal strain is positive for elongations and negative for contractions. This approach has been first applied by Yaman et al. (2013) to quantify strain tensors by using demons algorithm to non-rigidly align images acquired in successive anatomical scans at deformed (flexed) and undeformed (extended) knee joint configurations [57].

However, applying morphometrical analyses to skeletal muscle comes with its own set of challenges. Expressing deformation tensors in an arbitrary frame of reference may suffice to study neuroanatomical changes. However, physiologically relevant length changes in skeletal muscle occurs in the fiber direction. Fortunately, DTI clears the way for probing this directionality in voxel level, which forms the input for the reconstruction of myofascicles as 3D streamlines via tractography. Rotating voxel-wise strain tensors to the fiber direction pointed by the unit vectors between individual streamline segments (nodes) yields length changes in fiber direction (Section 1.3.3). This allows visualization of local strain distributions on the tracked streamlines and provides a powerful tool for in-vivo exploration of musculoskeletal mechanics.

In agreement with recent finite element modelling [34], proximal and distal GM fascicle regions undergo differential length changes. In passive muscle, this trend manifests as proximally lengthened and distally shortened fascicle bundles, explained by the effect of distally directed myofascial loads ascribed to the mechanical interaction of the muscle with its surrounding tissues. This is contrary to the classical viewpoint, which ignores myofascial loads and expects uniform length changes along the fiber length.

In conclusion, non-invasively decoupling origins of epimuscular mechanical interactions within a wide and volumetric field of view is challenging. Therefore, MRI-DTI approach as an intriguing step to examine the intricate link between muscle anatomy and function in-vivo. The following section will look into the success of demons algo-

rithm in calculating tissue deformations.

1.4 Earlier use and success of Demons algorithm in calculating tissue deformations

Demons registration was introduced by Thrion (1998) as a method based on the optical flow principles. The purpose of this technique is to non-rigidly deform one image into another on a sub-voxel basis in order to establish a spatial matching between the images. Thirion?s algorithm regularizes the total displacement field in each iteration by smoothing it with a Gaussian kernel until the convergence criterion is satisfied [94]. Therefore, this algorithm can be described as a diffusion-like optimization process that is performed on the entire displacement field [95]. The earliest applications of Demons algorithm involve multi-modality registration for assisting transbronchial biopsy [96] and automatic detection of hippocampal atrophy on magnetic resonance (MR) images [97]. In those years, a study focusing on theoretical understanding of Demons algorithm indicated that this method can be considered as an application of a second order optimization to minimize the sum of squared differences of voxel intensities [98]. Note that such image similarity measure is especially recommended for intra-modality image registration (Hutton et al. 2003, Nestares et al. 2000). Consequently, Demons algorithm is commonly preferred for registration of medical images from the same modality in the more recent years [99, 100, 58, 61].

Demons algorithm has been utilized for calculating deformations in various tissues such as pelvic floor [59], lung [100], myocardium [58] and finger flexor muscles [99]. In those studies, good agreements were shown among strains calculated using Demons algorithm and those determined by other registration methodologies and imaging modalities. A commonly used reliable method to test algorithm success is to use synthetic image sets with known deformations imposed on the test image itself [101, 95]. On the other hand, physical phantoms are used for a more direct testing [102, 59]. Wang et al. (2005) validated the algorithm quantitatively by using both of

these testing methods. Their method involves known deformation tests for synthetically deformed prostate and neck computerized tomography (CT) images and for a physically deformable pelvis phantom. They showed that Demons algorithm successfully establishes spatial correspondence between the features of synthetically transformed images with the mean error margin at a level of sub-millimeters. Results from phantom tests revealed a spatial matching accuracy of better than 1.5 mm for this algorithm. Furthermore, based on their findings from dynamic tumor contour deformation tests, the authors concluded that Demons algorithm has sufficient mapping accuracy to be implemented in the targeting of radiotherapy to the cancerous tissue. Also Samant et al. (2008) indicated such potential application of the algorithm in adaptive radiotherapy [103]. This points out the reliability of Demons algorithm in estimating non-rigid deformations even for such critical clinical implementations. Note that such radiotherapy oriented registration studies were carried out using CT. Although MR images have relatively less spatial resolution compared to CT images, they provide a superior soft tissue contrast, which facilitates successful spatial matching for non-rigid registration of also anatomical MR image pairs.

This technique reliability of which was well established was employed recently to assess the deformation of human lower leg musculature [57, 61]. Knee angle changes were imposed passively to alter the length of m. gastrocnemius, whereas the ankle was fixed to restrain distally the lengths of all lower leg muscles. Yaman et al. (2013) devised a synthetic known image deformation test involving very similar displacements to those occurring in the experiments, which were imposed exclusively on m. gastrocnemius, forcing the remaining tissue volume to be absolutely undeformed. Such challenging registration yielded no false deformations to be calculated in that volume and strains of similar order of magnitude as those imposed by image deformation were calculated for m. gastrocnemius. This confirms success of Demons algorithm for muscle tissue analyses, but also shows its limitations: (1) strains were somewhat underestimated suggesting that they are conservative estimators of actual local deformations. (2) Sharp discontinuities in deformation yield errors for narrow regions separating the deformed and undeformed volumes indicating that deformations in boundaries between anatomical units need caution. However, strict discontinuities as such are unrealistic

during actual joint movement and also in the present test protocol, which does not involve joint movement. Huijing et al. (2011) and Yaman et al. (2013) conducted also a rigid body motion test by imposing synthetic motion representing a much larger scale motion than possible motion of subjects during imaging. As this should theoretically cause zero strain it is a good test of the algorithm, which yielded very small strains, calculated in those studies and presently. Robustness of this technique to quantify physiologically relevant in-vivo deformations in human lower leg musculature has also been tested against actual subject repositioning [60]. Those authors quantified local tissue deformations caused by Kinesio Taping within the entire lover leg in a unique way. They showed that error strains caused by subject positioning were larger than those imposed by synthetic rigid body deformation. However, both of them were significantly smaller than those caused by Kinesio Taping indicating effects induced by this treatment do dominate such artifacts and Demons algorithm is sensitive to discriminate those. This is important because according to some researches this treatment is not capable of causing considerable effects [104, 105]. In contrast, quantifying local tissue deformations due to Kinesio Taping yielded a great novel insight for an objective understanding of the effects of this treatment. Note that the experimental testing conditions in the present study did not require the subjects? repositioning. Therefore, an additional testing of such repositioning was not performed.

It is important to note that all medical images are subject to noise due to imperfections of the utilized image acquisition hardware. Therefore, possible adverse effects of such noise on quantitative image analysis must be considered. This becomes even more critical if a directional change estimator, e.g., spatial gradient operator is utilized, as done presently. As a consequence, strain quantification may be affected by intensity non-uniformity [106] in acquired anatomical images due to MRI instrumentation based imperfections [107]. Those include variations in the main magnetic field, radiofrequency (RF) inhomogeneity and eddy current distortions. Anatomy dependent properties such as shape and electromagnetic characteristics can also lead to such imperfections [108]. Utilization of the same coils for both transmission and reception is known to make image acquisition insensitive to RF inhomogeneity for the fast-low-angle-shot FLASH sequence [109]. It is highly possible that the presently employed

anatomical image acquisition method partly compensated plausible hardware-based intensity non-uniformity because FLASH sequence was employed with an acceptable nominal flip angle of 30°using surface coils for both transmission and reception. However, this alone may be inadequate to resolve such stochastic effect. Taking that into account, we performed an additional test and assessed the effect of inevitable different noise distributions in different scans on strain quantification using Demons algorithm: subsequently acquired separate anatomical image sets in identical subject position were registered. This assessment showed that strain artifacts caused by hardware-based noise were much smaller than strains occurring due to submaximal activity. In addition, those artifacts did not show a sizable variance that would cause sizable strain heterogeneity across a region. This indicates objectively that strain artifacts are present due to sources of noise in MR imaging, but the experimental deformations both regarding strain amplitudes and distribution patterns are not ascribable to them. We anticipate that further technical developments marginalizing any artifacts of the employed advanced MRI analyses and tailoring them also to other protocols of musculoskeletal applications can yield highly relevant new studies.

1.5 Aims of the Thesis

In light of the overview presented above and the developments needed to study muscle structure function relationship in-vivo, this thesis aims at:

1. Building a relational analysis framework that enables numerical investigation of mechanical relationships between fiber direction strains and any information layer with spatial correspondance.

2. Testing the hypothesis that neurovascular tracts indicate exposure to the myofascial loads in human GM muscle upon sustained isometric plantar-flexion by using the methodology developed in (1).

3. Performing a robustness analysis to test the hypothesis that demons algorithm tuning parameters are not a significant determinant of fiber direction strain het-

erogeneity on passive joint motion.

4. Using velocimetry and quantitative MRI for the cross-modality validation of demons algorthm based strain quantification and to explore the added value of microstructure imaging in assessing muscle structure function relationship, respectively.

1.6 Thesis Overview

1.6.1 Magnetic resonance and diffusion tensor analyses indicate heterogeneous strains along human medial gastrocnemius fascicles caused by submaximal plantarflexion

The first aims of the thesis is addressed by first developing a MATLAB codebase that enables using DTI reconstructed fascicles as a basis to compare image registration derivatives (e.g., the displacement field, strain tensors and invariants) with macroscale extramuscular linkages. This was achieved by using a spatial statistics framework in the context of continuum mechanical analyses. Second aim was achieved by applying this methodology on the analysis of fiber direction strains upon sustained submaxial isometric plantarflexion. First principal strains were calculated on manually segmented neurovascular tracts (NVTs) and visualized along with fiber direction strain encoded fascicles. Findings are presented in Chapter 2. The results suggested a dominant existence of distally directed myofascial loads (proximally shortened, distally lengthened deformation pattern, consistent across participants) that are locally modified at the intersection of NVTs, confirming the hypothesis that neurovascular tracts indicate exposure to the myofascial loads in human GM muscle upon sustained isometric plantar-flexion. These findings are discussed in the context of myofascial force transmission and its relevance for in-vivo muscle function, including an assessment of the parallel distribution of strain in Appendix A.

1.6.2 In-vivo along muscle strain heterogeneity is not affected by image registration parameters: robustness testing of combined magnetic resonance and diffusion tensor imaging method

The second aim of the thesis is addressed by performing a multiverse analysis on the tuning parameters (α and σ) of the demons non-rigid registration algorithm using a multimodal passive knee extension dataset consisting of 5 healthy participants. Findings are presented in Chapter 3. Combined use of tile charts, analytical statistical tests and the hierarchical shift function analysis have shown that demons algorithm tuning parameters do not determine the heterogeneity pattern across muscle parts of the GM, confirming the hypothesis. Nevertheless, parameter selection substantially modifies the amplitude of fiber direction strains. Outlier strains that appear to be affected the most by the parameter changes are found near the areas of discontinuity, not in the proximity of NVTs (Appendix B).

1.6.3 Velocimetry and quantitative MRI for cross-validation, generalizability and microstructural origin assessment of fiber direction strains as calculated by demons non-rigid registration

The third aim of the thesis is first achieved by acquiring a single participant dataset at a different imaging center (passive knee extension experiment, with reference to [82]) along with a quantitative imaging protocol to calculate T1, magnetization transfer ratio (MTR) and saturation index (MTsat) maps for the assessment of the relevance of the underlying microstructure. The processing was performed using a processing pipeline that is different than the reference method for the assessment of generalizability. As for the cross-modality validation, 2D velocity-encoded phase-contrast (VE-PC) and compressed sensing accelerated 4D PC dataset derivatives were used (kindly acquired, processed and shared by the research team of Drs. Usha and Shantanu Sinha from San Diego State University, CA, USA) . Findings are presented in Chapter 4. Fiber direction strains upon passive knee extension show a similar distribution pattern and strain amplitudes to those reported by the reference study [82].

This indicates the generalizability of MRI-DTI methodology to study in-vivo musle mechanics. Among the quantitative metrics tested, T1 distribution were the strongest predictor of the strain distribution, whereas no significant relationships were observed for MTR and MTsat. There exist a subtle similarity between the strain rate (from 2D VE-PC, cyclic contraction) and fiber direction strain (demons algorithm, sustained contraction) show subtle distribution similarities. Nevertheless, 4D PC data provides a better comparison basis. Distribution of principal strains on GM as calculated by demons algorithm show comparable patterns to those revealed by strain rate maps. Overall, the results shown in this work constitute a proof-of-concept for the validation and understanding of the physiological relevance of demons algorithm based strains with orthogonal information provided by highly accelerated and quantitative acquisition sequences.

1.7 List of Publications Produced From the Thesis

1.7.1 Journal publications

1.7.1.1 First author.

1. "Magnetic resonance and diffusion tensor imaging analyses indicate heterogeneous strains along human medial gastrocnemius fascicles caused by submaximal plantar-flexion activity", A. Karakuzu, U. Pamuk. C. Ozturk, B. Acar, C. A. Yucesoy, Journal of Biomechanics, Vol. 57, pp. 69-78, 2017.

2. "In-vivo along muscle fascicle strain heterogeneity is not affected by image registration parameters: Robustness testing of combined magnetic resonance - diffusion tensor imaging method", A. Karakuzu, A. Arpak, C. A. Yucesoy, Journal of Mechanical Behavior of Biomedical Materials, Under Review, 2022.

1.7.1.2 Not first author.

3. "Combined magnetic resonance and diffusion tensor imaging analyses provide a powerful tool for in vivo assessment of deformation along human muscle fibers", U. Pamuk, A. Karakuzu, C. Ozturk, B. Acar, C. A. Yucesoy, Journal of Mechanical Behavior of Biomedical Materials, Vol. 63, pp. 207-219, 2016.

4. "The role of intra-and epimuscular fasciae beyond being passive structural elements: MRI analyses indicate that they interfere with and affect muscle?s active mechanics",O. B. Gozubuyuk, A. Karakuzu, U.Pamuk, C. A. Yucesoy, Journal of Bodywork and Movement Therapies, Vol. 22:4, pp. 852-853, 2018.

5. "Successful return to play following adductor longus proximal tendon rupture in professional soccer without re-injury at 12 months: A case report",O. B. Gozubuyuk, M. H. Hoen, M. Akman, I. Ipseftel, A. Karakuzu, Journal of back and musculoskeletal rehabilitation, Vol. 31:3, pp. 583-587, 2018.

1.7.2 Conference Proceedings

1.7.2.1 First author.

6. "Assessment of in-vivo skeletal muscle mechanics during joint motion using multimodal magnetic resonance imaging based approaches", A. Karakuzu, U. Pamuk, C. Ozturk, C. A. Yucesoy, 18th National Biomedical Engineering Meeting, BIYOMUT, SP7, p. 34, Oct 16-17. 2014, (accessed on 02.12.2018)
10.1109/BIYOMUT.2014.7026373
http://www.biyomut2014.boun.edu.tr/BIYOMUT2014/Bildiri_Kitapcg_files/BIYOMUT2014_OzetKitabi.pdf

7. "Using advanced MRI techniques for estimating strain distributions along muscle fibers during isometric plantar-flexion activity of human medial gastrocnemius, in vivo", A. Karakuzu, U. Pamuk, B. Acar, C. A. Yucesoy, International Society of Biomechanics, ISB, XXVth biennial international congress of ISB, pp. 1339-1340, Jul 12-16, 2015, (accessed on 08.08.2022)

https://media.isbweb.org/images/conferences/isb-congresses/2015/isb_2015_abstract_book_final.pdf

8. "Quantifying deformations along human skeletal muscle fibers invivo: Multimodal MRI assessments in passive and active conditions", A. Karakuzu, U. Pamuk, C. Ozturk, B. Acar, C. A. Yucesoy, 8th Congress of the National Biomechanics Society of Turkey, Ankarak Oct 19-23, 2016, (accessed on 08.08.2022) https://silo.tips/download/uluslararas-katlml-8-ulusal-biyomekanik-kongresi-bilimsel-program -19-ekim-2016-a[1]

9. "Combined Diffusion Tensor and Magnetic Resonance Imaging for in vivo Assessment of Human Muscle Function", A. Karakuzu, U. Pamuk, P. Akyazi, C. Ozturk, B. Acar, C. A. Yucesoy, 21st Annual Congress of the European College of Sports Science, Vienna, Jul 6-9, 2016.

10. "On the reproducibility of mri-dti based passive length changes and the added implications of quantitative mri", A. Karakuzu, J. Cohen-Adad, N. Stikov, C. A. Yucesoy, International Society of Biomechanics, ISB, XXVIIth biennial international congress of ISB, Calgary Jul 31, 2019.

1.7.2.2 Not first author.

11. "Effects of variation of stretch and activation level on human gastrocnemius geometric and mechanical metrics", U. Pamuk, A. Karakuzu, C. A. Yucesoy, editor J. Ojeda, European Society of Biomechanics, ESB, 23rd annual congress of ESB, YÖK yayın ID: 4150430, 2-5 Jul 2017, (accessed on 08.08.2022) https://esbiomech.org/conference/archive/2017 seville/papers/ 1665-4570-1-PB.pdf

12. "Intra- and epimuscular connective tissues are not just passive structural elements, but interfere with, and affect muscle's active mechanics", C. A. Yucesoy,

[1] Awarded Prof. Dr. E. Zeki Korkusuz Biomechanics Research Award for the best presentation

A. Karakuzu, U. Pamuk, World Congress of Biomechanics, WCB, 8th biennial WCB. Mechanics of passive muscle and connective tissue 1, Jul 08-12, 2018, (accessed on 02.12.2018)
https://app.oxfordabstracts.com/stages/123/programme-builder/submission/19761?backHref=/events/123/programme-builder/view/sort/author&view=published

13. "MRI and DTI analyses combined provide a powerful tool for quantifying deformation along human muscle fibers in vivo", U. Pamuk, A. Karakuzu, B. Acar, C. Ozturk, C. A. Yucesoy, International Society of Biomechanics, ISB, XXVth biennial international congress of ISB, pp. 903-904, Jul 12-16, 2015, (accessed on 02.12.2018) https://isbweb.org/activities/congresses
https://isbweb.org/images/conferences/isb-congresses/2015/isb_2015_abstract_book_final.pdf

14. "MRI analyses indicate non-uniform human muscle tissue deformations and confirm theoretically anticipated sarcomere length heterogeneity, in vivo", U. Pamuk, A. Karakuzu, P. Akyazi, B. Acar, C. Ozturk, C. A. Yucesoy, 18th National Biomedical Engineering Meeting, BIYOMUT, SP9, p. 35, Oct 16-17, 2014, (accessed on 02.12.2018) 10.1109/BIYOMUT.2014.7026392,
http://www.biyomut2014.boun.edu.tr/BIYOMUT2014/Bildiri_Kitapcg_files/BIYOMUT2014_OzetKitabi.pdf

15. "Magnetic resonance imaging analyses confirm so far theoretically posed intermuscular interaction effecs, in vivo", U. Pamuk, A. Karakuzu, P. Akyazi, B. Acar, C. Ozturk, C. A. Yucesoy, International Society of Electrophysiology and Kinesiology, ISEK, XX ISEK congress, p. 81, Jul 15-18, 2014, (accessed on 02.12.2018)
https://isek.org/past-conferences/
https://isek.org/wp-content/uploads/2015/10/ISEK2014Rome.zip

16. "Muscles' activation state affects medial gastrocnemius fiber strain heterogeneity: Assessment using MRI and DTI methods", U. Pamuk, A. Karakuzu, G. Sanlı, C. A.Yucesoy, International Society of Biomechanics, ISB, XXVIth biannual international congress of ISB, p. 107, Jul 23-27, Brisbane 2017, (accessed on

02.12.2018) https://isbweb.org/images/conferences/isb-congresses/2017/ISB2017-Full-Abstract-Book.pdf

17. "Kinesio Taping Effects on Along Muscle Fascicle Local Length Changes: Magnetic Resonance and Diffusion Tensor Imaging Based Assessment", S. Yildiz, A. Arpak, A. Karakuzu, C. A.Yucesoy, 6th International Fascia Research Conference, Sep 10-14, Montreal 2022.

18. "Unintended Botolinum Toxin Type-A Effects on Muscle Mechanics are Notable and Progressive In Time", C. S. Kaya-Keles, A. Karakuzu, C. A.Yucesoy, 6th International Fascia Research Conference, Sep 10-14, Montreal 2022.

2. MAGNETIC RESONANCE AND DIFFUSION TENSOR IMAGING ANALYSES INDICATE HETEROGENEOUS STRAINS ALONG HUMAN MEDIAL GASTROCNEMIUS FASCICLES CAUSED BY SUBMAXIMAL PLANTAR-FLEXION ACTIVITY

2.1 Introduction

Sarcomere is the basic functional element of skeletal muscle and its length is the key determinant of force production [25]. Sarcomere length changes are also central to the excursion of the muscle. Therefore, in order to characterize the contribution of activated human muscle to joint function in vivo, it is crucial to quantify length changes along the fascicles. Nevertheless, this is quite challenging because the target muscles are not directly accessible to be tested with techniques such as laser diffraction [110]. Taking biopsied muscle samples from patients with cerebral palsy, sarcomere length estimation has been done fairly precisely [111]. However, these samples characterize length changes at only selected few locations. Moreover, laser diffraction imaging was used to sample large numbers of sarcomeres in thick whole longitudinal sections of isolated rat muscle [112]. The finding from this study revealed prominent regional sarcomere length variations across the muscle. even though it was not performed in vivo, and individual fascicles were not tracked, these findings underpin the significance of such applications in human skeletal muscle.

In vivo, muscle operates in a system of a fascial integrity. The epimysia of neighboring muscles are linked [9]. Additionally, collagen reinforced neurovascular tracts (NVT) continuous with the compartmental boundaries interconnect neighboring and distant muscles [10, 2]. On altered relative position of the muscle with respect to its surroundings, epimuscular myofascial loads originating from that system act on the muscle belly [113, 16]. These loads can be transmitted inside the muscle because

the extracellular matrix (EMC) is a part of the fascial integrity. The ECM is also connected to muscle fibers along their full peripheral surface [13]. Therefore, for muscle in vivo, epimuscular myofascial loads and intramuscular ones originating from the ECM and muscle fibers can manipulate local deformation along the fascicles [16, 2]. Finite element modeling has indicated theoretically that strain distribution can be non-uniform such that shortened and lengthened segments can be present along the same fascicle of stimulated muscle [17, 114]. This is considered to manipulate force production and length range of force exertion [15] and as an important determinant for the outcome of orthopedic surgery [113, 115] and botulinum toxin treatment [19, 20].

Magnetic resonance imaging (MRI) techniques are highly suitable for studying human muscles, in vivo. MRI deformation analyses enable calculation of local muscle tissue deformations in active [116, 117, 118, 119] and passive conditions [61, 57]. Moreover, 3D orientation of the skeletal muscle fibers can be determined using Diffusion Tensor Imaging (DTI) [71]. DTI has previously been used to study fascicle architecture in human muscles [120, 121], including the medial gastrocnemius (GM) [122]. Yet, only few studies have combined both aspects of the MRI technique [123, 124]. Recently, Pamuk et al. (2016) studied human GM fascicle strains caused by passively imposed knee joint angle change [82]. However, assessments of local tissue deformations along human skeletal muscle fascicles caused by in-vivo activity are lacking.

Based on the findings of the reviewed experimental studies and finite element modeling we hypothesized that submaximal plantar flexion activity causes heterogeneous length changes along the fascicles of human medial gastrocnemius (GM) muscle, in vivo. In this study, using MRI based deformation analyses and DTI based tractography combined, our aim was to test this hypothesis.

2.2 Methods

2.2.1 Subjects

Experimental procedures were in strict agreement with the guidelines and regulations concerning human welfare and experimentation set by Turkish law and approved by a Committee on Ethics of Human Experimentation at Boğaziçi University, Istanbul. Five healthy female subjects (age=26±3year, height=162±7cm and body mass=51±5kg) volunteered (Table 2.1). Subjects from the same gender minimized anthropometric differences and women subjects less prone to fatigue [125] were preferred. Following a detailed explanation of the purpose and methodology of the experiments, the subjects gave their written informed consent.

Table 2.1
Anthropometric Data

Subject	**Age (years)**	**Height (cm)**	**Mass (kg)**	**Upper leg length (cm)**	**Lower leg length (cm)**	**Knee angle attained during testing (°)**
A	25	160	47	42.0	37.0	178
B	27	154	45	49.0	36.0	176
C	29	160	52	43.0	37.0	178
D	28	165	56	51.0	36.0	170
E	27	158	52	44.0	38.0	176

2.2.2 Experimental protocol and image acquisition

Subjects were positioned in prone position. The right foot was fastened to a custom-built foot pedal equipped with an MRI compatible dynamometer (Biopac TSD121B-MRI, CA, USA) at an ankle angle of 90°and the knee joint was fixed at full extension. Subsequently, the subjects were asked to perform MVC during 5 seconds of

plantar flexion followed by a two minutes rest period. This was repeated three times and the highest plantar flexion force value measured was determined to represent the MVC.

The subjects were trained to perform sustained isometric plantar flexion activity corresponding to 15% of MVC during six minutes with the help of a visual feedback interface. Such activity level was selected based on previous reports showing 15% of MVC as the highest activity, which in sustained conditions causes no substantial fatigue [126].

Each subject was positioned in a 3T clinical MR scanner (Magnetom Trio; Siemens, Erlangen; Germany) in prone position. The right foot was firmly fastened to the custom-built MRI compatible foot pedal at an ankle angle of 90°(Figure 2.1a). A piece of Velcro under the heel and straps over the ankle allowed joint position fixation. The knee was brought to fully extended position and fixed on the scanner table using a piece of Velcro attached over the patella and also on the MRI table. The knee angle in this position equaled (mean ± SD) 175°±3°. These joint configurations were maintained throughout the experiment. In relaxed condition of the subjects, image acquisition was done (*undeformed state*). Subsequently, the subjects performed sustained isometric plantar flexion at 15% MVC and maintained that during a second image acquisition (*deformed state*). Separate sets of 3D high-resolution anatomical (MR) and diffusion images (DT) were acquired for both states.

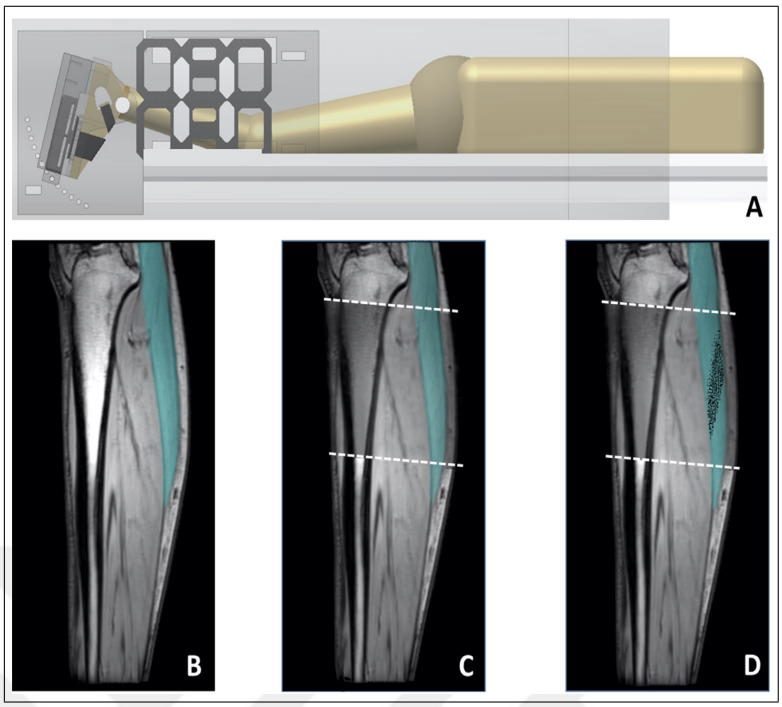

Figure 2.1 (a) Subject position in the undeformed (relaxed) and deformed (15% MVC) states was constant. The body was positioned prone on the patient table in the bore of the MRI machine. A custom made MRI compatible fixation device was used to fix the ankle angle at 90°. The foot pedal located in this device is equipped with an MRI compatible dynamometer (Biopac TSD121B-MRI, CA, USA) to measure the MVC level during scanning. An MRI compatible monitor allowed subjects to adjust and maintain activation at the target level. A piece of Velcro under the heel and strapping over the ankle allowed ?xation of the ankle angle. To locate the knee joint in extended position, a piece of Velcro was attached to the patella and a corresponding piece of Velcro was placed on the MRI table. (b) A sagittal-oblique anatomical MR image, aligned with the longitudinal axis of the GM (indicated in turquoise). (c) A matching diffusion weighted image (DWI) set is superimposed semi-transparently on the corresponding position of the GM. The region between the white dashed lines marks the longitudinal boundaries of the collected DWI. (d) The tracked GM fascicles (indicated in black) in the section considered are shown.

3D turbo fast low-angle shot (Turbo FLASH) based (Table 2.2) coronal MR image sets were collected using two 6-channel surface coils. Choices of high bandwidth and frequency encoding in proximo-distal direction (Weis et al. 1998) allowed minimizing potential chemical shift artifacts. Region between the most proximal part of the head of the tibia and the most proximal location of the transverse crural ligament comprised the field of view (FOV) (Figure 2.1b).

Table 2.2
MR and DT imaging parameters.

Modality	**MR imaging**	**DT imaging**
Sequence	Turbo FLASH	ss-EPI
Slice orientation	Coronal	Axial
Repetition time (TR) (ms)	1750	4900
Echo time (TE) (ms)	3.36	61
FOV (mm2)	320x320	180x180
Matrix	320x320	128X128
Pixel size (mm2)	1.0 x 1.0	1.4 x 1.4
Slice thickness (mm)	1.0	2.8
Flip angle (degrees)	12	90
Bandwidth (Hz/pixel)	130	2003
b-value (s/mm2)	N/A	450
Number of diffusion directions	N/A	12
Inversion time (TI) (ms)	1100	N/A
Acquisition time (mm:ss)	05:41	07:48

Subsequently, a 2D single shot echo planar imaging (ss-EPI) based multidirectional clinical DTI sequence was utilized (Table 2). Fat saturation and posterior-anterior direction frequency encoding were applied to minimize chemical shift artifacts in the region of interest. FOV of DT images along the proximo-distal axis include the region between the proximal neck of the tibia and the most distal border of the axial DT images (Figure 2.1c).

2.2.3 Calculation of deformations

Using sagittal localizer images, GM belly length was calculated as the distance between the femur condyle and GM muscle-tendon junction [127].

In vivo displacements caused by muscle activation were obtained by implementing Demons algorithm [128] a non-rigid and non-parametric image registration method, in MATLAB (The Mathworks Inc., USA) [129]. Following registration, displacement volume in the global coordinates was transformed on the deformed state b0 images. In order to assess deformations within the GM, Green-Lagrange strain tensors were calculated voxel-wise. The validity of Demons algorithm in quantifying tissue deformations has been shown earlier [59, 95]. The algorithm?s success in reproducing known deformations was tested vigorously for muscle tissue [57].

Rician noise was removed [130] from raw DT images. Subsequently, diffusion tensor of each voxel was calculated from these images. To reconstruct GM muscle fiber tracts, streamline tractography with 4th order Runge-Kutta numerical integration [131] was performed using custom software built on VAVframe framework [132]. Tract seed points were generated from voxels showing a minimum diffusion directionality (FA$\geq$0.1) [133]. The seed points were bi-directionally tracked with integration steps of half of the smallest voxel dimension (0.7mm) [134]. Each integration point forms a fiber node.

Tracking termination conditions were defined based on diffusion tensor and tract parameters to reconstruct GM muscle tracts. This operation was terminated when at least one of the following conditions was met: (i) The current tract node?s FA$<$0.5, (ii) tract curvature$>$5°(Froeling et al. 2012), (iii) total tract length exceeds 50mm [135]. Based on known muscle geometry of GM, tracts shorter than 30mm were discarded. One distally and one proximally located polygonal sections were defined across the GM within the non-weighted DT images (b0 images) of the deformed state and only the tracts running along both of them were accepted for further processing. Please see the supplementary material on fascicle tracking.

Strain tensors were linearly interpolated onto the nodes of the tracts based on the weighted means of the grid neighbors of a given voxel in the strain field. Finally, each strain tensor was rotated to align with unit tangent vector of the tract for each given node yielding fiber direction strain values. Nodal coordinates with corresponding tract strains were transferred to 3D Slicer v4 for visualization [136].

The GM volume studied was divided into ten muscle parts (P4-1, M1-2 and D1-4) per each 10% volume along the proximo-distal length. P4, D4 and M1-2 represent the most proximal distal and mid parts, respectively. Each muscle part was divided into 25 equal sub-volumes representing tract bundle segments. Mean nodal strains corresponding to each were pooled per muscle part for each subject and across all subjects, and were used in statistical comparisons of fiber direction strains occurring in different muscle parts.

Using anatomical MR images, arteries, veins and nerves perforating the GM were segmented as the deep (including Rr. Musculares, branching from N. Tibialis, and A. and V. suralis) and superficial (including N. cutanoues surae medialis, branching from N. Tibialis, N. suralis, N. saphenus, V. saphena magna and V. saphena parva) NVTs to the muscle. NVT intersections with the GM tracts were determined and visualized in fiber direction strain maps as key locations of epimuscular myofascial loading. First principal strains calculated for selected NVT sites were used to indicate presence of such loads.

2.2.4 Estimation of errors and repeatability

2.2.4.1 Strain artifacts caused by hardware-based noise. Two separate MR image sets of a subject in steady position were subsequently acquired and registered.

2.2.4.2 Test-retest repeatability. Repeatability After completing the original protocol and acquiring separate sets of 3D high-resolution MR in the undeformed and deformed states, the repeat protocol was executed in one subject: 3D high-resolution MR and DT images were acquired first in relaxed condition and subsequently during sustained isometric plantar flexion at 15% MVC. Deformation analyses and tractography were performed for the original protocol and its repetition.

2.2.4.3 Error strains caused by the algorithm. Error strains caused by the algorithm Theoretically, rigid body motion should cause no strains. To estimate error strains for the polled data collected from the subjects, image sets of the undeformed state were transformed by a synthetic rigid body motion imposed on the data: 10°rotation within the cross-sectional plane representing endorotation of the knee during ?exion [137], 3°rotations in the coronal and sagittal planes, and 4mm translation axially. The displacement fields calculated using Demons algorithm were mapped onto the tracked fibers and error fiber direction strains were determined.

2.2.4.4 Statistics. Paired sample t-test was performed to compare undeformed vs. deformed state GM belly lengths. Fiber direction strains among parts P4 to D4 pooled across all subjects and within each subject were compared by Kruskal-Wallis test followed by Dunn's procedure, including the repeatability test. Non-parametric Wilcoxon ranksum test was performed to compare experimental and error fiber direction strains. The differences were considered significant at $P<0.05$.

2.3 Results

Strain artifacts caused by hardware-based noise were small (2.3±1.2% and 2.0±1.4% for lengthening and shortening, respectively). The original and repeat protocols yielded a fairly good match between the deformation fields obtained (Figure 2.2): no significant differences were shown between mean fiber direction strain values per muscle part, yet strain values for the proximal muscle parts were significantly different from those of the distal muscle parts for both protocols (Table 2.3).

Table 2.3
Fiber direction strains (mean ± SD) in different muscle parts for the repeatability test.

Muscle part[1]	**Original**[2]	**Repeat**[3]
P4	-0.01±0.03	-0.01±0.03
P3	-0.02±0.02	-0.04±0.02
P2	0.03±0.03	-0.01±0.02
P1	0.04±0.05	0.04±0.02
M1	0.04±0.04	0.03±0.04
M2	0.06±0.03	0.02±0.05
D1	0.08±0.06	0.05±0.06
D2	0.09±0.08	0.07±0.05
D3	0.13±0.06	0.8±0.03
D4	0.09±0.02	0.6±0.01

[1] Muscle part: each one of the 10% of the GM volume (P4, P3, P2, P1, M1, M2, D1, D2, D3 and D4), where P4 and D4 represent the most proximal and distal parts, respectively and M1-2 represents the middle parts.

[2] Significantly different fiber direction strains for different muscle parts are as follows: For P4, P3 and P2: M2 and D1 to D4; for P1: D1 to D4; for D1, D2 and D4: P1 to P4 and M1; for D3: P1 to P4 and M1 to M2.

[3] No significant differences were shown between mean fiber direction strain values per muscle part of the original and repeat protocols.

Pooled data from all subjects showed the following: (i) mean error strains (1±1% and 2±1% for lengthening and shortening) (Figure 2.3a) are small and are significantly different from mean fiber direction strains (13.7±12% and 7.9±4% for lengthening and shortening) occurring due to maintained isometric plantar flexion activity (Figure 2.3b and 2.3c). GM belly length shortened significantly (from 223.2±13.2mm to 219.3±13.8 mm). (ii) Fiber direction strains in different muscle parts are not the same: most proximal muscle parts show shortening, whereas medial and distal muscle parts show lengthening (mean strains are up to 2% and 16%, respectively as shown in Table

2.4). The general nature of the deformation field throughout the GM indicate that proximal muscle parts show significantly different length changes compared to the mid and distal muscle parts and the mid muscle parts show that only compared to the less distal muscle parts. These findings indicate a non-uniform strain distribution along the tracked fascicles and confirm our hypothesis.

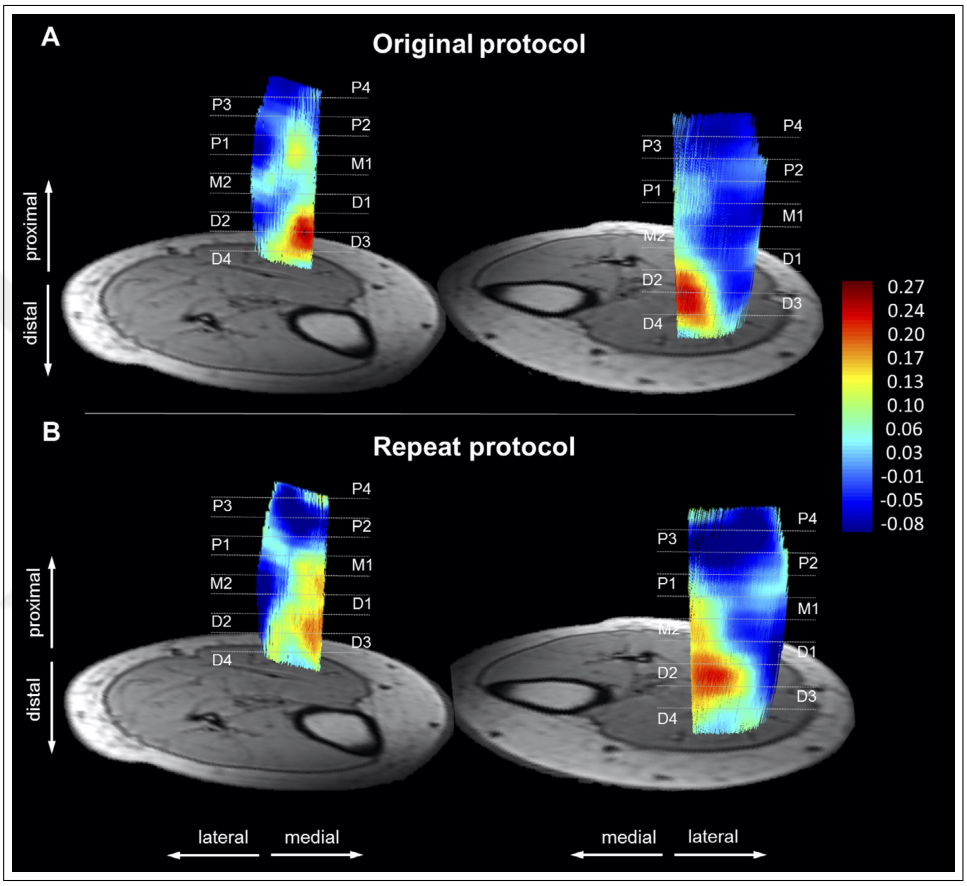

Figure 2.2 Fiber direction strain distributions occurring due to the original (a), and the repeat (b) protocols. The left panels show the anterior and the right panels show the posterior view of the tracked GM fascicles. The GM volume studied was divided into ten muscle parts (P4-1, M1-2 and D1-4) per each 10% volume along the proximo-distal length. These muscle parts are indicated using dotted lines, where P4, D4 and M1-2 represent the most proximal distal and mid parts, respectively.

Fiber direction strain distributions for subjects A-E agree with this general nature of the deformation field to a large extent (see Table 2.4 for exceptions). However, locally there are regions showing high fiber direction strain amplitudes and their locations vary between subjects. For subjects A, B and C, regions enclosed in muscle parts D1-2, D3-4 and D2-3 show strains ranging between 17-33%, 59-71% (for certain

nodes up to 100%) and 23-39% and indicating fascicle lengthening (Figure 2.4). For subject D regions enclosed in muscle parts P3-4 and D4 and for subject E, in M1-2, show strains ranging between 36-51% (up to 58%) and 8-16% also indicating fascicle lengthening (Figure 2.4). Notably, these regions include NVT intersections with the GM fascicles (across all subjects, fiber direction strains at those nodes show lengthening equaling mean±SD 0.09±0.13) and regions in the neighborhood. The first principal strains calculated for these NVT sites (up to 60% in subject B) do indicate presence of myofascial loads (Figs. 4 and 5).

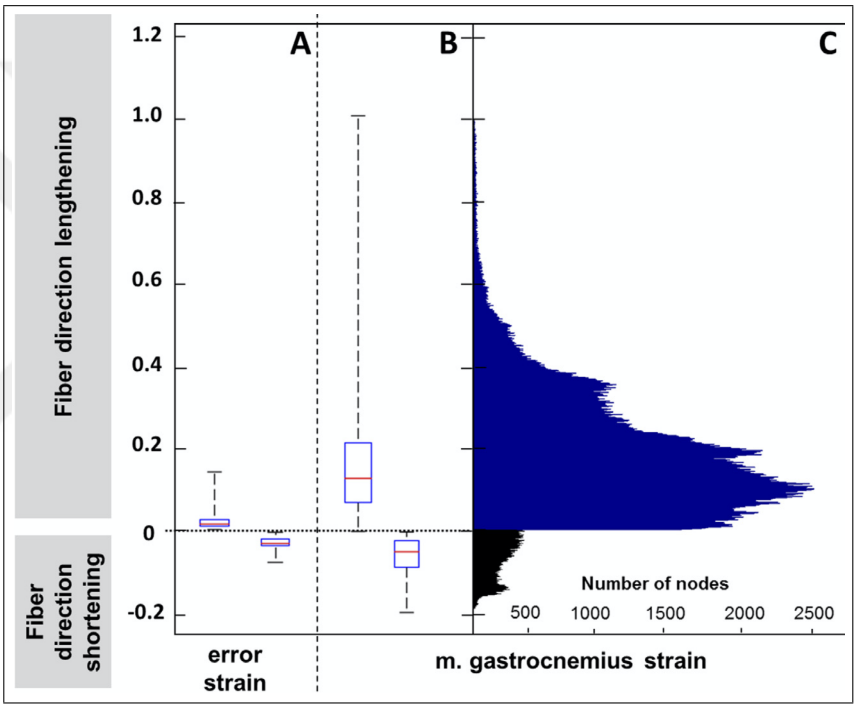

Figure 2.3 Box and whisker plots for (a) error strains and (b) strains along the GM fibers caused by 15% MVC effort. The horizontal line inside each box represents the median strain value; the upper and lower edges of each box itself represent upper and lower quartiles respectively (i.e., the 75th and 25th percentiles), and lines extending from each end of the box (whiskers) indicate the peak values of the principal strains plotted. (c) Distribution of fiber direction strains of different nodes for the pooled data from all subjects.

Table 2.4
Fiber direction strains (mean ± SD) in different muscle parts.

Part[1]	**Pooled**[2]	**A**[3]	**B**	**C**	**D**	**E**
P4	-0.02±0.06	-0.01±0.05	-0.04±0.05	0.02±0.04	-0.08±0.06	-0.01±0.02
P3	-0.01±0.07	-0.02±0.03	-0.07±0.04	-0.01±0.02	-0.01±0.10	-0.01±0.03
P2	-0.01±0.10	-0.01±0.02	-0.09±0.04	-0.05±0.05	0.20±0.10	-0.03±0.02
P1	0.03±0.13	-0.03±0.04	-0.03±0.06	-0.01±0.09	0.27±0.06	0.01±0.04
M1	0.05±0.11	-0.07±0.03	0.07±0.10	0.05±0.05	0.18±0.07	0.07±0.04
M2	0.10±0.09	0.01±0.05	0.16±0.11	0.12±0.06	0.13±0.05	0.06±0.02
D1	0.14±0.11	0.12±0.04	0.20±0.13	0.23±0.10	0.08±0.06	0.01±0.02
D2	0.15±0.16	0.12±0.02	0.42±0.10	0.14±0.04	0.07±0.02	0.02±0.04
D3	0.16±0.19	0.13±0.03	0.43±0.19	0.01±0.07	0.11±0.09	0.01±0.05
D4	0.10±0.12	0.12±0.02	0.12±0.11	0.05±0.02	0.19±0.20	-0.06±0.08

[1] Muscle part: each one of the 10% of the GM volume (P4, P3, P2, P1, M1, M2, D1, D2, D3 and D4), where P4 and D4 represent the most proximal and distal parts, respectively and M1-2 represents the middle parts.

[2] Pooled data: fiber direction strains per each part grouped across all subjects. Significantly different fiber direction strains for different muscle parts are as follows. For P4, P3 and P2: M1 to M2 and D1 to D4; for P1: M2 and D1 to D4; for D1 and D2: P1 to P4 and M2; for D3 and D4: P1 to P4. Therefore, the general nature of the deformation field throughout the GM indicate that proximal muscle parts show significantly different length changes compared to the mid and distal muscle parts and mid muscle parts show that only compared to the less distal muscle parts.

[3] Key deviations from the general nature of the deformation field: For subject A, fiber direction strains in proximal muscle parts are not significantly different from those in the middle parts, but those in the distal parts are. For subject B, no significant difference between the fiber direction strains in P4 and M1, P1 and M2 and middle muscle parts and distal ones. For subject C, fiber direction strains in the proximal muscle parts are significantly different than those in M2, D1 and D2. Unlike the remaining subjects, for subject D fiber direction strains in P1 and P2 are significantly different than those in P3 and P4. For subject E, fiber direction strains in the proximal muscle parts are significantly different only from the middle muscle parts.

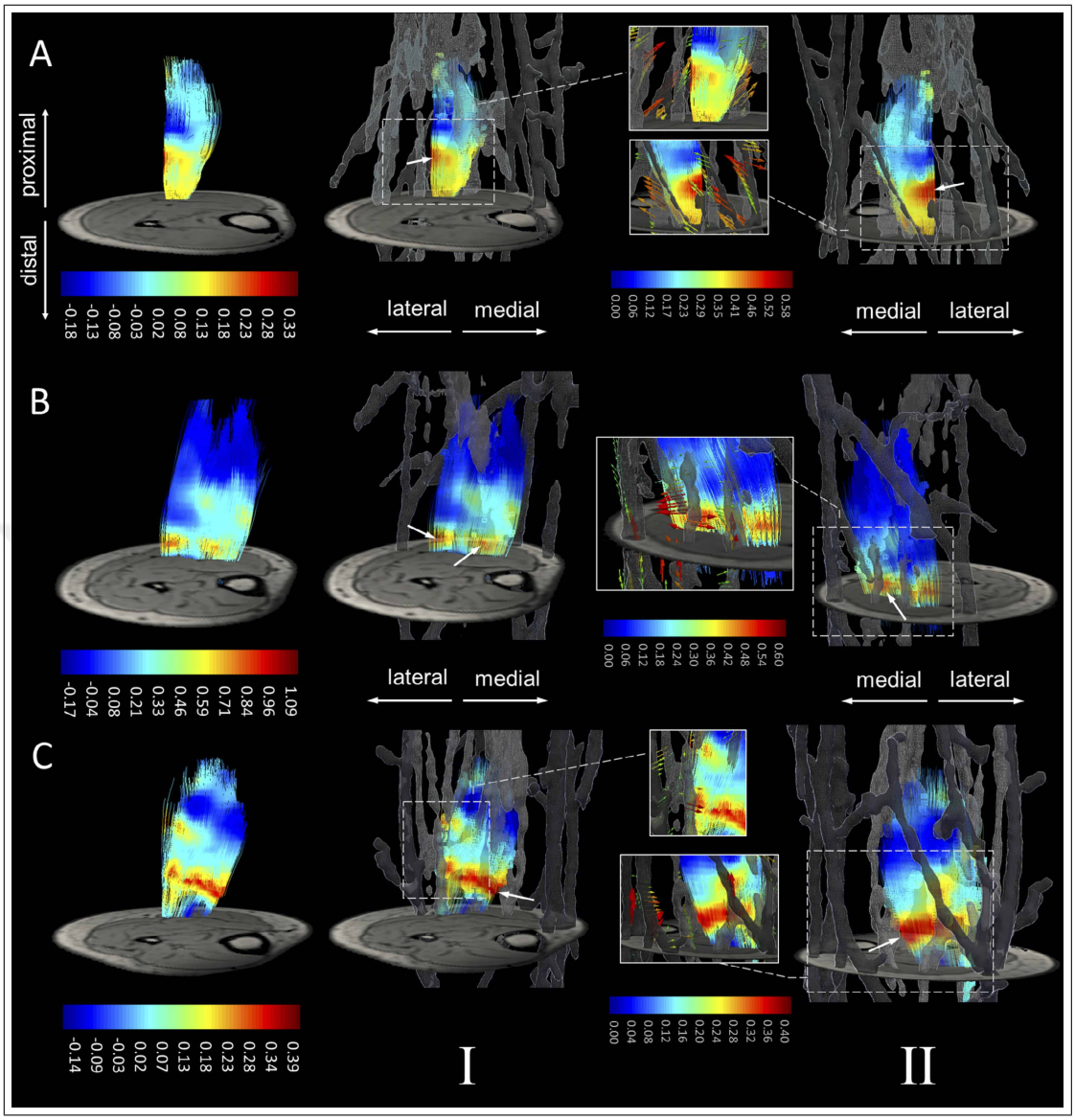

Figure 2.4 Effects of 15% MVC isometric submaximal plantar-flexion activity on GM fascicles and neurovascular tracts for subjects A-C. Fiber direction strain values are mapped on tracked GM fascicles (the leftmost and mid panels show the anterior, and the rightmost panel shows the posterior view) per subject. The mid and the rightmost panels also show the superficial (dark gray) and deep (light gray) NVTs and the continuity of these structures with the GM tissues. The intersections of the NVTs with the GM fascicles are highlighted. The insets (dashed boxes) focus on muscle regions showing high fiber direction strain amplitudes indicating fascicle lengthening. The first principal strains calculated for those NVT sites are visualized using glyphs to indicate presence of myofascial loads. The direction of each glyph is determined by the corresponding Eigen vector. The length of each glyph is proportional to the size of local peak strain. The larger color bars on the left report the fiber direction strains and the smaller ones on the right reports the first principal strains on the NVT structures per subject.

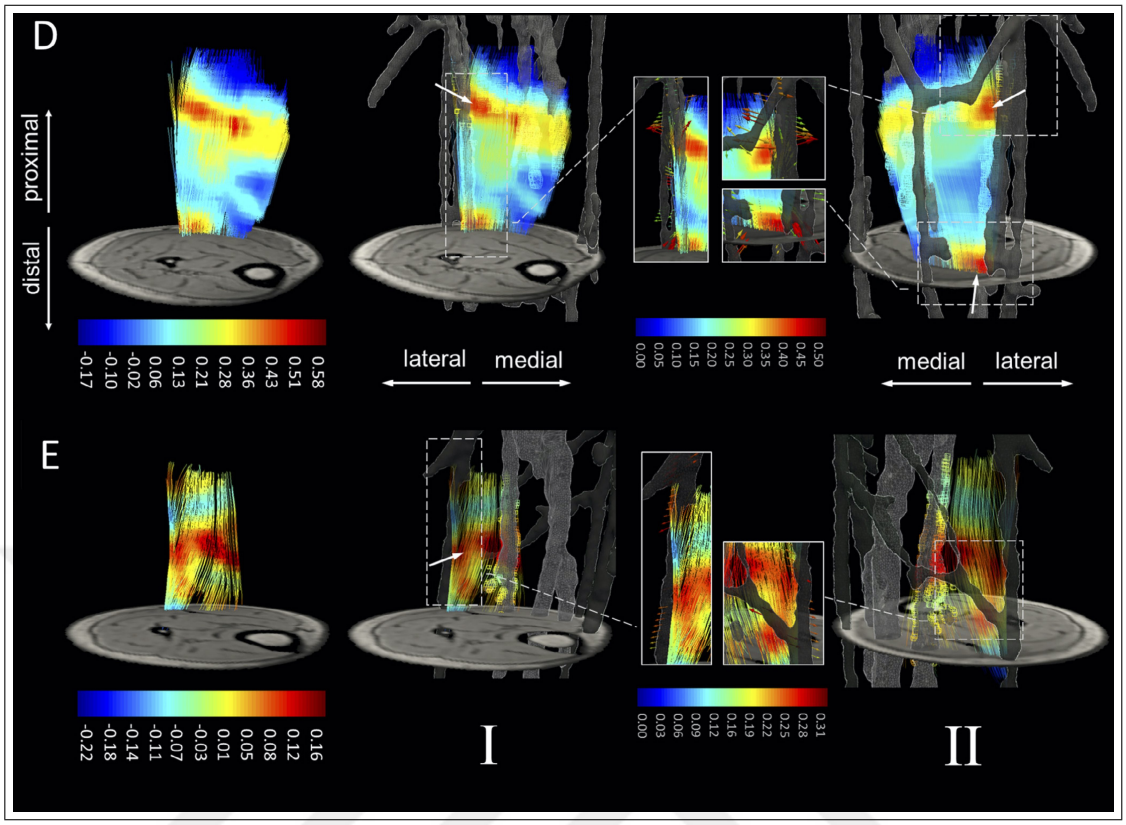

Figure 2.5 Effects of 15% MVC isometric submaximal plantar-flexion activity on GM fascicles and neurovascular tracts for subjects D-E. Fiber direction strain values are mapped on tracked GM fascicles (the leftmost and mid panels show the anterior, and the rightmost panel shows the posterior view) per subject. The mid and the rightmost panels also show the superficial (dark gray) and deep (light gray) NVTs and the continuity of these structures with the GM tissues. The intersections of the NVTs with the GM fascicles are highlighted. The insets (dashed boxes) focus on muscle regions showing high fiber direction strain amplitudes indicating fascicle lengthening. The first principal strains calculated for those NVT sites are visualized using glyphs to indicate presence of myofascial loads. The direction of each glyph is determined by the corresponding Eigen vector. The length of each glyph is proportional to the size of local peak strain. The larger color bars on the left report the fiber direction strains and the smaller ones on the right reports the first principal strains on the NVT structures per subject.

2.4 Discussion

Tracked are whole fascicles originating from the superficial GM aponeurosis, running through antero-inferior direction and inserting on the deep aponeurosis. Their 3D description agrees well with GM muscle structure [138], but represent a group (approximately 20%) of GM fascicles located in the mid-GM belly. Possible distribution of fiber activation within the muscle during the tested submaximal GM activity should be considered. The size principle indicates activation intensity as a key factor for motor unit firing [139]. Lower intensity forces in human GM is maintained by the recruitment of small and intermediate muscle units through activation of Type I and Type IIa muscle fibers [140]. Although approximately half of the GM is comprised of Type-I muscle fibers [141], spatial distribution of different types of muscle fibers and possible effects of that on distribution of activity within the muscle is not well known. However, recent literature helps characterization of fiber activity in the presently studied GM part. Active muscle unit [142] and muscle fiber clusters were shown in GM regions during various efforts [143, 44, 45, 144]. During submaximal isometric fatiguing plantar flexion at %50 MVC, distal GM parts exhibited more fatigue resistant characteristics than the proximal parts [145]. Profound activation in distal GM parts during standing indicates that slower motor units are more likely to be found distally whereas; faster ones are located in the proximal regions [146, 45]. support this by showing a shift in localized activity towards more proximal GM parts for increased submaximal plantar flexion intensity (20-60% MVC). Their results show activity around the central GM region for 20% MVC. These findings indicate that on imposed 15% MVC, the GM part studied presently was comprised of activated fascicles.

Using ultrasound imaging, the GM architecture and fascicle length changes were studied elegantly. Rana et al. (2013) assessed 3D fascicle orientations in the GM and showed that submaximal isometric plantar-flexion causes more pronounced changes in fascicle pennation angle in the distal regions compared to the proximal regions [49]. Hodson-Tole et al. (2016) showed in passive GM that for the same muscle-tendon unit length changes imposed, fascicle length changes were greater with ankle motion than knee motion [144]. Notably, those findings indicate differential effects regionalized

within the GM, which shows parallelism with our present findings. To the best of our knowledge, this is the first study, which reports strain occurring along fascicles of an activated human muscle in vivo. On isometric activation, muscle fibers will undergo shortening [147]. Nevertheless, instead of a uniform shortening, our results show a heterogeneous strain distribution including also local lengthening in several regions of GM fascicles. Therefore, loads suggest an impact on the fascicles that counteract sarcomere shortening. In the undeformed state, passively extended knee position imposes a stretch on the GM and changes the relative position of the proximal muscle belly with respect to its surroundings. Consequently, the muscle's epimuscular connections in the proximal part are stretched proximally imposing distally directed epimuscular myofascial loads on that part. Pamuk et al. (2016) showed that this causes local lengthening in the proximal and shortening in the distal ends of the GM fascicles. In contrast, the general pattern of fascicle strain shown presently is the opposite. Therefore, 15% MVC effort could have changed the epimuscular myofascial loads acting on the muscle. Two effects of this active condition are relevant. First is the shortening of the tracked mid-GM belly fascicles causing their proximal and distal ends to displace in the distal and proximal directions, respectively. This can diminish distally directed epimuscular loads developed in the undeformed state on the proximal part of the GM. Second, is the relative position changes with respect to the SOL causing distally directed epimuscular loads to act in the distal parts of the GM. This is supported by [48]. In extended knee position, their findings indicate a more pronounced displacement of the GM aponeurosis in the proximal direction. Consequently, shortening of the sarcomeres located proximally are plausibly accompanied by the ones distally located being restrained from shortening caused by activation. However, such passive epimuscular forces alone cannot explain local lengthening observed. Collagenous intermuscular connections stretched constitute a stiff pathway for transmission of also the contractile forces between synergists [15]. Note that, at submaximal activation levels, those pathways have been shown to be relatively more effectual [148]. During sustained submaximal plantar-flexion, the SOL is activated more than the GM, producing a bigger contribution to ankle torque [149]. Transmission of some of its active force onto the distal parts of the tracked GM fascicles can elevate the distally directed epimuscular loads and cause the local lengthening observed. Such inter-synergistic myofascial force

transmission has been shown not only between passive [61, 57] but also between active human calf muscles [47, 150], which supports this reasoning.

On the other hand, the present data provides body to that reasoning. The NVTs visualized with their first principal strains exemplify main structures facilitating intermuscular mechanical interactions, their continuity inside the GM and the presence of myofascial loads. These loads are transmitted to the GM tracts at their NVT intersections and plausibly are also spread along the muscle via their continuity with the ECM. This is responsible for the general nature of the deformation field throughout the GM, but also can explain the deviations from that and the differences among the subjects. One such deviation is the peak fiber direction lengthening shown in the proximal muscle parts in subject D. For this subject the NVT intersections are concentrated in those parts and the first principal strains substantiate around that region suggesting high myofascial loads causing particular fascicle lengthening. A similar concentration of NVT intersections and high myofascial loads are conceivable for Subjects A and E in the medial and distal muscle parts. For subjects B and C, such NVT intersections are positioned in the distal muscle parts in agreement with the general nature of the deformation field, but apparently elevating the amplitude of fascicle lengthening in subject B in that part compared to the other subjects.

Inter-subject variability of fascicle strain amplitudes and distributions not agreeing with the general pattern may also be associated with other factors. First, inter-individual differences in the calf muscle-tendon complex anatomy are plausible. Contribution of the gastrocnemius and SOL muscles to the formation of the Achilles tendon is individual dependent [151]. Cummins et al. (1946) report that for about half of their participants, the SOL makes the dominant contribution, which indicates a long distal gastrocnemius aponeurosis [152]. For about a third, the muscles contribute equally indicating direct attachment of gastrocnemius fibers to the tendon i.e., no distal gastrocnemius aponeurosis. This implies presence of differences in e.g., fiber length and orientation. It is also known that inter-calf mechanical interactions are plausible via the Achilles tendon [153, 154]. Yet, presently the ankle was restrained, which limits such interaction. Second, although care is taken to unify joint positions and activa-

tion levels across the participants, differences in initial strains ascribed to variability of intramuscular tissue mechanical properties in the undeformed state can cause inter-subject variability of fascicle strains [2]. Third, properties of epimuscular connections are complex involving non-linear mechanical characteristics [155] and inhomogeneous distributions [156]. Consequently, a comparable stretch on the epimuscular connections may yield much larger or smaller amplitudes of epimuscular loads to act on different parts of the muscle in different individuals. Pre-strain in the epimuscular connections [14] may e.g., avoid distally directed epimuscular loads on the proximal GM to be balanced by the activation and limit shortening in this part as observed in subject D. Note also that, the factors addressed above are not independent from each other and considering their interaction suggests that intrinsic differences among different individuals are highly plausible. Previous measurements of human muscle force directly at the tendon do indicate that such differences are present despite identical testing conditions [157]. However, the causes for inter-subject variability of along fascicle strain should be further studied. A specific assessment of how sensitive the strain distributions are to the initial starting point can help understanding the role of tissue properties.

We conclude that submaximal plantar flexion activity causes a heterogeneous distribution of strain within the GM fascicles. The GM is reported to behave close to isometric during in vivo activities [46]. Therefore, our test condition is relevant to understand how the GM functions in vivo. However, effects of other conditions can be substantial. First, a different distribution of strain can be expected in other knee and ankle angle combinations because different amplitudes and directions of epimuscular loads are plausible in the altered relative position of the muscle with respect to its surroundings [158, 18]. Second, regional patterns of recruitment were shown to change in GM during dynamic tasks [159]. Therefore, an interaction between mechanical behavior and activation pattern is also plausible, which will influence the intra-fascicular strain patterns during different activities. Such condition dependent strain heterogeneity along the fascicles implies that sarcomeres of a muscle fiber may attain different lengths and have differing force production capacities. As shown in earlier animal experiments [24], this has major functional implications including unequal forces exerted at the proximal and distal ends of the bi-articular muscle and hence a differential

contribution to joint moments. In addition, strain heterogeneity across the fascicles implies that mean sarcomere lengths of different muscle fibers may differ. This was shown to affect muscle's length range of force exertion [35] and hence is relevant for the muscle's excursion. Limited joint range of motion is a major pathology for several conditions. Assessment of serial and parallel fascicle strain heterogeneity can make a significant contribution to our understanding of the etiology of those conditions and mechanisms of the treatment techniques. This is highly relevant for e.g., spastic cerebral palsy patients [160, 161] and the developed techniques can be used to relate limited excursion to fascicle strain with e.g., passive state isometric testing. Investigation of local deformations in the GM and other lower leg muscles in active conditions may provide a better insight to evaluate muscle injuries of athletes [162, 163]. In sum, the present approach and indicated fascicle strain heterogeneity has numerous implications and new work is indicated in several conditions in health and disease.

3. IN-VIVO ALONG MUSCLE FASCICLE STRAIN HETEROGENEITY IS NOT AFFECTED BY IMAGE REGISTRATION PARAMETERS: ROBUSTNESS TESTING OF COMBINED MAGNETIC RESONANCE-DIFFUSION TENSOR IMAGING METHOD

3.1 Introduction

The sarcomere is the smallest contractile unit of musculoskeletal force generation, determined by its length changes. Arranged in series, sarcomeres make up muscle fibers, which come together to form fascicles that bundle into a muscle. Therefore, quantifying sarcomere length changes is central to understanding skeletal muscle function with major implications to pathology, diagnosis, treatment and performance. Although sarcomere length-force production relationship has a long-standing history [164], understanding its characteristics in-vivo is still a challenge as a non-invasive quantification of sarcomere length changes over large muscle sections is required. Converging to such ideal, a minimally invasive hybrid imaging study reported that in-vivo fascicle length change in the muscle fiber direction is a linear predictor of sarcomere length changes over a moderate field of view (FOV) [165]. Moreover, their findings provide direct evidence on the heterogeneity of in-vivo sarcomere length distribution in human, as was reported in mice [166]. Considering profound relevance of sarcomere length heterogeneity to joint range of motion [35], non-invasively quantifying local fascicle length changes in-vivo over a large FOV is key to understanding muscle function.

Magnetic resonance imaging (MRI) is a powerful tool for quantifying local length changes (i.e., strain) by probing the velocity of the soft tissue based on phase information across multiple time frames [167]. Using highly under-sampled image reconstruction, such velocimetry-MRI methods can measure muscle kinematics in short acquisition times [55]. Yet, in general, these scans require cyclic soft tissue displacements

for proper velocity encoding. Therefore, test participants have to perform highly consistent joint movements or isometric muscle contractions repetitively. Furthermore, isotropic resolution remains limited due to signal-to-noise-ratio constraints and the strains derived do not meaningfully match muscle architecture. 3D muscle architecture information of tracked fascicles in a steady muscle encoded using diffusion tensor imaging (DTI) is challenging to be fed to velocity-based local strains given the dynamic nature of the velocimetry acquisitions.

Relying on image analysis rather than specialized MRI scans, image registration gives an alternative way to quantify morphometrical changes in soft tissue. From non-rigid registration of a pair of T1-weighted musculoskeletal MR images acquired at two successive conditions (deformed and undeformed) in the same scan session, a high-resolution 3D displacement field at the voxel scale of 1mm. This can be further derived into a deformation gradient field, a fundamental quantity of continuum mechanics. For muscle fibers that undergo large deformations [168], Green-Lagrange strain tensors can be calculated locally using this deformation gradient field across muscle tissue [61, 57, 60]. Strain component along muscle fiber direction can be calculated by using DTI. Recently, such MRI-DTI analyses were utilized to study along muscle fascicle strains in human medial gastrocnemius (GM) muscle in-vivo [82, 87]. These findings showed in concert with an anticipated sarcomere length inhomogeneity [165, 166, 2], non-uniform strains along human GM fascicles in-vivo.

MRI-DTI method is a powerful non-invasive tool for quantifying fascicle length changes over a large FOV [82]. Earlier, non-rigid MR image registration was commonly used in neuroanatomy and via Jacobian determinants of the deformation field yielding local volumetric changes [90, 169]. Highly popular use of such tensor- and voxel-based morphometry in human brain [90, 169, 170] has triggered considerable research and debate on how these measurements are influenced by different MRI scanners [171, 172], software selection [173, 174, 175] and post-processing parameter settings [176, 177]. Community standards were established for post-processing [178, 179] and reporting [180] of morphological changes in human brain. Despite that the MRI-DTI method could have a similar potential impact to the study of in-vivo muscle function, such

application-specific validations concerned with the practical aspects of the analysis workflow are yet to be made.

MRI-DTI non-rigid registration approach implements extensively the demons algorithm [128], which employs joint histogram matching to accurately resolve large local deformations between MR image pairs [129]. Along with standard deviation (σ) of the Gaussian kernel used for displacement field smoothing as a regularization step, an additional normalization factor (α) aims to improve alignment stability of the edge features [98]. Robustness of strain calculations against rigid body motion [57], estimation of known deformation field [57], participant repositioning [60] and random errors [87] was tested. Yet, effects of tuning parameters were not studied. Decreasing the locality of the registration [129], increasing σ can limit strain amplitudes [57]. However, the combined effect of varying both parameters may alter both amplitude and heterogeneity of muscle fiber direction strains. Consequently, it is crucial to study the effects of these parameters on muscle fiber direction strain distribution patterns.

The goal was therefore, to investigate the capability of demons algorithm in quantifying muscle fiber direction local length changes. The specific aims were (1) to assess the consistency of the findings among different data analysis workflows and to provide an open source workflow, and (2) to test the hypothesis that although σ and α tuning parameters may affect the strain amplitudes, the pattern of muscle fiber direction local length change distributions is reproducible.

3.2 Methods

3.2.1 Parameter analysis using the reference data

Applying the data from Pamuk et al. (2016) to a different analysis workflow one-at-a-time variations of tuning parameter configurations $C^{\langle\alpha,\sigma\rangle} \mid \forall_{(\alpha,\sigma)} \in \{4, 6, 8, 10\}$ were assessed:

1. Fiber direction strains along the GM tracts (ε) were utilized to study (i) the robustness of the results against a different analysis pipeline and (ii) the influence of tuning parameters at a broader sense for $C^{\langle\alpha,\sigma\rangle} \mid \forall_{\alpha=\sigma} \in \{4, 6, 8, 10\}$. Four configurations corresponding to these parameter pairs are denoted by $C^{\alpha=\sigma}$.

2. To robustly assess the central tendency evolution of deformation fields in response to the variation of tuning parameters, *median fiber direction strains at different muscle parts* ($\tilde{\varepsilon}_{part}$) were constructed as heatmaps.

3. For a qualitative interrogation of distribution shape differences, *ridgeline kernel density plots* across all tested parameter settings were plotted on selected muscle parts with a focus on deviating $\tilde{\varepsilon}_{part}$ values.

4. To identify the nature and significance of the tuning parameter effects on the heterogeneity of deformation fields, *hierarchical shift function analysis* was performed per participant by modeling (modified z-score standardized and downsampled) fiber direction strains as a function of different muscle parts and binary pairings of $C^{\alpha=\sigma}$.

5. To assess whether the deformation heterogeneity persists across all $C^{\langle\alpha,\sigma\rangle}$ or if the variations undergo systematic changes, the *number of significantly different pair-wise comparisons in different muscle parts* were presented as heatmaps.

3.2.2 Data analysis workflow

The reader is referred to Pamuk et al. (2016) for detailed descriptions of the experimental design, MRI acquisition protocols, and the reference data processing workflow [82].

The 3D displacement fields were obtained by registering deformed- and undeformed-state (knee flexion and extension, respectively) anatomical images using an open-source implementation [129] of demons non-parametric image registration [128] in MATLAB (R2015b, The MathWorks Inc., Natick, MA). The registration was repeated for every $C^{\langle\alpha,\sigma\rangle}$ combination studied by changing only one parameter at a time. Subsequently, 3D voxel-wise Green-Lagrange strain tensors were calculated from the resulting displacement fields in the native space of the deformed-state structural images.

Diffusion-weighted images (DWI) were denoised using the joint Rician LMMSE filtering [181] previous to the standard least-squares diffusion tensor (DT) estimation. Muscle fiber tractography was then performed with the following constraints: Fractional Anisotropy (FA) > 0.19, tract length of 30 - 50 mm, and maximum curvature of 1 deg/mm. Seed points were located at the GM muscle belly with a 2 mm margin from the superficial and deep aponeuroses [182]. Step length was set to 0.7 mm, corresponding to half of the in-plane resolution. All DTI processing and fiber tracking was performed in 3D Slicer release v4.4 [183].

To project strain values to the fiber tract segments, strain tensors were first interpolated between the off-grid tract nodes using inverse distance weighted interpolation. Finally, the unit tangent vectors calculated between successive tract nodes were used to extract strain components in respective fiber directions. These operations were performed using in-house MATLAB code, reimplemented from previously written C++ modules in the VAVframe framework [184].

3.2.3 Statistical analyses

3.2.3.1 Median fiber direction strains at different muscle parts. As a robust measurement of central tendency [185], the median of nodal strains at every muscle part was reconstructed as annotated heatmaps across $C^{\langle\alpha,\sigma\rangle}$ for each participant. The colormaps across muscle parts (i.e., each vertical stripe) were individually adjusted for the respective $C^{\langle\alpha,\sigma\rangle}$ to allow an easy assessment of trend recurrence across configurations.

3.2.3.2 Preprocessing. To inform the statistical comparisons with the spatial organization of nodal strains, tracked fascicles of the GM were divided into 10 equal parts (P4-1, M1-2, and D1-4) along the long axis. P4, D4, and M1-2 represent the most proximal, the most distal, and mid parts, respectively.

Upon preliminary inspection, kernel density estimates of strain distributions in different muscle parts revealed sizable amplitude differences along with varying outlier effects and shape asymmetry between different $C^{\langle\alpha,\sigma\rangle}$ outputs. To robustly bring different $\varepsilon^{\langle\alpha,\sigma\rangle}$distributions within a comparable magnitude scale for the assessment of heterogeneity across these muscle parts, fiber direction strains were transformed to modified z-scores (z) given by:

$$z_i = \frac{\varepsilon_i - \tilde{\varepsilon}}{1.4826 XMAD} \tag{3.1}$$

where ε_i is the ith nodal fiber direction strain, $\tilde{\varepsilon}$ and MAD are the median and median absolute deviation calculated from the strain distribution of all tracts, respectively [186]. Following the standardization, tract node coordinates were treated as point clouds and reduced to 1400 points (limited by the number of nodes in participant D-D4) at each muscle part using interval down-sampling [187] to allow for a balanced comparison between them.

3.2.3.3 Ridgeline kernel density plots. To compare probability density functions of $z^{\langle\alpha,\sigma\rangle}$, kernel density estimations [188] were visualized using ridgeline plots (Python 3.6.12). To exemplify distribution shape differences across $C^{\langle\alpha,\sigma\rangle}$, representative muscle parts from three participants were selected. Ridgeline plots of all participants and muscle parts including $z^{\langle\alpha,\sigma\rangle}$ before interval down-sampling and the original $\varepsilon^{\langle\alpha,\sigma\rangle}$ distributions were made available as an interactive dashboard [189].

3.2.3.4 Hierarchical shift function analysis. Shift function (SF) analysis is a powerful graphical analysis tool to measure differences at any location in the distributions in absence of shift or scale parameters [190]. A multi-level expansion of this method enables comparing multiple distributions between two dependent conditions to interrogate the overall effect, namely hierarchical shift function (HSF) analysis [191]. Presently, we applied the HSF in R v3.6.1 to compare all the binary pairings of $z^{\alpha=\sigma}$ across different muscle parts. Following a median unbiased quantile estimation (9 boundaries dividing the statistical distribution into 10 equal chunks) for every $z^{\alpha=\sigma}_{part}$ distribution [192], a one-sample t-test is performed on the 20% trimmed means of quantile differences between binary pairings of $z^{\langle\alpha,\sigma\rangle}$ across muscle parts. Multiple comparisons between 9 consequential one-sample t-tests were then adjusted for significance using Hochberg's procedure [193] and confidence intervals (CI) were calculated at each quantile, yielding the group shift function. Note that the comparison is performed on the standardized distributions, where each score represents how many median absolute deviations away is the corresponding strain value from the median strain of the whole tracked fascicle. Therefore, significant quantile differences detected by HSF can be ascribed to the impact of tuning parameters on the heterogeneity of the deformation fields across muscle parts. Moreover, the nature of the effect can be characterized via group shifts.

3.2.3.5 Number of significantly different pair-wise comparisons. An analysis of variance test (Kruskal-Wallis) among different muscle parts was followed by Dunn-s posthoc procedure on all $C^{\langle\alpha,\sigma\rangle}$ outputs. Corresponding heatmaps were gen-

erated to evaluate whether the tuning parameters had a preferential influence on the number of significant pair-wise differences between different muscle parts.

3.2.3.6 Reproducibility. All the source code (at v1.0) and intermediate derived data to reproduce the figures and analyses in the article are publicly available, and can be executed online without installation [194]. Please refer to the code repository for the instructions.

3.3 Results

Visual inspection and statistics summary of Figure 3.1 reveals the following:

(i) *Strain amplitudes at the reference parameter configuration* $C^{\langle 6,6\rangle}$ peak amplitudes are 21% shortening and 67% lengthening, both manifested in participant C, yielding the widest within-participant distribution range of 88%. The smallest shortening of 15% is observed in participant D-E, whereas participant B shows the lowest local lengthening of 28% and the narrowest within-participant range of 45%.

(ii) *The general pattern for the deformation field* - the positive strains are encountered in the proximal muscle parts, while negative ones mostly are towards distal parts of the tracked fascicles.

(iii) *Inter-participant differences* - variability is apparent. For example, participants D and E show lengthening in the distal parts, not only in the proximal parts.

(iv) *Effect of the tuning parameters*: As $C^{\alpha=\sigma}$ increases from 4 to 10, ε values for all participants drop substantially in amplitude (e.g., for participant B, peak shortening and lengthening equal 43% and 130% ($C^{\langle 4,4\rangle}$) whereas 1% and 9% ($C^{\langle 10,10\rangle}$), respectively.

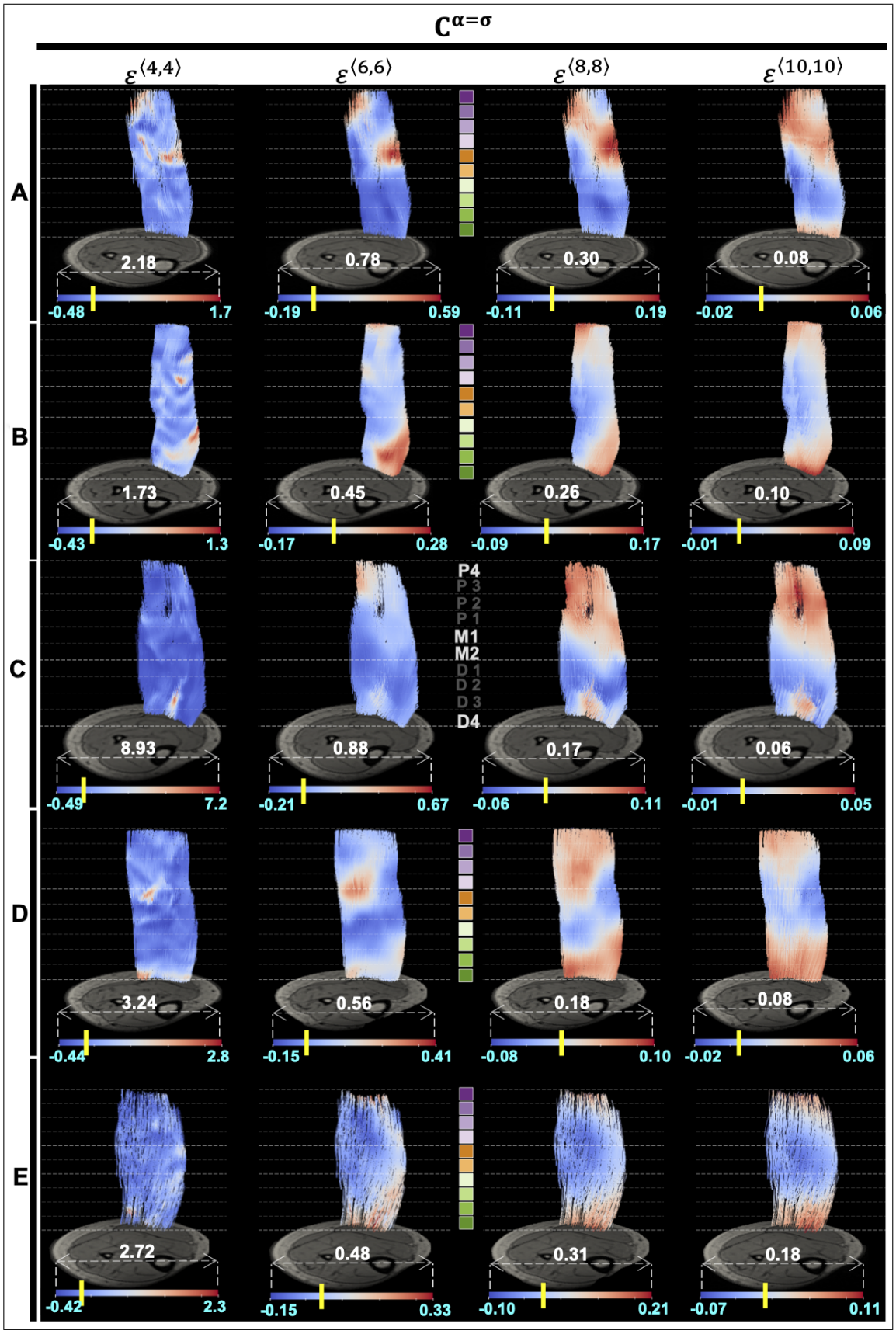

Figure 3.1 Serial distribution of local fiber direction strains (ε) along tracked fascicles of the medial gastrocnemius (GM) on knee extension are visualized across participants (participants A-E, rows) and for tuning parameters where α equals σ ($C^{\alpha=\sigma}$, columns). Horizontal color-bars show min-max (turquoise), range (white) and zero-crossing (yellow) of the respective ε distributions. Dashed white lines indicate 10 muscle parts along with corresponding tags and categorical color palettes.

Figure 3.2 compares the breakdown of median fiber direction strains at different muscle parts for each parameter configuration ($\tilde{\varepsilon}_{part}^{\langle\alpha,\sigma\rangle}$) by annotated heatmaps. The strain amplitude attenuation in response to increasing $C^{\langle\alpha,\sigma\rangle}$ is valid for majority of $\tilde{\varepsilon}_{part}^{\langle\alpha,\sigma\rangle}$ (e.g., for participant A, $\tilde{\varepsilon}_{M1}^{\langle4,4\rangle}$ =26% whereas $\tilde{\varepsilon}_{M1}^{\langle10,10\rangle}$=2% and, $\tilde{\varepsilon}_{D2}^{\langle4,4\rangle}$=-14% $\tilde{\varepsilon}_{D2}^{\langle10,10\rangle}$=0%). This is valid also for exclusive changes of either tuning parameter (e.g., for α=4 for participant C, $\tilde{\varepsilon}_{D3}^{\langle4,\sigma\rangle}$ values equal 28, 19, 13 and 10%, as σ increases from 4 to 10) and for σ=4, $\tilde{\varepsilon}_{D3}^{\langle\alpha,4\rangle}$ values equal 28, 19, 14, and 10%). Therefore, tuning parameters comparably affect strain amplitudes. Note however that exceptions to this general pattern exist. A major example is participant B in which, parts P4 and P3 show that increasing $C^{\langle\alpha,\sigma\rangle}$leads to not only a strain amplitude change but also a sign change: $\tilde{\varepsilon}_{P3}^{\langle4,4\rangle}$=-13% whereas, $\tilde{\varepsilon}_{P3}^{\langle10,10\rangle}$=5%. Much less pronounced other examples include participant A ($\tilde{\varepsilon}_{P2}^{\langle4,4\rangle}$=-2% whereas, $\tilde{\varepsilon}_{P2}^{\langle10,10\rangle}$=4%), participant C ($\tilde{\varepsilon}_{M1}^{\langle4,4\rangle}$=-5% whereas, $\tilde{\varepsilon}_{M1}^{\langle10,10\rangle}$=2%), while e.g., participant E ($\tilde{\varepsilon}_{P3}^{\langle4,4\rangle}$=-3% whereas, $\tilde{\varepsilon}_{P2}^{\langle10,10\rangle}$=1%) is considered to indicate a fluctuation around 0 strain instead of a sign change. To address the mechanism for such sign change, Fig. 3 visualizes kernel density curves of every $z^{\langle\alpha,\sigma\rangle}$ distribution within muscle parts P4, M1 and D4, for participant B.

$z_{P4}^{\langle\alpha,\sigma\rangle}$ distribution shapes indicate that the bulk of the distribution moves from left to the right of the zero-line at $C^{\langle6,6\rangle}$ and stabilizes there with a gradually increased right-skewness as the parameters increase. Therefore, past $C^{\langle6,6\rangle}$, negative median strains yield positive median strains in part P4 (Figure 3.2), which mechanism affects also P3-P1 in participant B. Note that, for other parts exemplified in Figure 3.3, this effect is not valid, hence no sign change of strains occurs.

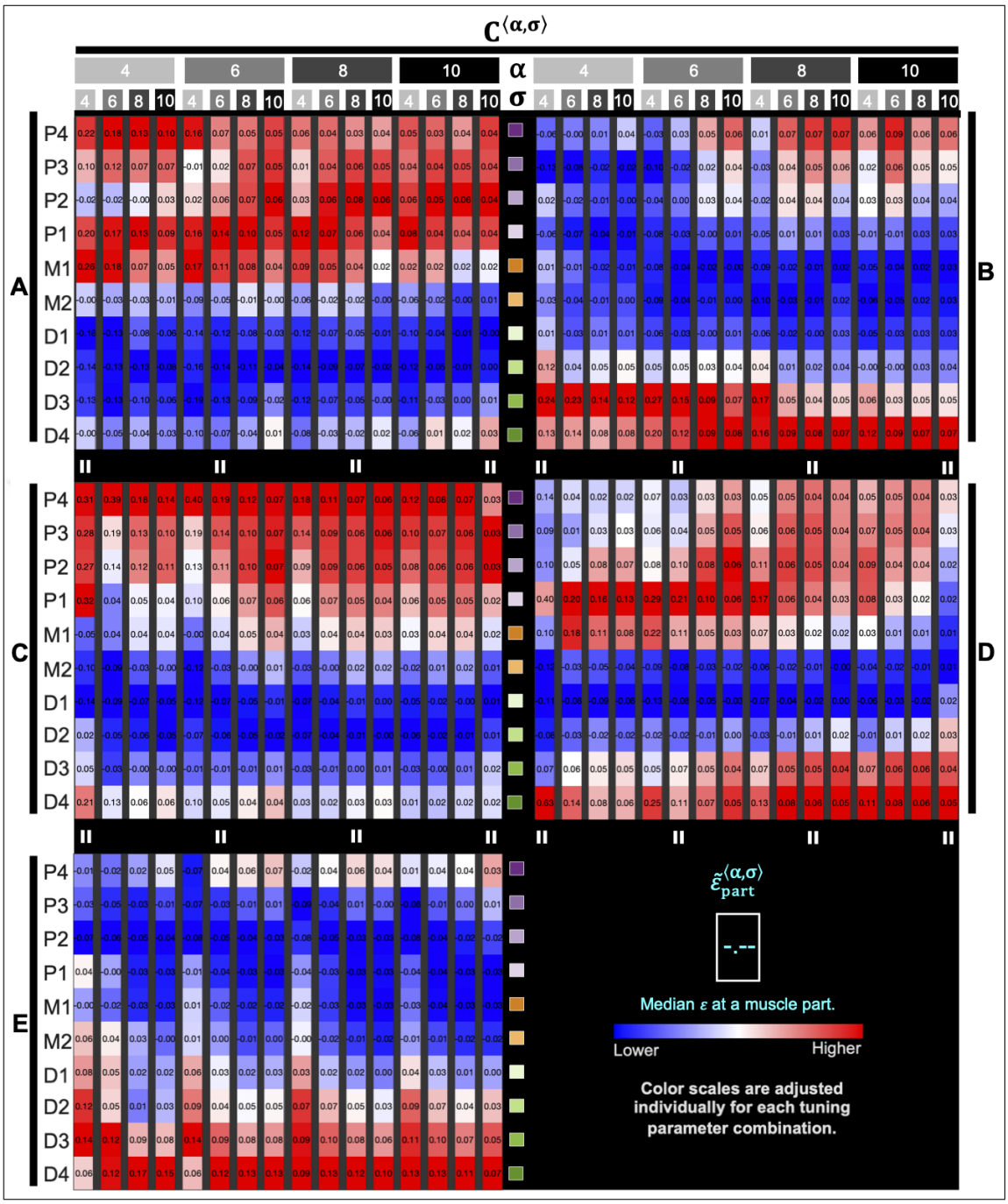

Figure 3.2 Annotated heatmaps plot median fiber direction strain values at each muscle part ($\tilde{\varepsilon}^{\langle\alpha,\sigma\rangle}_{part}$) across all tuning parameter configurations ($C^{\langle\alpha,\sigma\rangle}$, columns). The color scales are adjusted independently per tuning parameter combination to inspect the consistency of proximo-distal $\tilde{\varepsilon}^{\langle\alpha,\sigma\rangle}_{part}$ patterns against parameter changes. The $C^{\alpha=\sigma}$ pairs are indicated by white quotation marks for the reader's convenience.

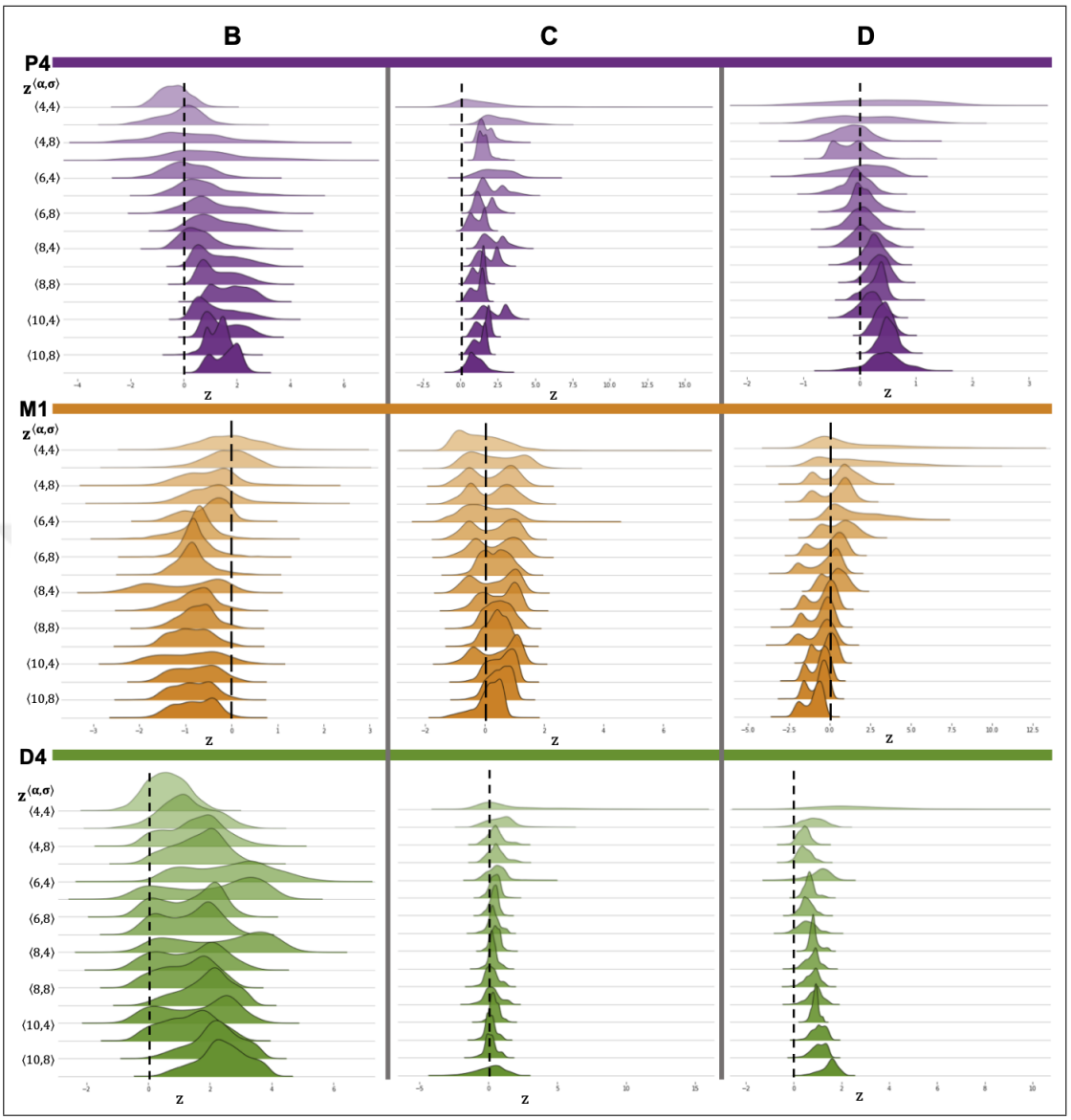

Figure 3.3 Kernel density ridgeline plots of modified z-score distributions across all the tuning parameter combinations ($z^{\langle\alpha,\sigma\rangle}$) are displayed for the P4, M1, and D4 muscle parts (rows) of the participants B-D (columns). The horizontal axis limits of each panel are determined individually by the min-max across all the density plots.

Figure 3.4 shows the number of significantly different pair-wise comparisons in different muscle parts, which indicates that changes to that caused by increasing $C^{\langle\alpha,\sigma\rangle}$ are limited. Moreover, those changes are rather arbitrary and no $C^{\langle\alpha,\sigma\rangle}$ dependent systematic pattern can be discerned from these heatmaps. For participant E, part D3 shows the maximum, whereas for participant A, parts P4-M1 show the minimum significant pairwise differences (14 and 5 out of 16 parameter pairs, respectively).

The absence of a monotonic change in the number of significant differences caused by increasing $C^{\langle\alpha,\sigma\rangle}$ suggests that the heterogeneity of strain distribution along the tracked fascicles is not determined by parameter configurations.

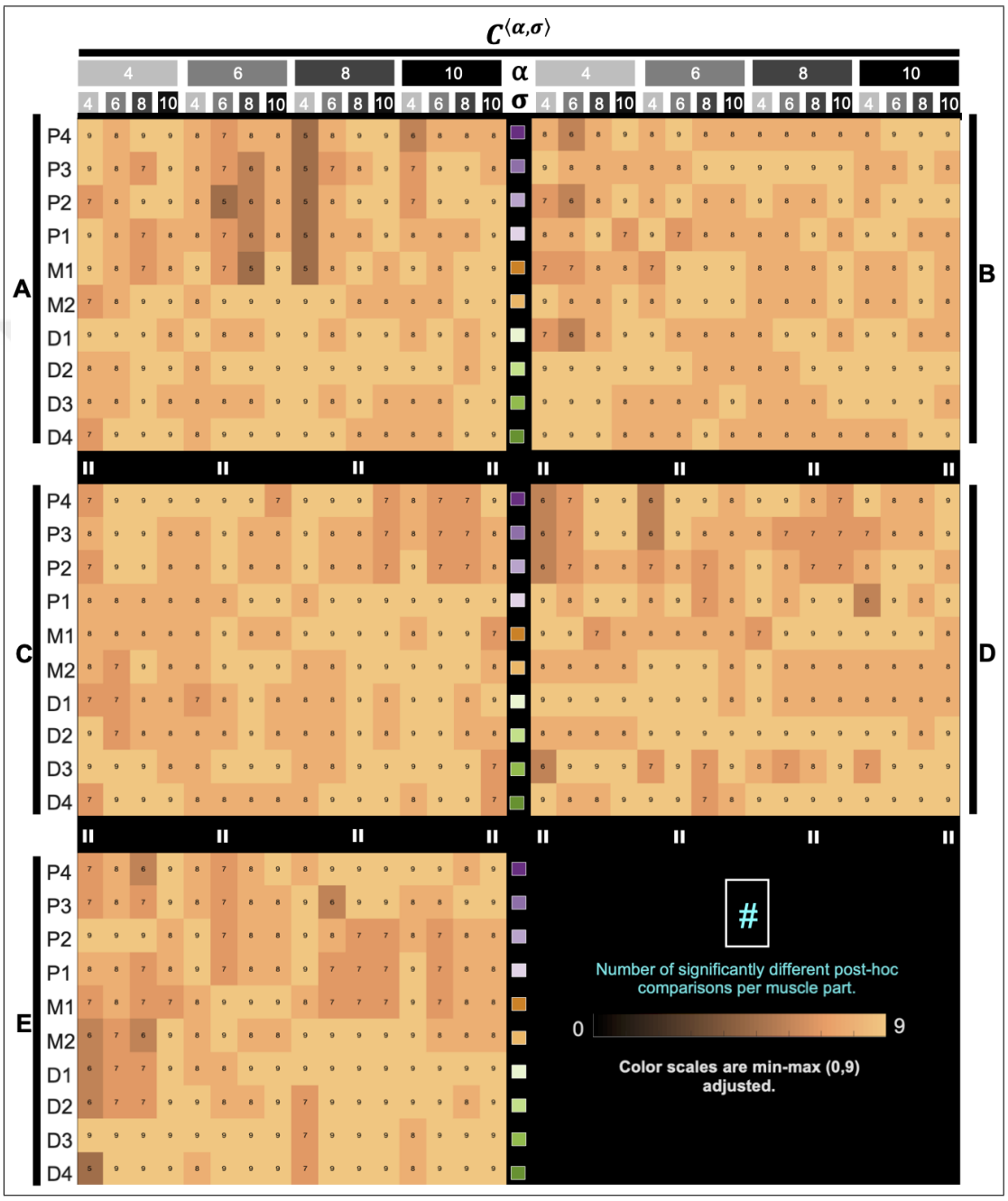

Figure 3.4 Number of significant post-hoc comparisons across muscle parts are shown for the tuning parameter combinations as annotated heatmaps per participant. The color scales are adjusted to min-max of 0-9, as the maximum possible number of significant post-hoc differences for 10 groups is 9 (i.e., one muscle part can be significantly different than all the remaining 9 muscle parts at the most).

Figure 3.5 aims at exemplifying using hierarchical shift function analysis (Figure 3.5a) and showing the nature (Figure 3.5b-c) of the effects of increasing $C^{\langle\alpha,\sigma\rangle}$ on the heterogeneity of deformation field across different muscle parts. Each strain quantile involves from each muscle part, the lowest 10% of the strains to the highest 10%, in 10% increments, i.e., 9 strain quantiles represent one participant per $C^{\langle\alpha,\sigma\rangle}$. For an assessment across different muscle parts, each represents mean z-score differences of the corresponding $C^{\alpha=\sigma}$comparison.

A strain quantile with a confidence interval (CI) that contains zero is one that different $C^{\langle\alpha,\sigma\rangle}$ yield no significant effects across muscle parts. Conversely, if the CI of a strain quantile excludes zero, significant effects across muscle parts occur leading to effects also on fiber direction strain heterogeneity. Per $C^{\alpha=\sigma}$ comparison, this is represented by a fishbone plot collectively. For participant C, such shift function analysis for $C^{\langle4,4\rangle}$ vs. $C^{\langle10,10\rangle}$ statistically shows the net effect of tuning parameters on strain heterogeneity across muscle parts, to include significant effects for the last two quantiles (Figure 3.5a). This indicates that only the z-scores form the highest 20% of strains change their position within the distribution. Therefore, the effect of increased $C^{\langle\alpha,\sigma\rangle}$ is not only on strain amplitudes, but also on fiber direction strain heterogeneity across muscle parts. The mechanism of this analysis is as follows: Figure 3.5b illustrates how distribution quantile differences determine the shape and position of an individual shift function for participant C, part D4: subtraction of $z_{P4}^{\langle10,10\rangle}$ from $z_{P4}^{\langle4,4\rangle}$ yields positive differences, indicating that every quantile of $z_{P4}^{\langle10,10\rangle}$ should be shifted toward right to match $z_{C4}^{\langle4,4\rangle}$. However, this shift is not a constant for each quantile, revealing that certain strain amplitudes decrease more than the bulk of the distribution does at $C^{\langle10,10\rangle}$. In this case, the upper 3 quantiles suggest that $C^{\langle4,4\rangle}$ imposes a strong outlier effect to the highest 30% of strains. This explains the extreme, 720% peak local lengthening shown for participant C in part D4 for $C^{\langle4,4\rangle}$ (Figure 3.1). Moreover, the overlapped plot of all the shift functions shows that the effect of the tuning parameter alterations can occur in different directions at different muscle parts (Figure 3.1c). Note that a unit change in z-score represents one median absolute deviation change from the median strain of the whole tracked fascicles.

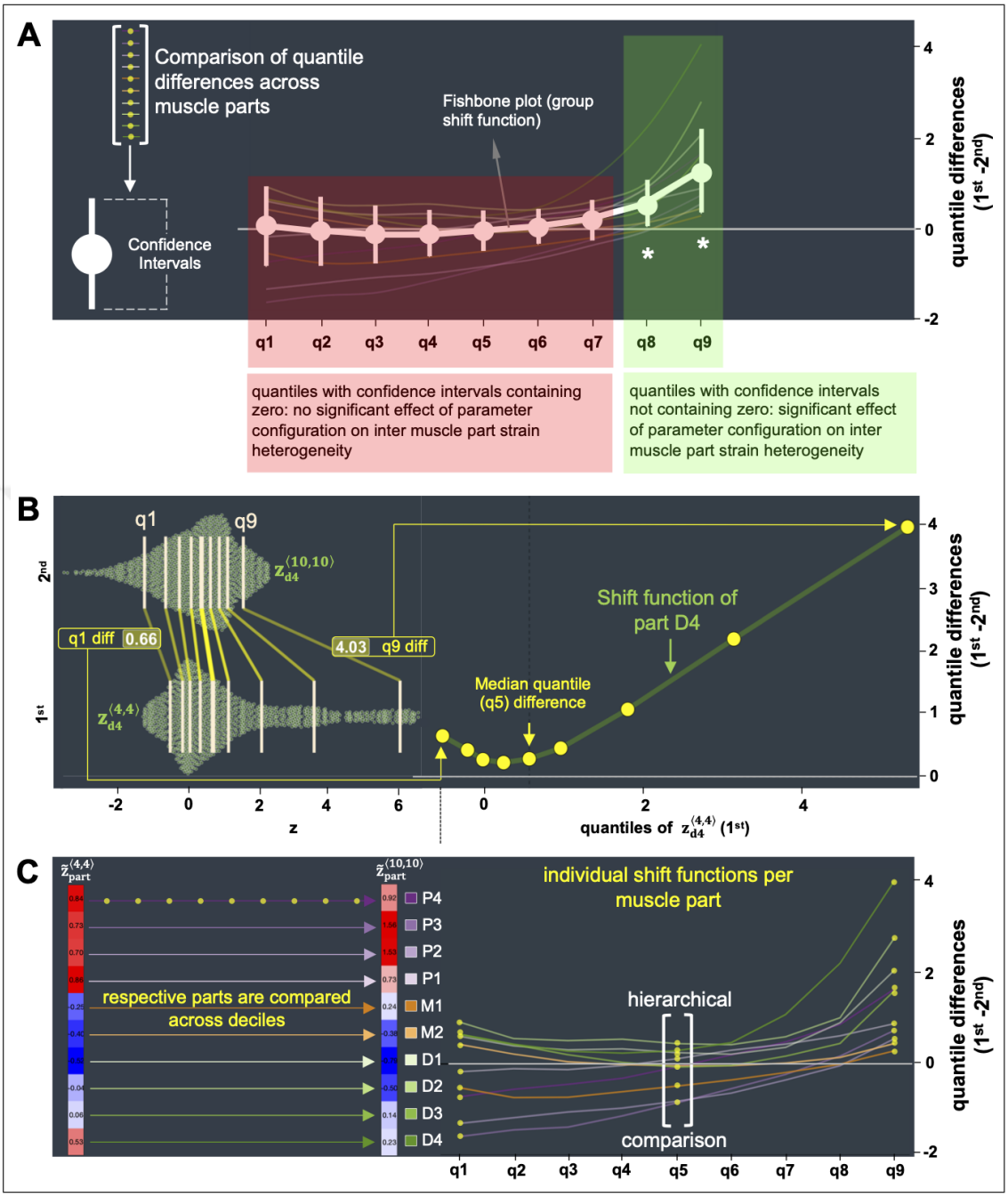

Figure 3.5 Steps of hierarchical shift function (HSF) analysis illustrated for the difference between $C^{\langle 4,4\rangle}$ and $C^{\langle 10,10\rangle}$ in participant C: (a) An individual shift function (SF) of muscle part D4 (right) is constructed based on the quantile differences (yellow circles) in association with the location of compared quantile pairs (beige bars) in $z_{D4}^{\langle 4,4\rangle}$ and $z_{D4}^{\langle 10,10\rangle}$ distributions (green swarmplots). (b) Individual SFs are constructed for each muscle part and overlaid by vertically aligning their quantile differences (right). The quantile difference at q5 approximately equals to the difference between $z_{part}^{\langle 4,4\rangle}$ and $z_{part}^{\langle 10,10\rangle}$ (left) for a given muscle part. (c) Fishbone plot showing muscle part comparisons by white circles at (20% trimmed) means of quantile differences and confidence intervals of the corresponding one-sample t-test.

Figure 3.6 shows this assessment for all participants and $C^{\langle\alpha,\sigma\rangle}$. It is of central importance that the vast majority of fishbone plots do include zero value, indicating overall, the lack of significance of the differences caused by tuning parameter changes on fiber direction strain heterogeneity across muscle parts.

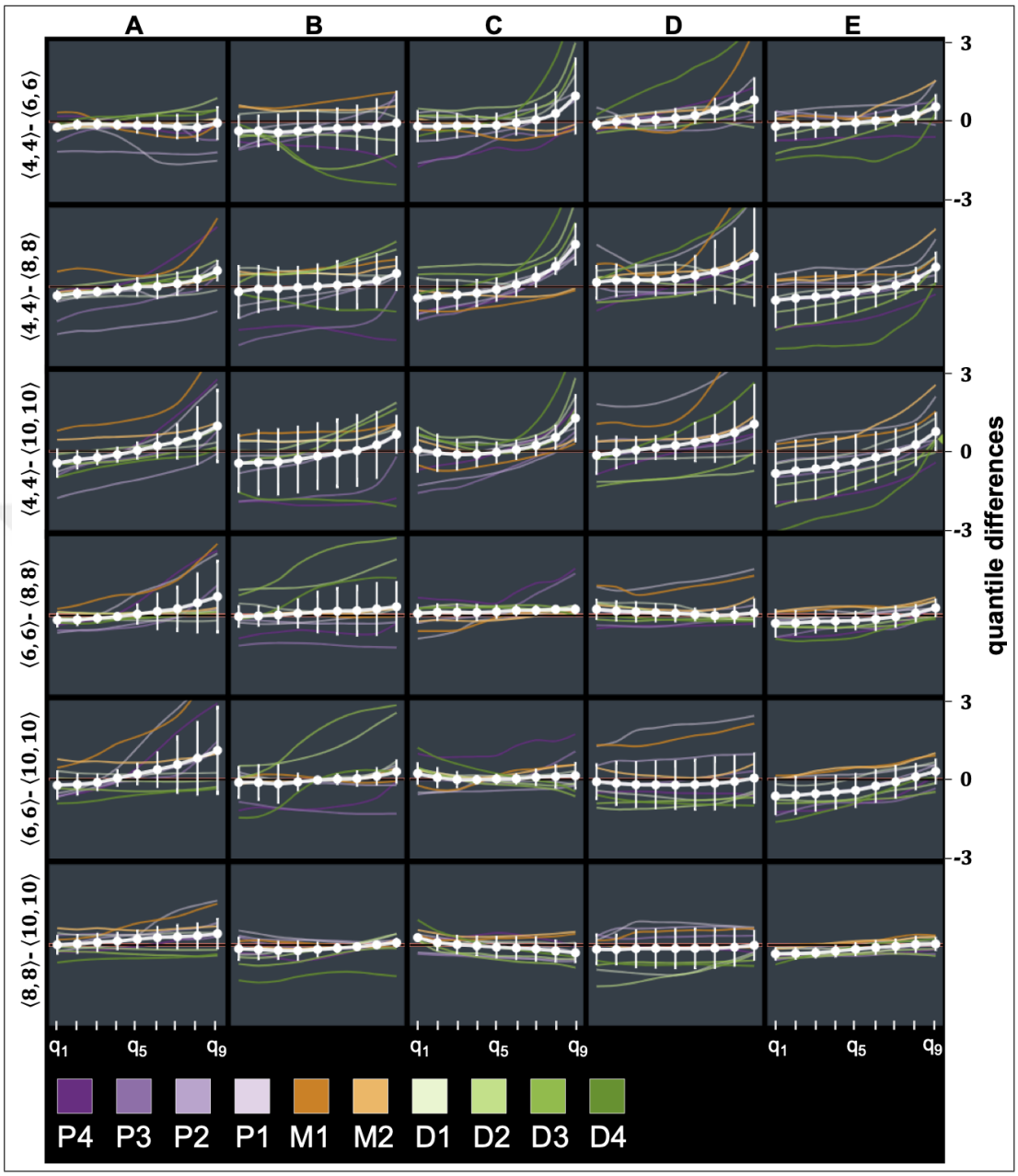

Figure 3.6 Hierarchical shift function (HSF) plots are shown for the differences between the binary pairings of modified z-score distributions where α equals σ (rows) per participant (columns). Panels contain 10 colored shift functions (SF), one for every muscle part. Each SF is plotted by the quantile differences of compared tuning parameter pairs ($z_{1st}^{\alpha=\sigma}$ - $z_{2nd}^{\alpha=\sigma}$) against the quantiles of the first pair ($z_{1st}^{\alpha=\sigma}$). The bold white SF outlines the quantile differences in muscle parts by trimmed means (white markers) and confidence intervals (CI). The y-axis limits are the same (from -3 to 3) to allow easy visual comparison across the panels. Inclusion of the null value of 0 in a CI indicates no significant effect for the respective decile differences.

3.4 Discussion

This study investigated the capability of demons algorithm in quantifying muscle fiber direction local length changes in terms of amplitude and distribution patterns. Based on the technique introduced previously [82] this was done by assessing the effects of implementing a new processing pipeline with the emphasis on effects of changing tuning parameters. A key finding is that the fiber direction strain distribution pattern across different muscle parts maintains overall stability against tuning parameter variations, standing up to rigorous statistical scrutiny. This confirms the hypothesis that demons algorithm tuning parameters are not a significant determinant of fiber direction strain heterogeneity across muscle parts. Given the critical implication of fiber direction local length changes for the understanding of in-vivo muscle function [2], having a detailed understanding of the capabilities of this technique and its limitations will make a major contribution to the proper utilization and further development of it in new studies.

3.4.1 Effects of employing different data analysis workflows

In Pamuk et al. (2016), with both tuning parameters set at 6 ($C^{\langle 6,6 \rangle}$), the general pattern for the deformation field within the GM showed that the proximal tract segments are lengthened, whereas the distal ones are shortened. Despite that general pattern, variations among the participants A-E (the present study follows the same convention) existed. The authors also reported that for some tracts, the general pattern was reversed: e.g., a small portion of the tracts near the medial end of the GM showed shortening proximally and lengthening distally for participant D. Considering $C^{\langle 6,6 \rangle}$ the present deformation patterns mostly mirror the general trend reported by Pamuk et al. (2016). On the other hand, the deformation amplitudes differed between participants with a gradual change from lengthening to shortening in the proximo-distal direction of the GM: peak local strain amplitudes of participants A-E were 10%, 12%, 19%, 17%, 23% for shortening, and 14%, 15%, 117%, 35%, 26% for lengthening, respectively.

Our present findings show that the range of strain amplitudes calculated using the new processing pipeline for $C^{\langle 6,6\rangle}$ (from 15% to 21% for shortening and from 28% to 67% for lengthening) remains within that of Pamuk et al. (2016). Yet, the peak lengthening shown in Participant C does differ (117% vs. 67%). The same applies for Participant A (14% vs. 59%). Nonetheless, $\tilde{\varepsilon}_{P1}^{\langle 6,6\rangle}$ of 14% for Participant A and $\tilde{\varepsilon}_{P4}^{\langle 6,6\rangle}$ of 19% Participant C (Figure 3.2) clearly indicate that bulk of the distributions are in close agreement with the range reported by Pamuk et al. (2016) with outliers excluded (14% for Participant A and 17% for Participant C). This suggest that such discrepancies between the original and present peak $C^{\langle 6,6\rangle}$ values are due to differences in outlier influence (S1). This can be explained by variations in the sampling of strain domain caused by differences between diffusion tractography outputs from different software [195].

These results demonstrate the robustness of methodology by Pamuk et al. (2016) against the application of a new data processing chain, which follows a similar workflow logic, but uses different software packages and programming languages. Supplementing a recent study that established the generalizability of our methodology by acquiring data at a different scanner site and using different analysis tools [196], this study brings demons algorithm one step closer to completing the picture of reproducibility [197] in estimating in-vivo muscle deformation.

3.4.2 General effects of tuning parameters on strain amplitudes

We looked into two kinds of effects. First, is on the strain amplitudes. Regardless of the participants and muscle parts, strain amplitudes profoundly changed in response to changing tuning parameters. As a general effect, local deformation amplitudes declined with increasing parameters in agreement with the theoretical framework [57]. However, this trend was not without exceptions (Figure 3.2). Yet, what muscle parts showing an opposing trend of strain amplitude change against parameter alterations had in common is that the shift functions corresponding to these regions consistently remained outside the HSF confidence intervals. This indicates an amplitude underesti-

mation that persists across the distribution near the anatomical boundaries. Previous tests reported a similar underestimation near anatomical boundaries where discontinuities in deformation field are likely, calling for a more cautious interpretation of strain amplitudes near these regions [57]. The ability of HSF in characterizing such discrepant observations lands the present methodology as a practical tool for the robustness assessment of demons algorithm in strain estimation. Note that recent investigations on the numerical stability of computational pipelines highly encourage such assessments as a typical component of the analytical workflows [198]. Hence, in addition to the synthetic rigid-body transformation tests for setting a minimum detectable change in strain amplitudes [199, 200, 82, 57], applying a parameter analysis as a routine procedure in reporting in-vivo strain amplitudes is a tenable approach for future work.

Although large local muscle tissue deformation is highly plausible [168], representative in-vivo range of strain amplitudes is yet to be established. In the last decade, a considerable body of literature has reported in-vivo strain amplitudes. Nonetheless, a dispersion of values is notable across modalities, even between comparable physiological testing conditions. For example in-vivo strain amplitudes on submaximal muscle activation were reported to be around 7% shortening by 3D ultrasound imaging at 30% of the maximum voluntary contraction (MVC) [201], 25% mean shortening by accelerated 3D dynamic MRI at 30% MVC [55] and 3% proximal mean shortening to 15% mean distal lengthening by 3D high-resolution MRI at 15% MVC [200]. However, several MRI-based 3D quantifications have shown good agreement with in-silico estimations both in strain amplitude [168] and heterogeneity [202]. Despite the promising agreement between model- and MRI-based estimations, optimizing in-vivo data acquisition protocols for accuracy in absence of a ground truth is difficult. Fortunately, a set of evaluation criteria has been documented for image registration quality assessment [203]. Following these guidelines, we used mean squared difference (MSD) as a metric to determine which tuning parameter combination performed relatively better [82, 200]. Recently, we reported MSD values for the $C^{\langle\alpha,\sigma\rangle}$ combinations tested in the present study by repeating the experiment by Pamuk et al. (2016) at a different imaging site [196]. In agreement with Pamuk et al. (2016), $C^{\langle 6,6\rangle}$ minimized the MSD and $C^{\langle 10,10\rangle}$ is indicated as the least favorable selection. Although similarity metrics such as MSD can

be helpful for the tuning parameter adjustment within the confines of a mono-modal registration algorithm, we acknowledge that it is not a direct indicator of the strain amplitude accuracy. Nonetheless, the present findings support that tuning parameters are a significant, yet not the sole, determinant of the strain amplitudes. Given that small alterations in the displacement fields estimated by a non-rigid registration algorithm can lead to higher errors in the metrics derived from it [98], anatomy-mimicking deformable phantoms and reference in-vivo measurements are needed for a thorough accuracy assessment of strain amplitudes.

Second effect assessed was on muscle fiber direction strain distribution patterns. A tuning parameter imposed significant change was observed only for a single participant at a single muscle part, when the edge case $C^{\alpha=\sigma}$ configurations were compared. The HSF analysis showed that $C^{\langle 4,4\rangle}$ consistently introduces a strong outlier effect, whereas the nature of insignificant alterations caused by higher parameters mostly rested on the tested participant and muscle part. In the scope of these findings, it can be concluded that the fiber direction strain heterogeneity is mostly agnostic to the selection of demons algorithm?s tuning parameters and other analytical variabilities brought by different workflow components. This conclusion adds to the previous evidence showing that the primary determinant of the general nature of the deformation field is the tested physiological conditions rather than non-rigid body motion [57], erroneous displacement estimations [57], participant repositioning [60] or random error [82].

3.4.3 Effects of tuning parameters on strain distribution pattern

Tuning parameter induced significant change in muscle fiber direction strain distribution pattern was shown only for one participant and for rather extreme comparisons (Participant C for $C^{\langle 4,4\rangle}$ vs. $C^{\langle 8,8\rangle}$ and $C^{\langle 10,10\rangle}$ restricted to highest strain deciles in distal muscle parts). However, this needs to be addressed. Anatomical localization indicates this effect in the vicinity of aponeuroses. A similar but insignificant effect shown for Participant A and D also sustains the observation near or within the

aponeurotic regions (see supplementary-material).

Although higher displacement amplitudes near aponeuroses are plausible in-vivo [167], the demons algorithm has been shown to produce erroneous results in narrow regions demarking anatomical structures [167]. The present findings indicate that these regions can be sensitive to tuning parameter choice. One solution to mitigate this problem is using a wider Gaussian operator, i.e., a higher σ [129]. However, this hampers registration locality hence calculation of displacement fields between high-resolution images. Given that the nature of the deformation field remains stable against parameter changes when a discontinuity is not a concern, an alternative solution is using a more conservative tractography seeding and fiber bundle filtering approach [204]. This can guard against sampling strain tensors that are subjected to a higher instability, increasing fidelity of the heterogeneity information. Therefore, muscle fiber direction strain heterogeneity across muscle parts is not governed by the choice of demons algorithm tuning parameters, where reconstructed tracts remain within the muscle belly. Due diligence should be exercised when including nodal strain clusters near anatomical boundaries of the targeted muscle to the assessments of strain heterogeneity.

3.4.4 Biomechanical mechanism and implications of muscle fiber direction strain heterogeneity

Existing literature on the quantification of musculoskeletal deformation does not pinpoint a precise range for in-vivo strain amplitudes. Nonetheless, heterogeneous strain distributions are recurrent findings [199, 200, 82, 57] and they bear important information about the underlying mechanical interactions. Therefore, showing the persistence of such key findings against the methodological choices is vital to the reliability of the inferences made about the biomechanics of the muscle. Presently, we demonstrated this for the use of the demons algorithm. The analytical stability of our algorithmic findings has been explained by a sound mechanical analysis. Using the well-established linked fiber-matrix mesh (LFMM) finite element model [61, 15], Pamuk et al. (2020) studied the mechanical mechanism of muscle fiber direction strain heterogeneity [202],

even opposing the imposed global condition, locally at parts of the muscle. The crux of their finding lies in the consideration of skeletal muscle as a mechanical actuator deeply integrated within a load-bearing collagenous lattice, inter-linking (epimuscular connections) a continuum of muscular and non-muscular structures within a limb. Considered in full isolation, the muscle belly should be free from any mechanical load exerted on it, via this network yielding an anticipated uniform strain (e.g., lengthening occurring throughout a globally stretched muscle), which is confirmed using the LFMM model [202]. In contrast, both positive and negative strains manifest in an epimuscularly connected muscle merely by changing its relative position while keeping its length constant. Such position change causes the muscle's epimuscular connections to stretch and impose myofascial loads acting on the muscle, which can manipulate the force balance locally along muscle fascicles giving rise to a non-uniform strain distribution [2]. This mechanism was shown to be effective following imposed passive length change and muscle activation as well [202], which conditions mimicked the principles of those employed in the previous MRI-DTI analyses in human muscle in-vivo [87, 82]. Note that, muscle is motor for movement and sarcomere length change is key to force production. However, heterogeneity of that along muscle fascicle is a key determinant for muscle's length range of force production [35], which has a direct impact on joint range of motion. This is a paramount concept for human muscle function in health and disease, putting in-vivo strain heterogeneity on the map as a potential diagnostic biomarker. Through that, the clinical outcome of several treatments hinges on the mechanical interaction of the muscle with its surroundings e.g., spasticity management using botulinum toxin [205] or orthopedic surgery of cerebral palsy patients [22] as well as kinesio taping [60].

3.5 Conclusion

We have demonstrated the robustness of the MRI-DTI method's outputs to changing software tools, and the consistency of muscle fiber direction strain heterogeneity patterns against parameter selection in demons algorithm. However, the strain amplitudes do vary with parameter choices. Consequently, new studies are indicated to

determine optimal tuning parameters to achieve accurate strain amplitudes compared against known exact strains. The present findings bring us one important step closer to a better understanding of the capabilities and limitations of the MRI-DTI methodology, and inform what conclusions can be reliably drawn about in-vivo musculoskeletal mechanics by using it.

4. VELOCIMETRY AND QUANTITATIVE MRI FOR CROSS-VALIDATION, GENERALIZABILITY AND MICROSTRUCTURAL ORIGIN ASSESSMENT OF FIBER DIRECTION STRAINS AS CALCULATED BY DEMONS NON-RIGID REGISTRATION

4.1 Introduction

Significance of the epimuscular myofascial force transmission [2] in-vivo has been an active research topic. This has driven the development of MRI-DTI approach studying local strains in muscle fiber direction (ε_f) in GM on of passive knee extension [82] and isometric plantar-flexion [87]. In agreement with recent findings from finite element modelling [34], proximal and distal GM fascicle regions undergo differential length changes. In passive muscle, this trend manifests as proximally lengthened and distally shortened fascicle bundles, explained by the effect of distally directed myofascial loads ascribed to the mechanical interaction of the muscle with its surrounding tissues. It is worth noting that this is contrary to the classical viewpoint, which ignores myofascial loads and expects uniform length changes along the fiber length.

Agreement of these in-vivo findings with the theoretical expectations based on the epimuscular myofascial force transmission (EMFT) framework is promising for studying the muscle structure function relationship. Nevertheless, there remained some questions regarding i) the origins of epimuscular mechanical interactions and ii) the validity of the strain distribution patterns as calculated by demons non-rigid registration. For the former, the first chapter of this thesis provides a proof-of-concept on how macroscale anatomical structures visible on a strongly T1-weighted image can be used to associate myofascial loading with the strain distribution pattern, achieved by a manual segmentation of neurovascular tracts. For the latter, a comprehensive set of tests were performed (please see Section 3, including a multiverse analysis [206]

of the demons algorithm tuning parameters in tandem with a robustness assessment [207], presented in the second chapter of this thesis.

A limitation shared by these studies in addressing (i) and (ii) is the lack of orthogonal information for the general purposes of association and validation, respectively. To mitigate this issue, this chapter supplies (i) with quantitative MRI (qMRI) parameters of magnetization transfer and relaxometry for the association between microstructural parameters and strain distribution, and (ii) with VE-PC data acquired in 2D and 4D for cross-modality validation of demons-algorithm-based strain distribution patterns (the *velocimetry experiment*). In addition to addressing the limitation (i), generalizability aspects are also studied by including the demons parameter analysis presented in the Section 3. Hence, this experiment will be referred to as the *generalizability and qMRI experiment*.

The specific objectives of the *generalizability and qMRI experiment* are:

- To analyze the generalizability [207] of the MRI-DTI findings upon passive knee extension by performing data collection at a different site, using a different experimental setup and a different processing pipeline than those used by [82, 87].
- To incorporate quantitative MRI metrics of the longitudinal relaxation time constant (T1) and magnetization transfer ratio and saturation index (MTR and MTsat, respectively), as well as empirical DTI parameter of radial diffusivity (RD) to characterize mechanical load distributions along muscle fibers.

The specific objective of the *velocimetry experiment* is:

- To compare the overall nature of the deformation field calculated by demons algorithm with the strain rate distribution maps produced by velocimetry MRI sequences on submaximal muscle activity.

In the following section, we provide an overview of the recent developments on musculoskeletal qMRI, holding strong potential in opening a new window to the understanding in-vivo muscle structure function relationship. For a brief review of the recent developments in the musculoskeletal velocimetry imaging methods that set the benchmark for the evaluation of in-vivo tissue mechanics, the reader is referred to Section 1.2.?

4.1.1 Supplementing in-vivo mechanical analyses with qMRI

Conventional MR images portray the underlying anatomical structures through a complex contrast mechanism that includes contributions from tissue magnetic relaxation properties (i.e., T1 and T2), proton density (PD), diffusion, magnetization transfer (MT) and susceptibility effects. These effects emerge from a series of quantum-mechanical interactions of the magnetic and radiofrequency fields with the targeted soft tissue, both of which are systematically manipulated by the acquisition systems to adjust relative contributions of effective micrometer-level MRI parameters (i.e., T1, T2, PD, MT, and diffusion coefficient (D)). As a result, the conventional images convey a predominant contrast (e.g., T1-weighted, or diffusion-weighted) in co-dependency with the remaining effective parameters. These images are often represented in an arbitrary grayscale range (i.e., voxel brightness), as they are qualitative in nature. To extract meaningful information from conventional images, pattern recognition strategies must be employed, either by expert radiologists or computer vision methods. It should be noted that the morphological metrics derived from these images (e.g., tumor volume) attributes a score to the observations based on, again, a qualitative pattern recognition (e.g., detection of the tumor). As MRI is not a direct measurement of the structure [208], such derived metrics are subjected to variabilities coming from multiple origins including image acquisition, reconstruction, and processing.

Quantitative MRI (qMRI), on the other hand, aims at assigning each voxel with a quantity that is defined on a physiologically meaningful measurement scale. Going from weighted images to quantitative maps, extracting information takes a more objec-

tive form as the voxel values now carry a more specific information about the underlying tissue microstructure. Therefore, quantitative maps are expected to be more reliable across imaging centers and time points besides providing added diagnostic value. Quantitative maps are generated by fitting the experimental data (that has been acquired by altering acquisition parameters) to an MRI signal representation or to a biophysical model [209]. The following sections will look at different musculoskeletal qMRI applications under 3 categories of relaxometry, diffusion and magnetization transfer imaging.

4.1.1.1 Relaxometry imaging. Of all musculoskeletal quantitative imaging methods, relaxometry-based measures have the longest research history. With its first application dating back to 1965, activation-dependent and edema related increase of the transverse relaxation time constant (T2) [210] has found widespread research in exercise [211] and pathological cases such as inflammation, fat-infiltration, fibrosis and atrophy [212]. Such changes observed on a monoexponential fitting regime were mostly ascribed to a bulk change in the myowater content. On the other hand, several studies have shown that the transverse relaxation in muscle decays over at least three components [213]. It is commonly accepted that the shortest component (T2 $<$ 10ms) is associated with the macromolecule-bound hydrogen [214]. More recently, Araujo et al. (2014) reported that myowater from intracellular and interstitial (i.e., extracellular space found outside the blood) compartments give rise to the intermediate exponential component (T2 around 30ms), whereas the longest exponential component (T2 $>$ 100ms) comes from the vascular space [215]. Quantifying T2 with multicompartmental accuracy enables the decoupling of the origins of cellular-level changes. For example, Saab et al. (2010) demonstrate that all three exponential components show increase after exercise, but changes of the shortest and intermediate components outweigh the longest one [216]. Another study looked at the effects of creatine supplementation on multicompartment T2, and reported that only the shorter components showed an increase, suggesting an increase in the intracellular water [217]. Theoratically, these multiexponential models of muscle tissue relaxation can be used to study tissue oxygenation as blood signal can be isolated from the actual myowater content. Nevertheless

in practice, these acquisitions are not time efficient. To characterize microcirculation of skeletal muscles, a faster approach is the use of blood oxygenation level dependency (BOLD) of the MRI signal [218]. Recent evidence points out that the primary source of BOLD changes in the muscle comes from perfusion related alterations [219]. The BOLD in muscle have been shown to differentiate slow- and fast-twitch fiber composition [220], varying levels of MVC [221] and drug intake [220]. So far, the investigation of BOLD changes in muscle have provided an easy mean to evaluate the muscle function in the context of microcirculatory regulations. Nevertheless, the quantitative contributions of multiple factors that determine the musculoskeletal BOLD effect are yet to be understood [218].

On the other hand, T1 mapping in skeletal muscle can help bring specificty to distinguish certain diseases that T2 alone cannot, such as inflammation vs fat infiltration [222, 223]. It is also possible to evaluate denervation [224] , post-exercise and age related changes [225]. Another popular use of T1 mapping is the assessment of changes in collagen content, such as fibrosis. For example, Bull et al. (2013) have reported a strong correlation between T1 and the degree of diffuse myocardial fibrosis using histological validation [226]. Nevertheless, the systematic bias between either fast cardiac [227] or traditional T1 mapping methods [228] imposes an important reliability problem. To that end, using vendor-neutral implementations of relaxometry mapping methods plays an important role in increasing multi-center and longitudinal reliability [229]. Widespread adoption of such standardization strategies can improve the detection of true biological variability that is associated with in-vivo T1 variations observed in skeletal muscle.

4.1.1.2 Diffusion imaging. As summarized in Section 1.3.2, empirical DTI parameters (e.g., FA, ADC and RD) have been applied in the cytoarchitectural characterization of muscles over the last 3 decades. More recent musculoskeletal diffusion imaging literature offers a deeper focus on the quantification of more specific surrogate markers of microstructural properties such as fiber diameter and extracellular water fraction [78]. Berry et al. (2018) reported that 40% of the variation in myofiber size can

be accounted by the simple single-echo DTI indices such as FA, which is increased to 70% when multi-echo DTI is performed in expense of long acquisition times. The main advantage brought by multi-echo DTI to muscle diffusion imaging is the possibility of sampling diffusion for longer durations (i.e., longer diffusion time) without significant SNR penalty due to short T2. Time-dependent diffusion MRI, also known as qt imaging [230] aims at characterizing tissue microstructure by allowing water molecules to interact with structural barriers (e.g., sarcolemma, macromolecules, cytoskeleton etc.) for varying diffusion times (i.e., the t space) in addition to multiple b-values (i.e., the q space) that alone cannot describe the diffusion it is Gaussian in all compartments. The development in this field has primarily focused on the study of white matter microstructural properties in the human brain. Unfortunately, most of these models cannot be applied to the myofibers as they show high density packing, larger cell sizes and short T2 times [231]. Nevertheless, some studies have explored such transient diffusion effects in the skeletal muscle [232, 233, 234]. Using random permeable barrier model, Fieremans et al. (2017) have shown the feasibility of diffusion imaging in quantifying fiber size and sarcolemma permeability, and demonstrated its application in calf muscles after exercise (increased myofiber size in GM) and in post-operative rotator cuff atrophy (decreased myofiber size) [233]. With the same model, Lemberskit at al. (2021) have shown that fiber size, sarcolemma permeability and fiber orientation distribution can be regarded as muscle microstructural features, and they can capture physiological changes that the anatomical measures (e.g., cross-sectional area) and empiricial DTI indices (e.g., FA, MD) could not [234]. Finally, a sensitivity analysis on the muscle miscrostructural parameters of fiber diameter, volume fraction, permeability, intra- and extracellular diffusion coefficients and T2 times have revealed that intracellular diffusion dominates the measured signal and fiber diameter appears to be more influential than permeability [231]. Even though most of these measurements are deemed reasonable in experimental musculoskeletal applications, numerical simulations put in the question their accuracy [235].

4.1.1.3 Magnetization transfer imaging. Magnetization transfer (MT) contrast makes use of the nuclear spin interactions between hydrogen protons in different

macromolecular environments. These interactions have been explained by commonly used two-pool model [236]. Conventional MRI images are reconstructed from the signals received from protons that are not bound to macromolecules, constituting the free pool. On the other hand, protons in close vicinity of macromolecules has almost no contribution to those conventional images, representing the bound pool. It is possible to selectively excite these spins using specially designed off-resonance radiofrequency (RF) pulses, known as magnetization transfer pulses. Skeletal muscle has been shown to exhibit a prominent MT effect upon the application of these pulses [237]. The spatially varying magnitude of this effect is commonly represented by calculating magnetization transfer ratio (MTR) as follows:

$$MTR = \frac{MT_{off} - MT_{on}}{MT_{off}} \tag{4.1}$$

where MToff is the magnitude of tissue signal before the MT pulse and MTon is the signal after pulse has been applied. This measure have so far been used in skeletal muscle to grade clinical severity of peripheral neuropathy [238], to evaluate pathological changes in limb-girdle muscular dystrophy patients [239] and to investigate its correlation with muscle strength [240]. Although one of its earliest uses on skeletal muscle was performed in a quite low magnetic field (0.26T), authors claimed that change in MTR values is attributable to the post-exercise increase in extracellular water content [241]. However, MTR is denoted as a semiquantitative measurement, given that overall observed signal in a quantitative MR experiment has been determined by a more complex model that includes the contributions of T1, uniformity of of B1 (excitation) and B0 (static) field amplitudes. As T1 depends on iron and calcium concentration, the relationship between the MTR and macromolecular content becomes non-linear.

In an attempt to explore qMT effects in skeletal muscle by decoupling quantification from tissue relaxometry parameters and scanner hardware, Sinclair et al. (2010) have designed the first rigorous qMT experiment on lower leg muscles of healthy sub-

jects [242]. They acquired a full set of FLASH images with 7 distinct off-resonance offset frequencies and two nominal flip angle to fit a complex qMT model [243] to their data. This enabled fitting of 4 different parameters that has shown intersubject variability. Then, by combining their parameters with T1 maps, they calculated bound proton fraction F, which defines the ratio of which MR-visible protons reside in the macromolecules. This parameter has been shown to be the clinically most relevant measure to evaluate central nervous system pathologies [244]. However, quantification of F requires a time consuming full qMT data acquisition and necessary sequence modifications to alter offset frequency are not enabled in most of the scanners. A recent study have shown that this parameter has shown a marked non-linear association with MTR, whereas displaying a high linear correlation (r = 0.80) with MR saturation index (MTsat), which reduces the effect of T1 from MTR [244]. Although MTsat is also a semi-quantitative measure, it greatly reduces some fundamental problems associated with MTR (i.e., T1 and B1 contributions), yielding an easy to acquire and a meaningful parameter [245]. Recently, Romero et al. (2019) have reported significantly higher MTsat values in the lower leg muscles of male participants in comparison to females [246]. They also report that MTsat values are consistently higher in Tibialis Anterior (TA) than those in the remaining calf muscles. These sex-related and regional differences can be explained by gender specific cytoarchitectural arrangement and Type I/Type II fraction of muscle fibers altering the MT saturation through extracellular occupancy of macromolecular content. The study of MT effects in skeletal muscle within clinically feasible scan time and with higher specificty to macromolecular content warrants further research with more advanced techniques such as inhomogeneous MT with zero echo time readouts [247].

4.2 Methods

4.2.1 Data acquisition

A 29 years old healthy female subject (173cm, 67.3kg) volunteered for the generalizability and qMRI experiment. Written informed consent was acquired prior to

the data collection following a protocol approved by the Montreal Clinical Research Institute Ethical Review Board, University of Montreal, Montreal, Quebec, Canada. The dataset including a single participant for the velocimetry experiment was kindly provided and presented herein with the permissions by Drs. Usha Sinha and Shantanu Sinha, Department of Physics, San Diego University, San Diego, California, USA.

For the generalizability and qMRI experiment, the participant was placed ate a 3T scanner (Siemens Prisma, Erlangen, GE, equipped with an upgraded 80 mT/m gradient system) in prone position. The left leg was brought to a reference position: (I) the ankle was ?xed at 90 by using stripes and cushioning materials. To locate the knee joint, a piece of Velcro was attached over the patella and on the MRI table. Few degrees of knee flexion were imposed by elevating the torso with support. The restriction was due to fact that utilization of the 15-channel knee coil without removing the spine coil precluded raising subject?s trunk to impose a higher level of flexion. After positioning subject into the isocenter, one anatomical turboFLASH and two field maps (B1 and B0) were acquired using the pulse sequences and acquisition parameters presented in Table 4.1-4.2. Subsequently, the support was removed and the knee was brought to full extension. In this deformed state (II), separate sets of anatomical turboFLASH, diffusion ss-EPI, field map (B1 and B0), magnetization transfer contrast and three variable flip angle (VFA) 3D image sets were acquired (Figure 4.1).

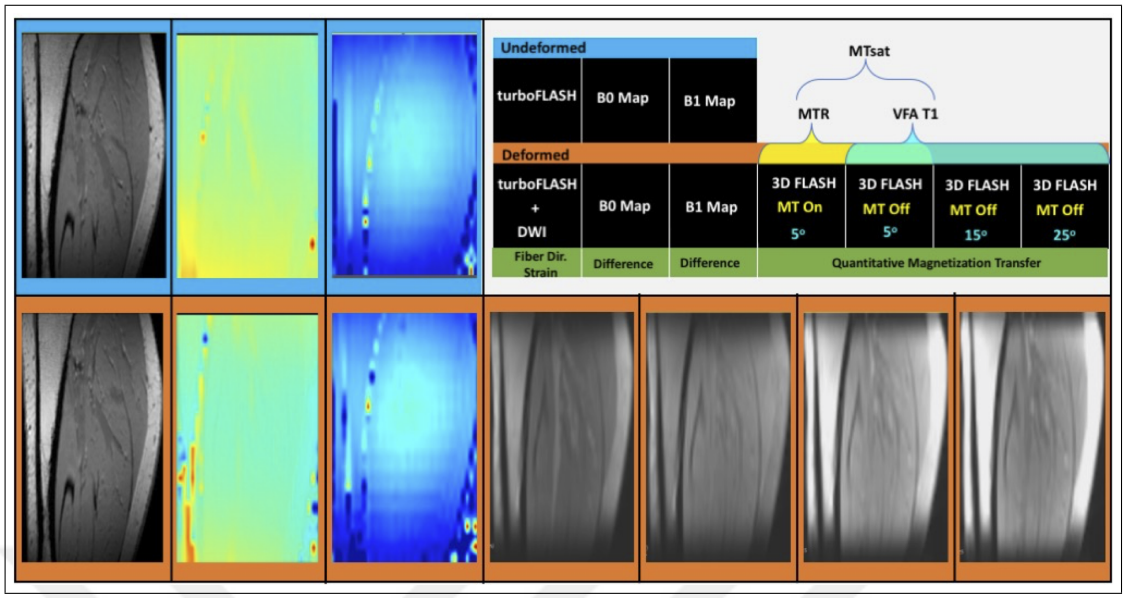

Figure 4.1 Sagittal plane images from 3D volumes acquired using different sequences and by altering specific parameters for the qMRI experiement. Inset figure (upper right) shows the relation between input/output data and respective information for each image by their placement on the layout.

Table 4.1
Acquisition parameters for the generalizability and qMRI experiment including structural and difusion-weighted sequences.

Sequence Name	**3D fast low-angle shot (FLASH)**
Slice Orientation	Transversal
Repetition Time (TR) (ms)	35
Echo Time (TE) (ms)	2.36
Pixel Size (mm2)	1.5 X 1.5
Slice thickness (mm)	5.0
Phase enc. dir	A >>P
Flip Angle	a: 5 b: 5 c: 5 d: 15 e: 25
Magnetization Transfer Contrast (MTC)	a: off b: on c: off d: off e: off
Bandwidth (Hz/pix)	260
MT Pulse Offset (Hz)	1200
Sequence Name	**ss-EPI**
Slice Orientation	Transversal
Repetition Time (TR) (ms)	2900
Echo Time (TE) (ms)	67
Pixel Size (mm2)	1.5 X 1.5
Slice thickness (mm)	5.0
Phase enc. dir	P >>A
Acceleration mode	GRAPPA (2 Accel. Fact., 24 Ref. lines)
Number of diffusion directions	20
b-Values	0, 500
Averages for b-values	5, 1
Bandwidth (Hz/Pixel)	1184

Table 4.2
Acquisition parameters for the generalizability and qMRI experiment including field mapping.

Sequence Name	**gre_field_mapping (b0 field map)**
Slice Orientation	Transversal
Repetition Time (TR) (ms)	1000
Echo Time (TE) (ms)	a: 4.92 b: 7.38
Pixel Size (mm2)	3 X 3
Slice thickness (mm)	5.0
Phase enc. dir	A >>P
Flip Angle	90
Bandwidth (Hz/Pixel)	259
Sequence Name	**b1 mapping (product sequence)**
Slice Orientation	Transversal
Repetition Time (TR) (ms)	6830
Echo Time (TE) (ms)	1.97
Pixel Size (mm2)	3.1 X 3.1
Slice thickness (mm)	5.0
Phase enc. dir	A >>P
Flip Angle	8
Bandwidth (Hz/Pixel)	490
Echo Spacing (ms)	4.3

For the velocimetry experiment, the participant was placed at a 1.5T clinical scanner (GE Healthcare, WI) in supine position with the right foot attached to a custom-made pedal as in [248]. The dataset for demons-algorithm-based strain quantification (relaxed and 15% MVC, undeformed and deformed, respectively) was acquired following the procedure described in [87]. The scan plane was prescribed in oblique-sagittal orientation to align GM fascicles within plane. To enable cross-modality comparison (Figure 4.2), the same participant was then scanned using a velocity-encoded phase-contrast (VE-PC) sequence during (approximately 70) repetitive cycles of iso-

metric plantarflexion at 15% MVC with the acquisition parameters summarized in Table 4.3.

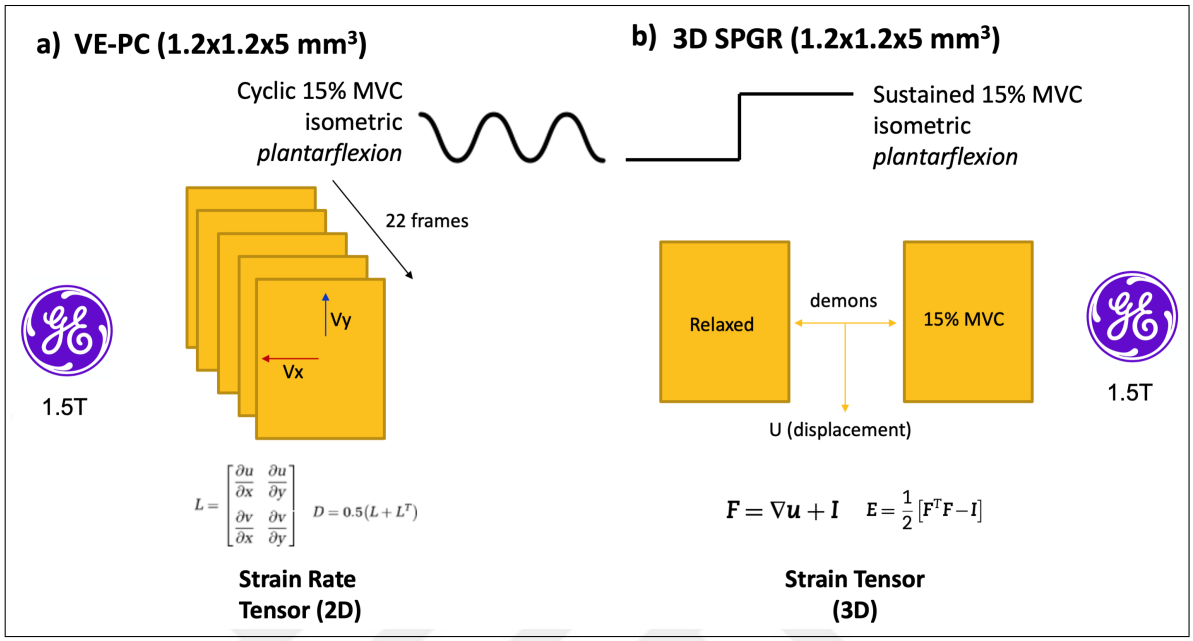

Figure 4.2 Schematic illustration of the data structure acquired for the cross-modality validation of the demons-generated-strain distribution. a) Velocity-encoded phase-contrast (VE-PC) data acquired during repetitive 15% MVC isometric plantarflexion. b) Undeformed (relaxed) and deformed (15% MVC sustained isometric plantarflexion) high-resolution anatomical datasets acquired using 3D spoiled gradient-echo (SPGR) sequence.

Table 4.3
Acquisition parameters for the 2D VE-PC sequence.

Sequence Name	**2D velocity-encoded phase-contrast (VE-PC)**
Slice Orientation	Sagittal-oblique
Repetition Time (TR) (ms)	16.4
Echo Time (TE) (ms)	7.7
Voxel Size (mm2)	1.2 X 1.2
Slice thickness (mm)	5.0
Field of View (cm)	30 X 22.5 (75% partial phase)
Image Matrix	256 X 192
Number of slices/phases	1/22
Velocity encoding ($cm \cdot s^{-1}$)	10
Number of excitations	2

Table 4.4
Acquisition parameters for the 4D compressed-sensing (CS) PC sequence.

Sequence Name	**4D CS flow**
Slice Orientation	3D
Repetition Time (TR) (ms)	51.2
Echo Time (TE) (ms)	4.43
Flip Angle (FA) (°)	80
Voxel Size (mm2)	2 X 2
Slice thickness (mm)	5.0
Field of View (cm)	15 X 30
Image Matrix	66 X 160
Number of phases	50
Velocity encoding ($cm \cdot s^{-1}$)	15
CS acceleration factor	8

4.2.2 Data processing

For both experiments, the calculation of the deformation field between deformed and undeformed anatomical images was performed using the demons implementation by Kroon et al. (2009), as in the reference implementation [82]. However, tractography and the projection of scalars along tracked GM fascicles were implemented in a new processing pipeline for the *generalizability and qMRI experiment*:

- Diffusion weighted images (DWI) were converted into a common data format for DTI processing using 3D Slicer.
- For the quality control and pre-processing of the diffusion data, DTIPrep was used [249]. Quality control included the removal of the bad gradients (none were discarded out of 30 directions for this dataset) and visual inspection for the prominent artifacts. Next, the joint Rician filtering method was used for denoising DWI. This was followed by motion correction of the gradient images and removal of the eddy current artifacts to improve the fidelity of the data [250].
- Preprocessed data was then transferred to the MITK-diffusion toolbox (v2018-4.0) for the calculation of DTI and fiber tractography [251]. The default streamline tractography algorithm was performed with the same tracking parameters chosen for GM by Pamuk et al. (2016). However, tracts were seeded only within the manually prescribed GM with the preferential streamline integration direction from deep to superficial aponeurosis. Resultant fiber bundle was filtered to discard streamlines that are not representative of the expected GM fascicle orientation.
- Deformation field calculated by demons algorithm and the reconstructed tracts were then transferred to an in-house toolbox to calculate voxelwise strain tensors and to project them on streamline nodes to represent fiber direction strains along tracked fascicles. Alignment of the fiber bundle with the deformation field was manually checked by overlaying them on the anatomical volume yielded by demons registration.

- Quantitative maps of MTR, (transmit B1 field corrected) MTsat and T1 were calculated using qMRLab (v2.2.1) [252], following a between-series motion correction implemented in the Elastix toolbox (v3.9) ref [253]. Empirical diffusion metric of RD was derived from the tensor image calculated using MITK-diffusion [251]. All the quantitative parameters were than projected onto the nodal fiber coordinates as scalars for visualization and statiscial analyses.

For the calculation of 2D strain tensors from the VE-PC data to enable cross-modality validation in the *velocimetry experiment*, the workflow described in [248] was followed. Positive and negative eigenvalues were derived from the strain rate data to be compared with first and third principle demons-calculated-strains (Figure 4.2).

To provide a more leveled ground for the comparison against demon-based strains, a 4D compressed sensing (CS) accelerated data derivatives (strain rate maps and descriptive statistics of strains) were kindly provided by Drs. Usha and Shantanu Sinha's research group. For reference studies please see [55, 56]. The original acquisition was performed at an CS factor of 7, yielding 50 temporal phases at 15% MVC muscle activity during 3 seconds (see Table 4.4 for the protocol). To derive demons-based strains, magnitude images of the 10th and 30th frames were registered. Unlike the 2D VE-PC analysis described above, here, the source of actual deformation captured by the demons (2 magnitude images out of 50 frames) is on par with that of 4D CS PC (50 velocity encoded images), allowing a more accurate comparison.

4.3 Results

4.3.1 Generalizability and qMRI experiment

The new diffusion imaging protocol and the new tractography pipeline have improved GM fiber coverage notably (Figure 4.3). The streamlines were representative of the GM fiber architecture, originating from deep aponeurosis, running in superoposte-

rior direction and attaching into deep aponeurosis.

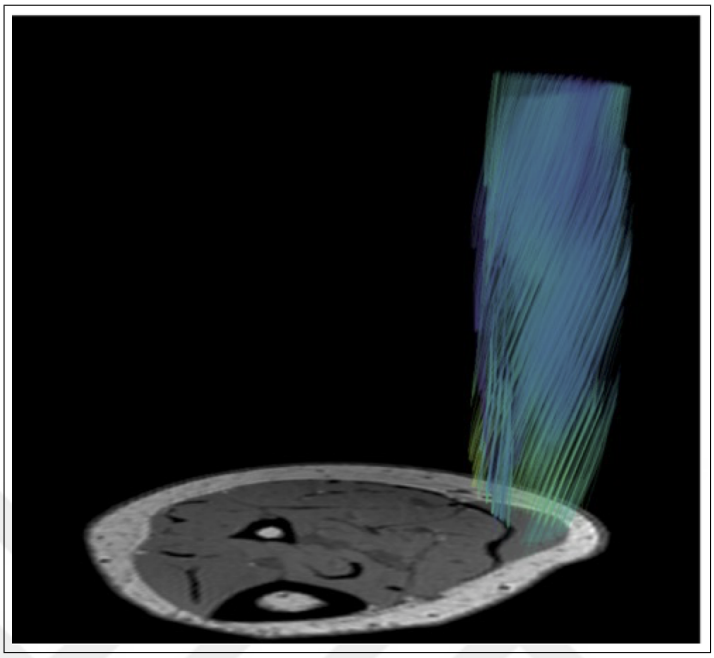

Figure 4.3 Medial gastrocnemius (GM) muscle fibers reconstructed using new acquisition parameters and tractography pipeline. Densely packed streamlines are representative of the muscle structure and present across the longitudinal coverage of the FOV of diffusion weighted volume. Tracts were transparently colored at random to provide a better sense of orientation.

Locations of the higher and lower nodal strain clusters remained stable irrespective of the parameter combinations (Figure 4.4). In line with the expectations from the theoretical framework of the demons algorithm, higher sigma values yielded a smoother distribution. For example, in the first row, smallest sigma gives out a focal distribution pattern, which smoothens with increasing sigma values. The extents of the distribution magnitudes, on the other hand, decreases markedly from 104% to 6% and from 47% to 12% for lengthening and shortening respectively. Similar relationship can be observed in all the rows. When observed in a column-major order, distributions reveal that the changes in strain magnitudes due to alpha were much smaller than those due to sigma. These trends can also be observed from the violin plots (see supplementary Figure C.1).

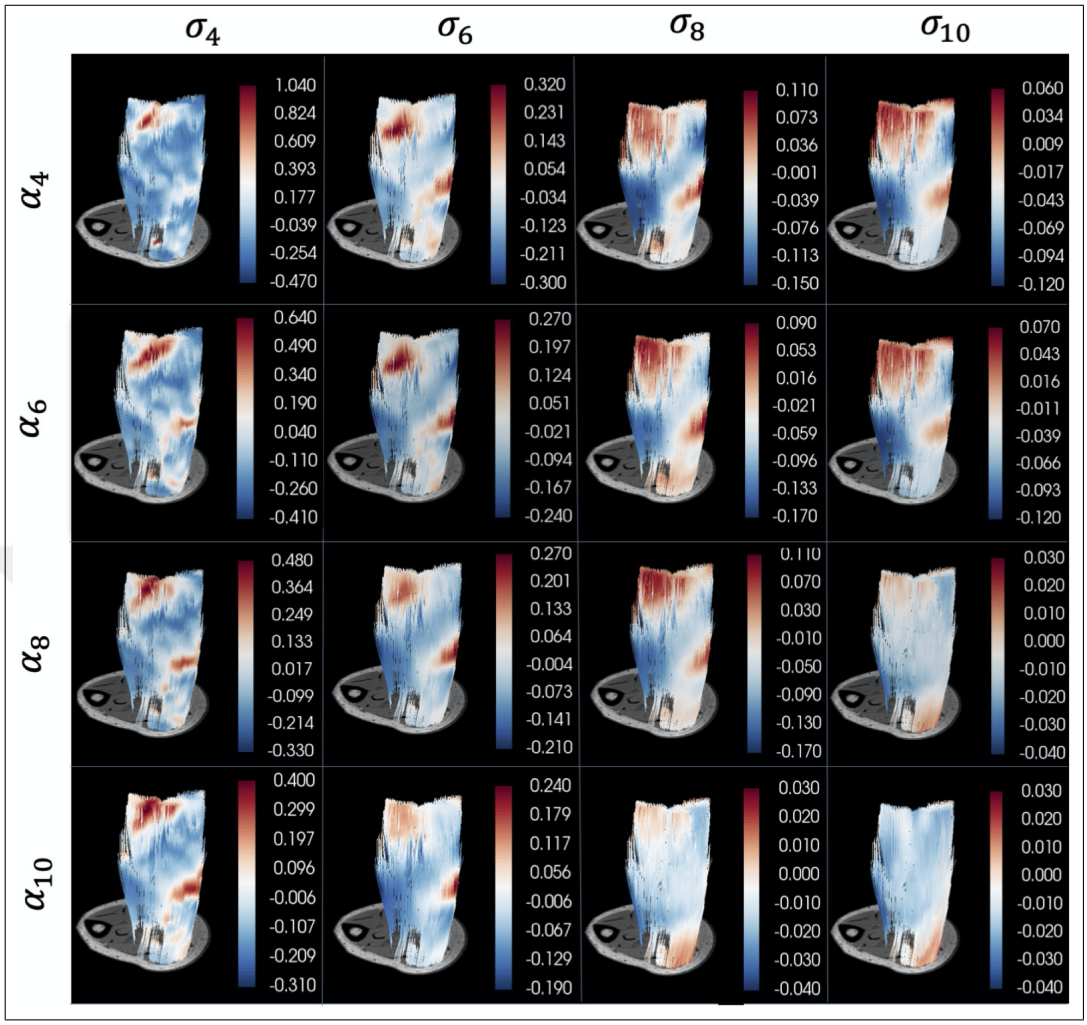

Figure 4.4 Serial fiber direction strains are visualized on the tracked fascicles of the medial gastrocnemius (GM) muscle for paired alpha (rows) and sigma (columns) combinations.

When the algorithm parameters kept the same with the methodology applied by Pamuk et al. (2016), the ε_f distribution ranged from -24.0% to 27%. This range is comparable to that of given over five subjects (-23% to 35%). Moreover, the overall nature of the distribution (Figure 4.4) is retained, indicating that proximal portion of the tracked fascicles lengthened, whereas shortened distally.

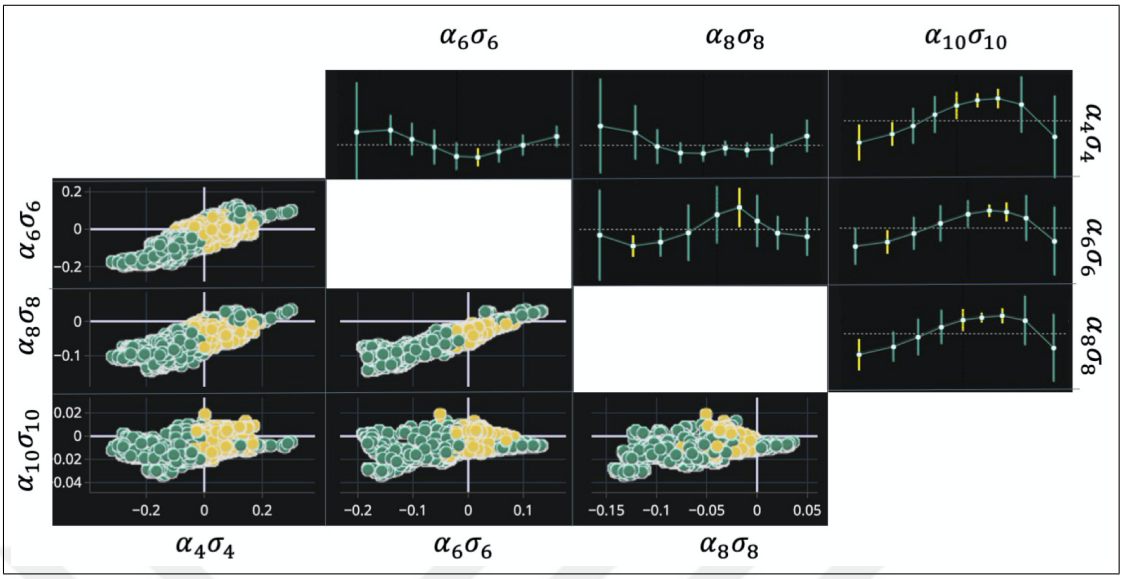

Figure 4.5 Lower triangle: Scatter plots for the paired alpha-sigma combinations ($C^{\langle\alpha,\sigma\rangle}| \ \forall_{\alpha=\sigma} \in \{4, 6, 8, 10\}$) of mean fiber direction strains ($\bar{\varepsilon_f}$). Pairs underwent at least one sign swap among these pairs are shown by yellow markers, green otherwise. Upper triangle: Shift function plots for the same alpha-sigma combinations are given in the lower triangle. These plots show 9 markers to represent intervals from 10 deciles. Horizontal axis gives the first pair, whereas vertical axis represents differences between the deciles of pairs. Vertical lines crossing each marker represent confidence intervals (CI) of the respective decile. Inclusion of zero (horizontal dashed line) indicates that the compared deciles are not significantly different (green). Significantly different deciles are indicated by yellow vertical line. Note that distributions are z-score normalized. Therefore 5th marker from the beginning corresponds to the mean decile. Remaining markers to its right and left represent strain deciles above and below the mean decile.

Except from $C^{\langle 10,10\rangle}$, the relationship between $\bar{\varepsilon_f}$ of different parameter combinations showed a marked linearity (Figure 4.5). This implies that the bias imposed in response to the parameter changes can be partially removed by shifting and scaling. However, 34% of the tracked fascicles (yellow markers in Figure 4.5) swapped sign at least once for the parameter combinations where $C^{\alpha=\sigma}$. Nonetheless, these changes were clustered around the zero crossing. Therefore, the changes do not have a preferential effect on the direction of strains, but strain amplitudes near zero crossing are more prone to changes in algorithm parameters. It should be acknowledged that such comparative analyses are not conclusive of which parameters performs better in the lack of ground-truth. Therefore, to supplement this analysis with an objective selection basis, registration performances were compared by mean squared error (Figure 4.6).

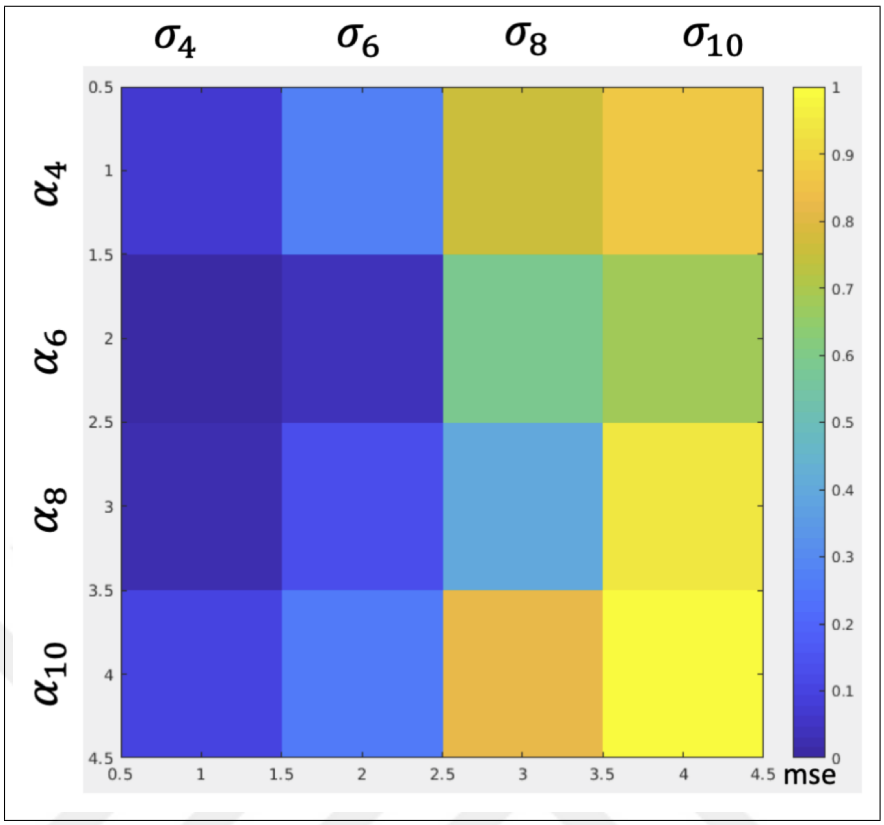

Figure 4.6 Heatmap of the normalized mean squared errors calculated between the registered (transformed undeformed state) image and the deformed state image for all parameter combinations.

Figure 4.6 shows that the error is the highest for $C^{\langle 10,10 \rangle}$. This can be explained by the reduction in the performance of demons algorithm to resolve local shape changes. For the lower σ values, keeping $C^{\alpha=\sigma}$appears desirable. The parameter combination applied by Pamuk et al. (2016), which is $C^{\langle 6,6 \rangle}$, yields one of the lowest error value for the same conditions tested in the present study.

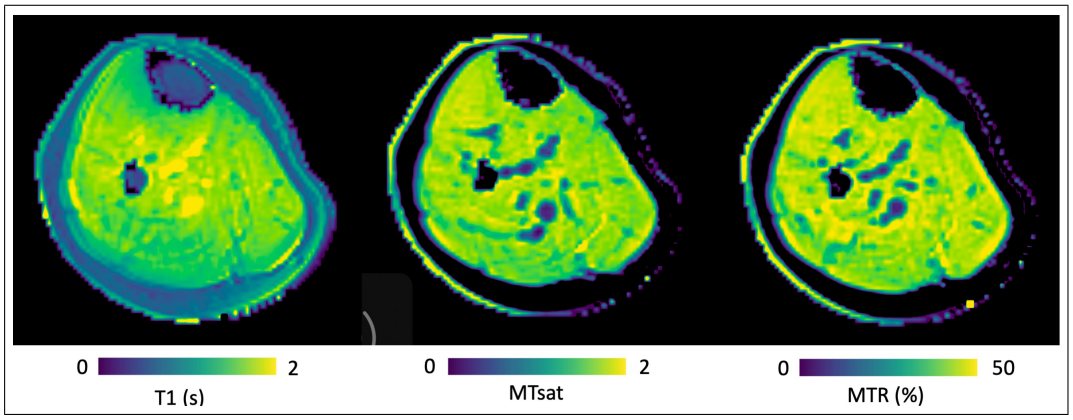

Figure 4.7 An axial slice of the quantitative T1, MTR and MTsat maps.

Table 4.5
Descriptive statistics (mean±SD) for the quantitative MRI parameters (T1, MTsat and MTR) are given for lower leg muscles of gastrocnemius medialis and lateralis (GM, GL), soleus (SOL), tibialis anterior (TA) and peroneus (PER).

	GM	GL	SOL	TA	PER
T1	1.67±0.09	1.50±0.06	1.66±0.07	1.50±0.04	1.75±0.05
MTsat	2.09±0.12	1.90±0.12	2.06±0.14	2.16±0.06	2.13±0.07
MTR	43.8±0.75	41.2±1.07	45.3±1.66	44±1.30	44.7±1.2

Figure 4.7 shows a transverse view of the quantitative maps of T1, MTsat and MTR within their respective distribution ranges. Within-plane, MTsat and MTR distributions do not show a notable regional variation, unlike the T1 map that shows higher values near vascular structures. Descriptive statistics from the ROI analysis (see supplementary Figure C.2) confirms the similar distribution range for T1 (from 1.5 to 1.75 seconds), MTsat (from 1.9 to 2.16) and MTR(from 41.2 to 45.3%) for all lower leg muscles in the analyzed slice (Table 4.5).

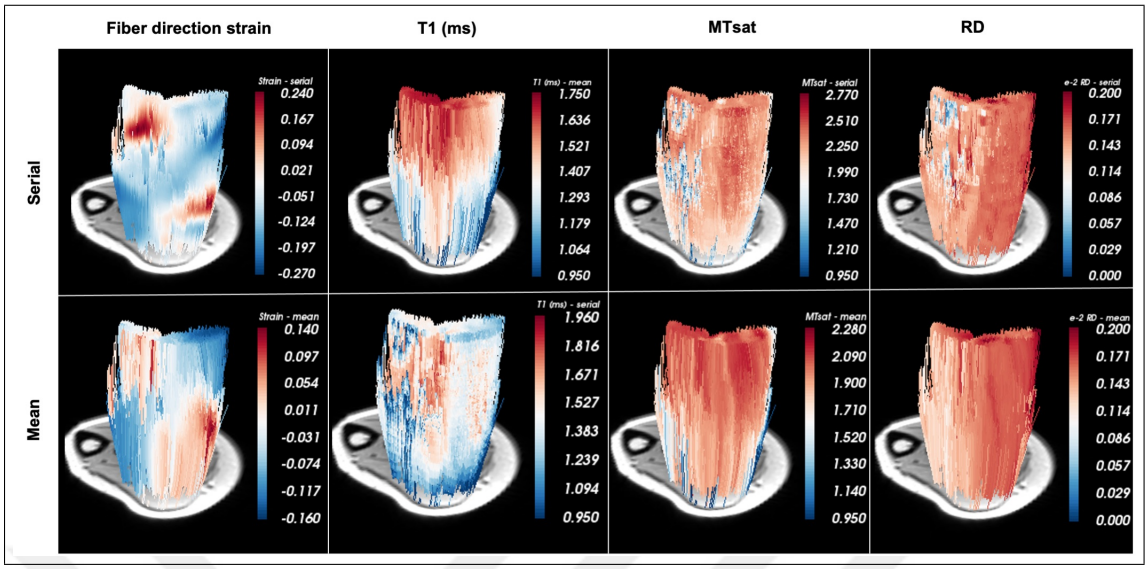

Figure 4.8 Serial and mean distributions of fiber direction strains (obtained at $C^{\langle 6,6 \rangle}$), T1, magnetization transfer saturation index (MTsat) and radial diffusivity (RD).

When filtered by the tracked fascicles, MTsat in GM varied from 0.9 to 2.7, T1 from 0.95 to 1.75 seconds and RD from 0.01 to 0.2 (Figure 4.8). Serial T1 distribution showed a somewhat compartmentalized appearance, with longer values in the proximal half and a significant effect on the $\bar{\varepsilon_f}$, $\bar{\varepsilon_{f+}}$, $\bar{\varepsilon_{f-}}$ (Table 4.6).

Table 4.6
Standardized beta coefficients (β) and standard errors (SE) from the multiple linear analysis to test the predictive effect of the quantitative MRI parameters over the mean fiber direction lengthening ($\bar{\varepsilon_{f+}}$) and shortening ($\bar{\varepsilon_{f-}}$).

	$\beta - \bar{\varepsilon_f}$	$SE - \bar{\varepsilon_f}$	$\beta - \bar{\varepsilon_{f+}}$	$SE - \bar{\varepsilon_{f+}}$	$\beta - \bar{\varepsilon_{f-}}$	$SE - \bar{\varepsilon_{f-}}$
MTsat	0.021	0.018	0.08	0.020	0.095	0.080
T1*	-0.30	0.020	-0.18	0.229	-0.26	0.079
RD	0.036	0.018	-0.06	0.212	-0.04	0.047

4.3.2 Velocimetry experiment

Following the convention by Sinha et al. (2015), Figures 4.9 and 4.9 show negative and positive eigenvalues of the 2D strain rate tensor. The eigenvalues are sorted according to the positive and negative values at each voxel, not by magnitudes. Therefore, the labels of negative and positive strain rate in Figures 4.10 and 4.9 may become misnomer depending on the deformation trend at a given time point, respectively. Please see Appendix C.2 for more detailed definitions and mathematical descriptions.

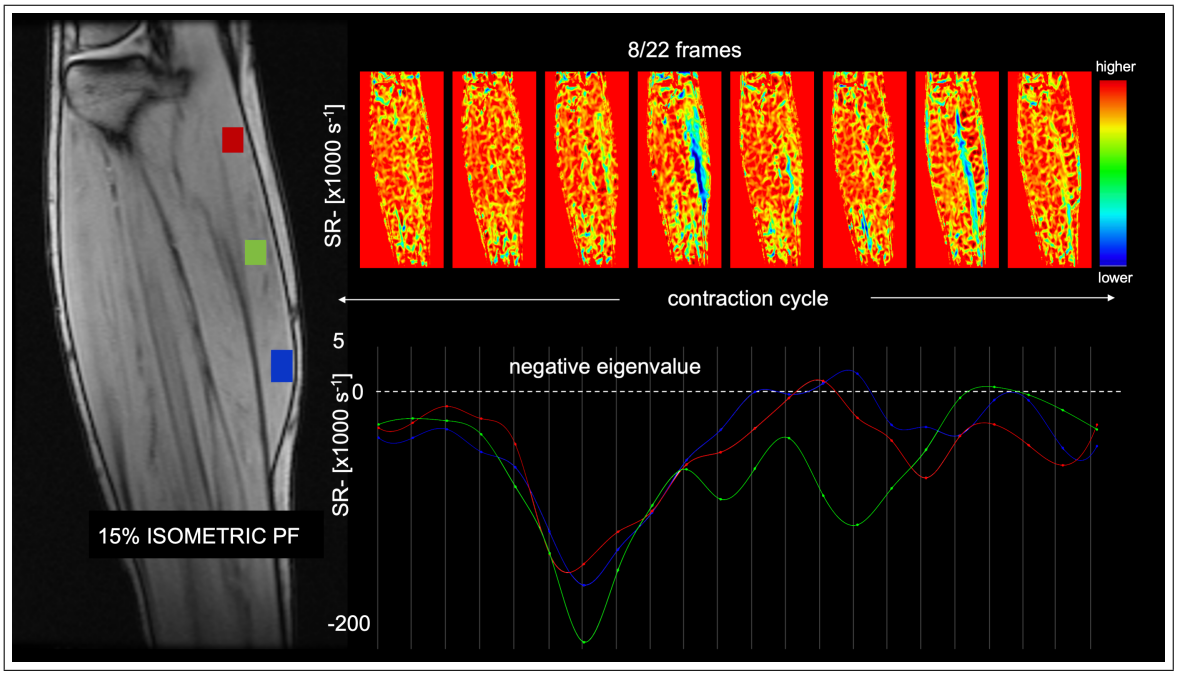

Figure 4.9 Positive eigenvalues of the strain rate tensor plotted throughout the contraction cycle (22 frames) at the proximal (red), medial (green) and distal (blue) regions of the medial gastrocnemius. Negative eigenvalues (SR_{fiber}) upon plantarflexion are shown (top row) for 8 out of 22 frames, corresponding to the contraction phase (approximately from 3th to the 10th frame).

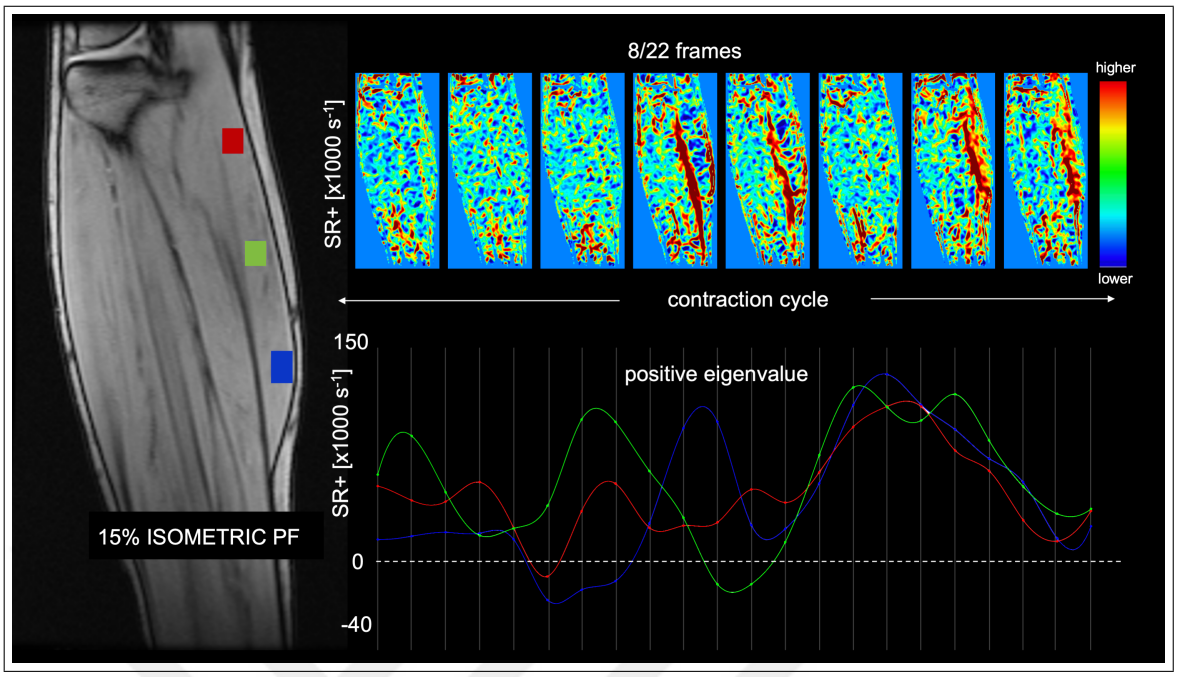

Figure 4.10 Positive eigenvalues of the strain rate tensor plotted throughout the imaging cycle (22 frames) at the proximal (red), medial (green) and distal (blue) regions of the medial gastrocnemius. Positive eigenvalues ($SR_{in-plane}$) upon plantarflexion are shown (top row) for 8 out of 22 frames, corresponding to the contraction phase (approximately from 3th to the 10th frame).

During the 15% MVC plantarflexion phase of the imaging cyle (from 3th to 10th frame in Figure 4.9), a prominent SR_{fiber} peak is obsered in all three GM regions (proximal, medial and distal given by red, green and blue ROIs, respectively). However, the SR_{fiber} was the highest at the medial, followed by the distal and proximal parts, indicating a heteregeneous strain trend across the GM. The 4th frame displayed in Figure 4.9 indicate higher contraction amplitudes around the deep aponeurosis with a noticeable gradual decrease towards the superficial aponeurosis of the GM. The proximo-distal heterogeneity persists during the rest of the imaging cycle.

Positive eigenvalues, i.e., $SR_{in-plane}$ or cross-fiber SR, during the same phase of the imaging cycle show a more pronounced proximo-distal heterogeneity (Figure 4.10). An interesting observation is that at the 5th time frame, where SR_{fiber} starts peaking (Figure 4.9), all ROIs indicate nearly identical $SR_{in-plane}$. Whereas at the peak of the contraction, proximo-distal heterogeneity of $SR_{in-plane}$ maximizes, such that proximal

and distal parts show positive and negative SR values, respectively. The highest shear strain trend remains at the medial part, where the highest contraction magnitudes were observed. On the other hand, the 4th frame in Figure 4.10 reveal that high $SR_{in-plane}$ magnitudes are clustered around the aponeuroses, but less within the muscle belly, unlike the SR_{fiber} where a gradual distribution pattern exists.

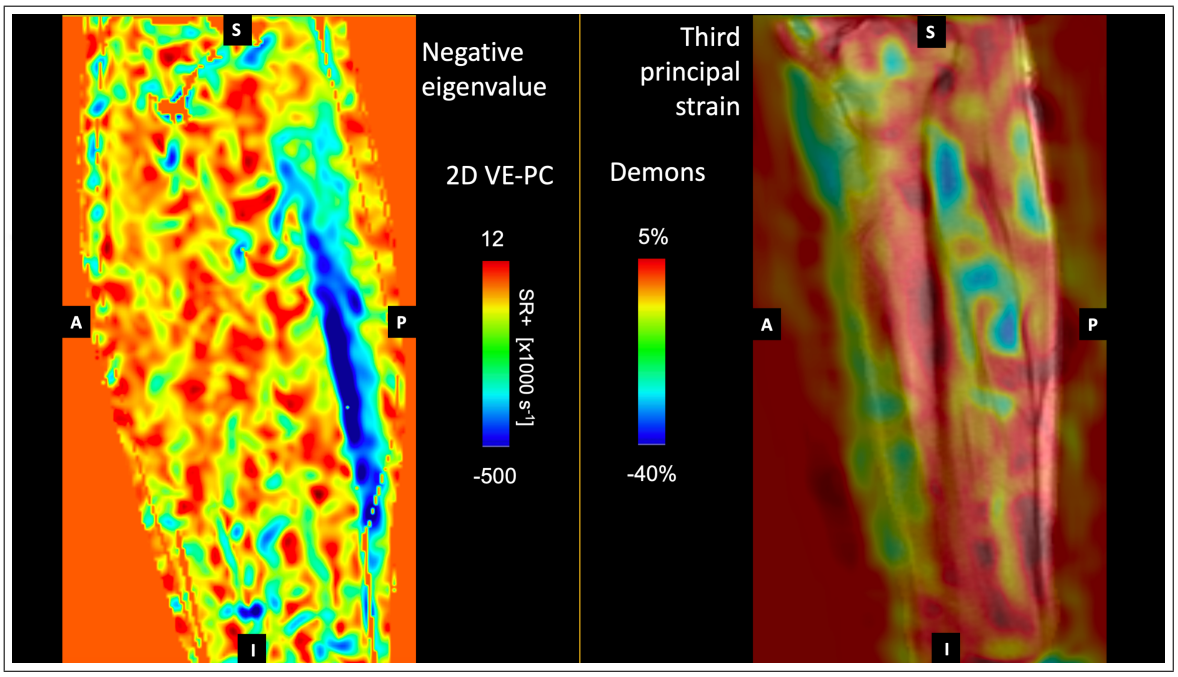

Figure 4.11 Side-by-side comparison of (left) the negative eigenvalue map of the SR (SR_{fiber}) from 2D VE-PC (the peak plantarflexion phase of cyclic 15% isometric contraction) and (right) third principal strains calculated from the non-rigid demons registration of 3D SPGR images (relaxed vs on sustained 15% isometric plantarflexion). Note that the slice location of the demons-based strain map (right) was set manually to mimic that of VE-PC.

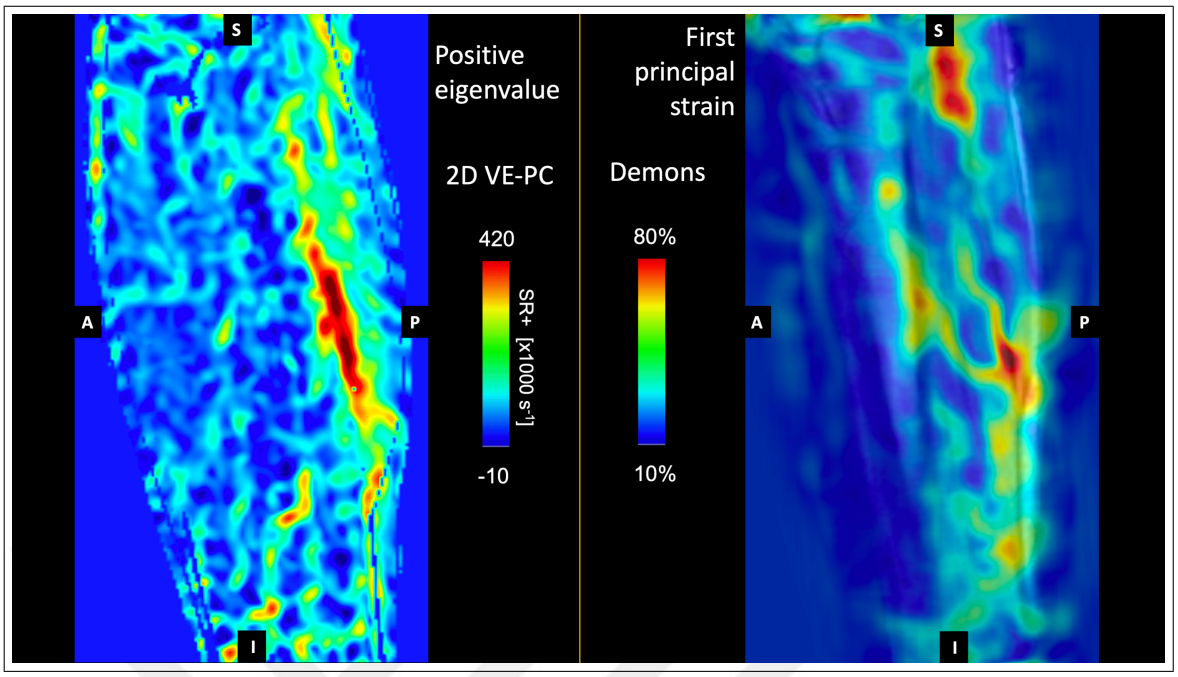

Figure 4.12 Side-by-side comparison of (left) the positive eigenvalue map of the SR ($SR_{in-plane}$) from 2D VE-PC (the peak plantarflexion phase of cyclic 15% isometric contraction) and (right) first principal strains calculated from the non-rigid demons registration of 3D SPGR images (relaxed vs on sustained 15% isometric plantarflexion). Note that the slice location of the demons-based strain map (right) was set manually to mimic that of VE-PC.

Side-by-side comparison of the SR_{fiber} and demons-based third principal strains (Figure 4.11) does not show an immidiately obvious similarity between the distribution patterns. However, both maps indicate shortening at GM and SOL with higher amplitudes in vicinity of deep aponeurosis. Differently from SR_{fiber}, demons-based third principal strains indicate local lengthenings of small magnitude. Both $SR_{in-plane}$ and demons-based first principal strains (Figure 4.12) show high amplitude strains towards the distal parts of the GM-SOL compartment, again, with higher deformations localized near the muscle boundaries.

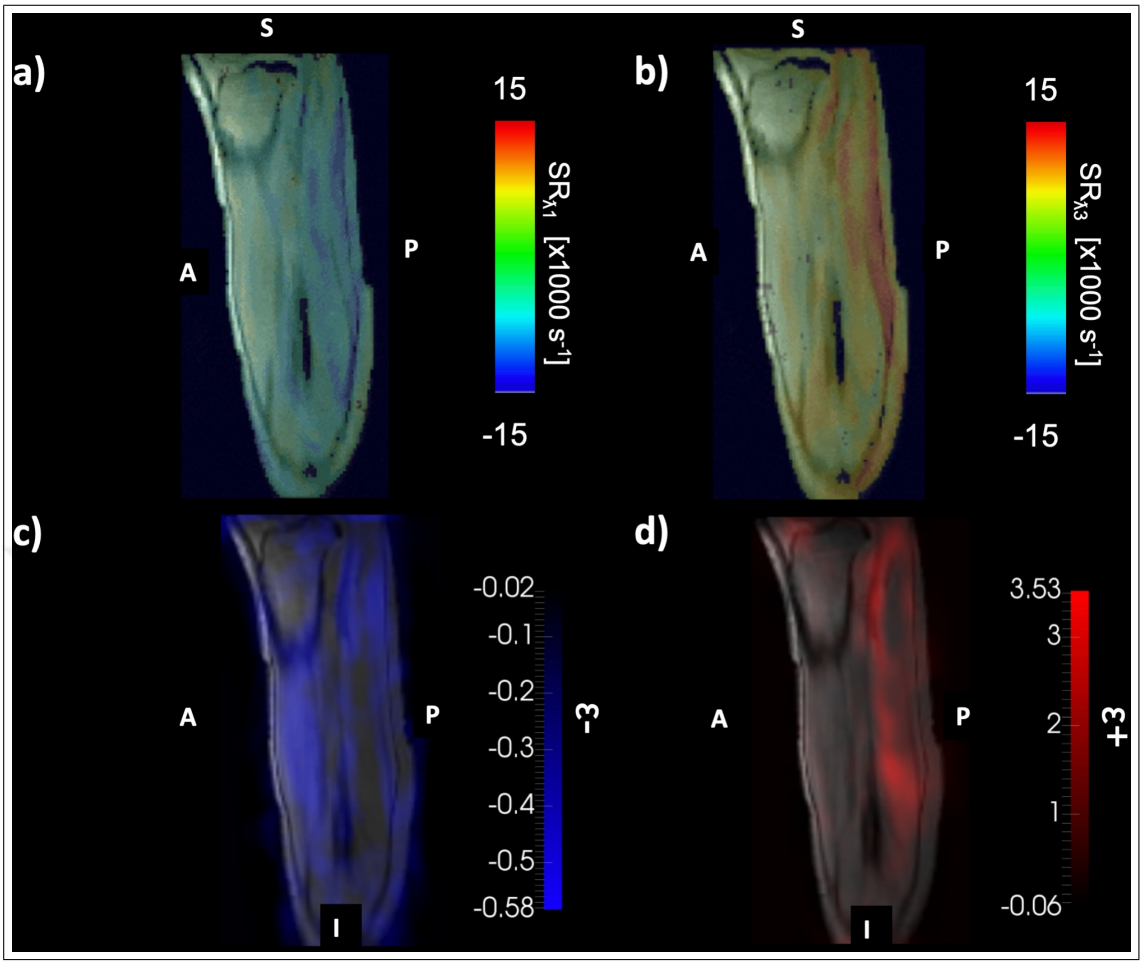

Figure 4.13 Comparison of deformation patterns between highly accelerated 4D compressed sensing (CS) flow acquisition and demons-based strains. a) Negative eigenvalue map of the SR (SR_{fiber}) and b) Negative eigenvalue map ($SR_{in-plane}$) from 4D CS PC. c) Third and d) first principal strains from demons-based strain quantification.

Comparison of demons-based strains and 4D CS PC strain rate maps show a more noticeable similarity (Figure 4.13): high amplitude deformations localized GM and around the deep SOL, with smaller magnitudes between both regions. Please note that it is possible to derive strain maps in addition to strain rate maps from the 4D CS PC data, as the voxels can be tracked within the whole 3D volume across time frames [56]. Even though the images were not available for a side-by-side comparison, strains from 4D CS PC (for a 7X7 ROI placed at the GM) were in the range of 30% shortening ($E_{\lambda 1}$) and 20% lengthening ($E_{\lambda 3}$) during the peak of the contraction. Demons-based (between 10th and 30th frame, where the peak of the contraction occurs) principal shortening and lengthening for GM was 43% and 25%, respectively.

4.4 Discussion

4.4.1 Generalizability and qMRI experiment

In this study, the passive knee extension experiment by Pamuk et al. (2016) was reproduced using a different scanner, with different participant and using a new processing pipeline. Both strain distribution pattern and magnitudes are generalizable given the agreement with the trends observed across five participants in [82]. Coupled with the robustness analysis presented in Chapter 2, the reproducibility analysis in [87] and participant repositioning in [60], these findings complete the puzzle of experimental reliability for the MRI-DTI method [207].

Although tractography seeding was restricted to the GM boundaries described by manually drawn ROI, some streamlines followed a pathway unrepresentative of GM structure (perpendicular streamlines at the distal end starting from the deep aponeurosis). Nonetheless, these streamlines can be discarded using a better ROI, orientation based filtering offered by MITK-diffusion and filtering by quantitative T1, as a threshold can be set for non-muscular voxels. More importantly, the coverage of the tracked fascicles in the present study exceeds that of given by [82]. This is in part due to the improvement of the GM tract selection, but also because of enhanced fidelity of the diffusion acquisition at twice higher gradient strengths. Therefore, there is not a reference in [82] for the region residing below the central section of the fascicles (Figure 4.4) to compare against. This region typically shows lengthening for the studied subject, highlighting the importance of a wider FOV in characterizing length changes, as addressed in the following section.

Scatter plots in Figure 4.5 adds to the shift function analysis presented in Chapter 2 for chracterizing the robustness of the demons-based strain quantification against tuning parameters. Other than those paired with $C^{\langle 10,10\rangle}$, fiber direction strain distributions between $C^{\alpha=\sigma}$pairs show a strong linear trend, indicating the applicability of the transformation revealed by the shift function in calibrating strain distributions in presence of a ground truth measurement. In addition, the strain magnitudes that

underwent sign changes were clustered around zero crossing. This indicates that the sign swap did not take place between high-magnitude strain regions (e.g., not from a high amplitude shortening to high amplitude lengthening). This further suggests that the bias introduced by parameter changes can be normalized by shifting and scaling.

T1 carries fundamental yet intricate information about biophysical microenvironment. Its distribution is informative of the variations in local tissue composition. Hence, the significant linearity shown in Table 4.6 implies a covariance with a tissue mechanical property that is linked to certain microstructural information captured by T1. Serial T1 distribution (Figure 4.8) exhibit a compartmentalized appearance, with longer values in the proximal half (e.g., 1.75s), with a notable decrease towards the distal ends (e.g., 0.9s). Assuming collagen, this would imply an increase in stifness going from proximal to distal parts of the tracked fascicles, which agrees with the myofascial load distribution leading to the observed strain pattern. Nevertheless, such a direct association is not possible as T1 depends on a multitude of factors. MT, on the other hand, is expected to be more specific. In skeletal muscle, the fraction of bound pool protons is plausibly associated with collagenous components, intra- and extracellular myocellular lipids or other tissue components that contain macromolecular content [242]. The degree of which these tissue components contribute to the MT effect is not known yet [238], granting further investigation on the sensitivity of the qMT methods on macromolecular content changes in skeletal muscle. A good example to that respect would be comparing the qMT parameters of botulinim-toxin (BTX) injected muscle with that of a control group to investigate whether qMT metrics account for collagenous content. This is because, recent histological findings indicate that the percentage of intramuscular connective tissue is higher in BTX administered animals than those for control groups [22]. Another plausible method is approaching MT effects in the context of the EMFT phenomena under passive joint angle movement. For example, findings from our study have shown that passive knee extension imposes distally directed myofascial loads on the tracked fascicles, resulting a general distribution pattern among all subjects with considerable intersubject variability (Pamuk et al. 2016). If MTsat accounts for the collagenous content primarily, such variabilities in strain distribution is expected to be correlated with magnetization saturation index

distribution. Finally, it is worth noting that determination of myofascial load distribution is a complex multiparametric problem. Therefore, strain quantification model can highly benefit from incorporation of quantitative metrics including MRI visible anatomical force transmission components, diffusion properties and MRI-related fields maps along with qMT data.

In conclusion, musculoskeletal qMRI characterization is a promising venue to an improved understanding of human muscle function relationship in the context of myofascial force transmission. Further research with more participants, multiple imaging sites and histological validation is needed to clarify the relationship between the quantitative parameters and muscle tissue microstructure.

4.4.2 Velocimetry experiment

Our research group rigorously tested various aspects of demons algoritm in quantification of material strain in skeletal muscle (see Section 1.4). The second chapter of the present thesis adds to these the findings that the deformation pattern is not determined by algorithmic choices. Here, we present the first cross-modality MRI dataset for a validity assessment using 2D VE-PC, as well as highly accelerated 4D CS flow.

Non-uniform deformation is a common finding in both 2D VE-PC and demons-based strain distributions, as well as higher strain amplitudes in the vicinity of deep aponeuroses of the studied triceps surae muscles. Nevertheless, a notable similarity is not present between the compared maps (Figures4.12 and 4.12). This can be explained by:

- Muscle deformation is not imposed similarly during cyclic (2D VE-PC) and sustained (demons) isometric submaximal plantarflexion.
- The resolution of the 3D SPGR deformed/underformed image pair (1.2x1.2x5 mm) is not on par with the reference study (1mm isometric) [87]. In addition,

the 3D SPGR sequence used for the data collection, unlike the turboFLASH flash used in [87], was not inversion-prepared, leading to a less effective T1 weighting. Demons algorithm is intensity based, hence affected by image contrast differences and resolution to track displacement.

- Resolving displacement in 2D vs 3D has important implications. In 2D VE-PC case, image orientation is prescribed to align with fiber orientation, under the assumption that the displacement in the orthogonal direction does not contribute to the deformation, as shown by [248, 55]. However, given the complex 3D architecture of muscle fibers [49, 81], such plane prescription does not neccesarily lock the orthogonal direction perpendicular to entire muscle fibers.
- Fundamental differences between Eularian and Lagrangian descriptions of flow. Please see Appendix C2.1 for a more theoretical explanation on the difference between VE-PC strain rates and demons-based strains.

Fortunately, highly accelerated 4D CS PC can change the landscape of validity analysis for in-vivo muscle deformation as quantified by non-rigid registration algorithms. As it is possible to track individual voxels across the contraction phase, a 3D displacement field can be obtained to calculate Green-Lagrange strain tensor as described in Chapter 1.3.1. Moreover, both magnitude images on which demons algorithm operates and velocity-encoded images capture the identical morphological changes. This, for the first time, levels the ground for PC-based strains to be rendered as a validation dataset for demons algorithm upon in-vivo deformation.

Figure 4.13 show the preliminary findings for such comparison. Overall spatial distribution patterns in SR and demons-based strain maps show similarity. Even though the reference for amplitude comparison was limited to a 7x7 ROI place at the center of GM on 4D PC strain maps, demons-based (at $C^{\langle 6,6 \rangle}$) principal shortening and lengthening (43% and 25%, respectively) are within 15% error margin with those from 4D PC (30% and 20% respectively). This difference is in part due to the selection of reference frames for demons registration. Unlike the 30th frame corresponding to the peak of the contraction, which shows good image contrast, magnitude reconstructions

of the first 10 frames were not suitable for registration. The difference between the reference frame selection for the calculation of Lagrangian strain is a plausible explanation of the amplitude differences. Finally, image contrast characteristics and resolution of the 4D flow magnitude images are much less informative for the demons algorithm to track deformation (see Figure 4.14 for comparison), resulting in a strain map with a coarser appearance (Figure 4.13).

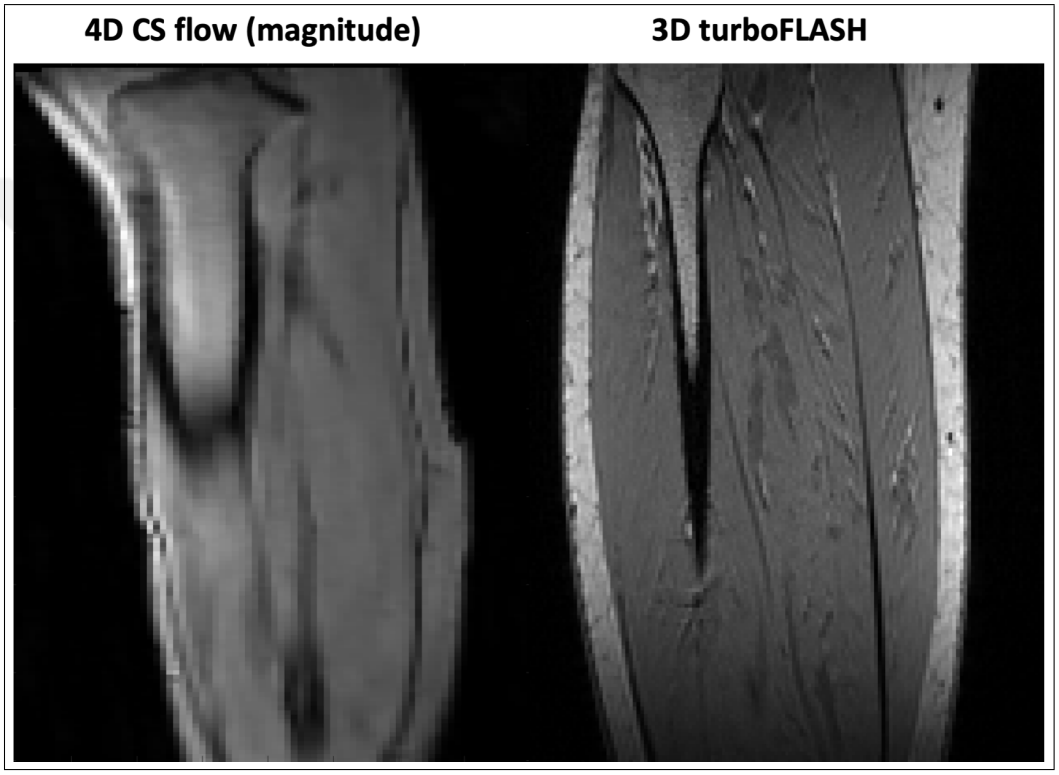

Figure 4.14 Comparison of 4D compressed sensing (CS) flow magnitude reconstructed image (left, 2x2x5mm) and turboFLASH T1w high-resolution (right, 1mm iso) images.

Future studies focusing on the cross-modality validation of image registration-based strains against highly accelerated CS flow acquisitions can be optimized for higher resolution and better image contrast. Given that such advanced acquisition and reconstruction methods are available to a limited number of research sites, validating MRI-DTI method with reference to high-dimensional CS data has a pivotal role for the accesibility and cost-efficiency in studying human muscle function relationship. As the current analysis is performed within the bounds of the data made available, Figure 4.13 constitues a preliminary, yet a promising, finding.

In conclusion, MRI-DTI method is robust against algorithmic choices, in addition to be repeatable, reproducible and generalizable [207]. Quantitative MRI can complement in-vivo mechanical analyses with tissue microstructural information to study human muscle function relationship across multiple dimensions, in-vivo. Finally, accelerating MRI using techiques such as CS and fingerprinting goes a long way toward validating the capacity of simpler acquisition and processing methods in providing reliable analyses. Our preliminary findings (Figure 4.13) represent a good example in that direction.

5. GENERAL DISCUSSION

Different information layers acquired by and extracted from multimodal MRI acquisitions bring a new dimension into studying human muscle function relationship in the context of myofascial connectivity, as well as to the validation of such in-vivo approaches. This thesis demonstrates a powerful example by incorporating macro- (NVT) and micro-scale (qMRI) structural information to the analysis of in-vivo mechanical interactions (demons-based strains) between lower leg muscles under both active and passive conditions.

The in-vivo data from both active and passive testing conditions for the GM indicate the existence non-uniform sarcomere length distribution on human muscle, extending previous results from in-situ animal experiments [2] and recent modeling studies [34]. These physiologically highly relevant findings support in-vivo presence of myofascial interactions in human muscle, which has major implications for the muscle function in health and disease. Future research can expand the scope of the literature on in-vivo existence of EMFT to other muscles for new testing conditions (e.g., kinesio taping, BTX administration and pos-operative assessment). Nevertheless, translating these findings into a fundemental understanding, and from there into clinical use necessitates a deeper evaluation, going beyond mapping local deformations along fascicles and quantifying position invariant statistical metrics. To that end, we performed comprehensive tests on the validity of demons algoritm. Given the importance of strain heterogeneity pattern [35], the currrent thesis expands these tests to include a multivariate analysis on the impact of tuning parameters on deformation field and implements a cross-modality validation strategy (Chapter 3). As for the accuracy of strain amplitudes, designing an MRI-visible deformable phantom or using publicly available datasets that have been published recently [254, 255, 256] are plausible options for the calibration of the MRI-DTI method.

APPENDIX A. MAGNETIC RESONANCE AND DIFFUSION TENSOR IMAGING ANALYSES INDICATE HETEROGENEOUS STRAINS ALONG HUMAN MEDIAL GASTROCNEMIUS FASCICLES CAUSED BY SUBMAXIMAL PLANTAR-FLEXION ACTIVITY

A.0.1 Mean fiber direction strains of different tracts and its relevance

Mean fiber direction strain along individual tracts were calculated and percentage of tract pairs with different mean strains were used as index for parallel heterogeneity of tract strain. Pair-wise comparisons of mean fiber direction strain along individual tracts within each subject were done based on Kruskal-Wallis with Dunn's post hoc test. Ratio of the number of fiber pairs with statistically different mean strains to the total number of fiber pair combinations quantify parallel distribution of strain per each subject.

Figure A.1 shows mean fiber direction strains of different tracts for each subject within axial cross sections. Index for parallel heterogeneity of tract strain indicates that approximately half of the tracts studied shows different mean strains (51.3%, 51.5%, 48.7%, 51.6% and 57.5% for subjects A, B, C, D and E, respectively). Inter-subject variability is noticeable for mean strain distribution. For subjects A, B and C, most superficial tracts show a positive mean strain, whereas for deeper tracts negative values are calculated. However, for subject D an opposite effect, and for subject E a more complex distribution is found.

It has been shown that with increasing parallel heterogeneity, muscle optimum length shifts to a longer length [35]. Furthermore, variations in partial activation pattern have been shown to affect the nature of the mean strain distribution by finite element modeling [19]. As a result, index for parallel heterogeneity constitutes a

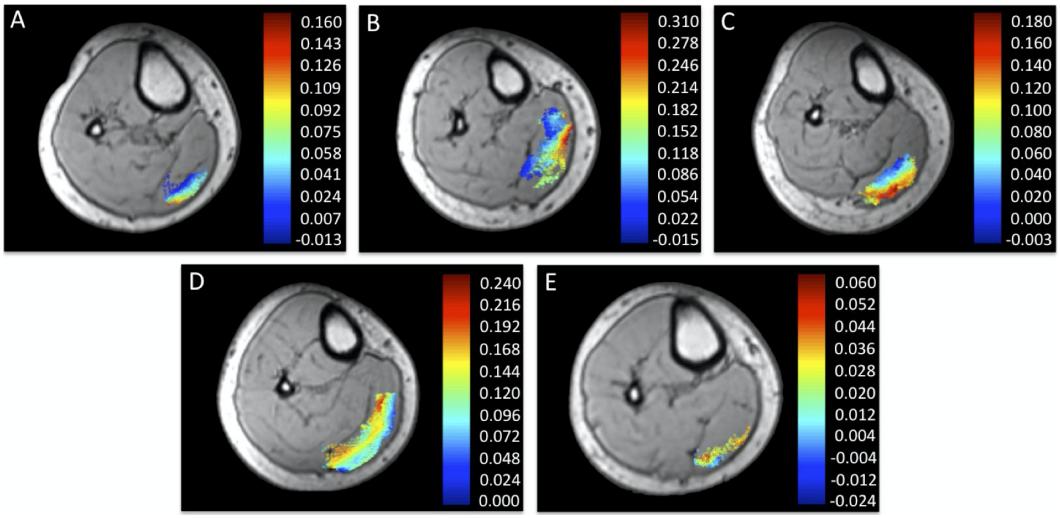

Figure A.1 Parallel distribution of fiber direction strains for each subject. Mean fiber direction strains of different tracts are mapped on a reference cross-sectional slice separately for each subject. The reference slice is chosen so as to maximize the fiber representation within the muscle cross section. Negative values represent shortening and positive values represent lengthening. Strain limits are not normalized to reflect individual parallel distribution differences.

promising parameter for subject specific characterization of in-vivo mechanics of the skeletal muscle and the nature of parallel strain distribution provides promising information to investigate activation patterns for several muscles during various tasks.

APPENDIX B. IN-VIVO ALONG MUSCLE FASCICLE STRAIN HETEROGENEITY IS NOT AFFECTED BY IMAGE REGISTRATION PARAMETERS: ROBUSTNESS TESTING OF COMBINED MAGNETIC RESONANCE-DIFFUSION TENSOR IMAGING METHOD

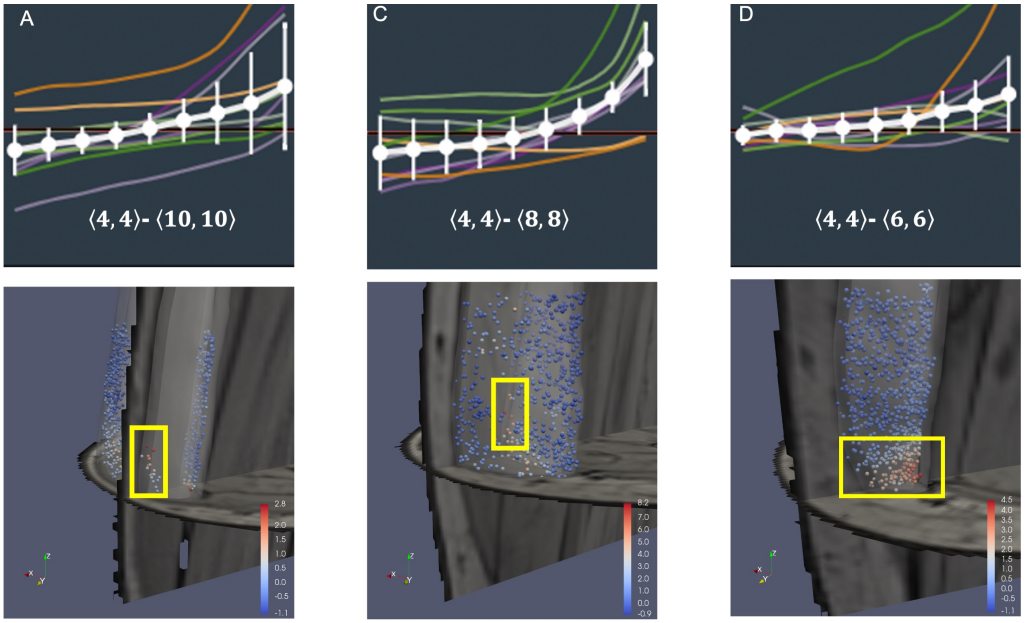

Figure B.1 hjgfd

APPENDIX C. VELOCIMETRY AND QUANTITATIVE MRI FOR CROSS VALIDATION AND MICROSTRUCTURAL ORIGIN ASSESSMENT OF FIBER DIRECTION STRAINS AS CALCULATED BY DEMONS NON RIGID REGISTRATION

C.1 Generalizability and qMRI experiment

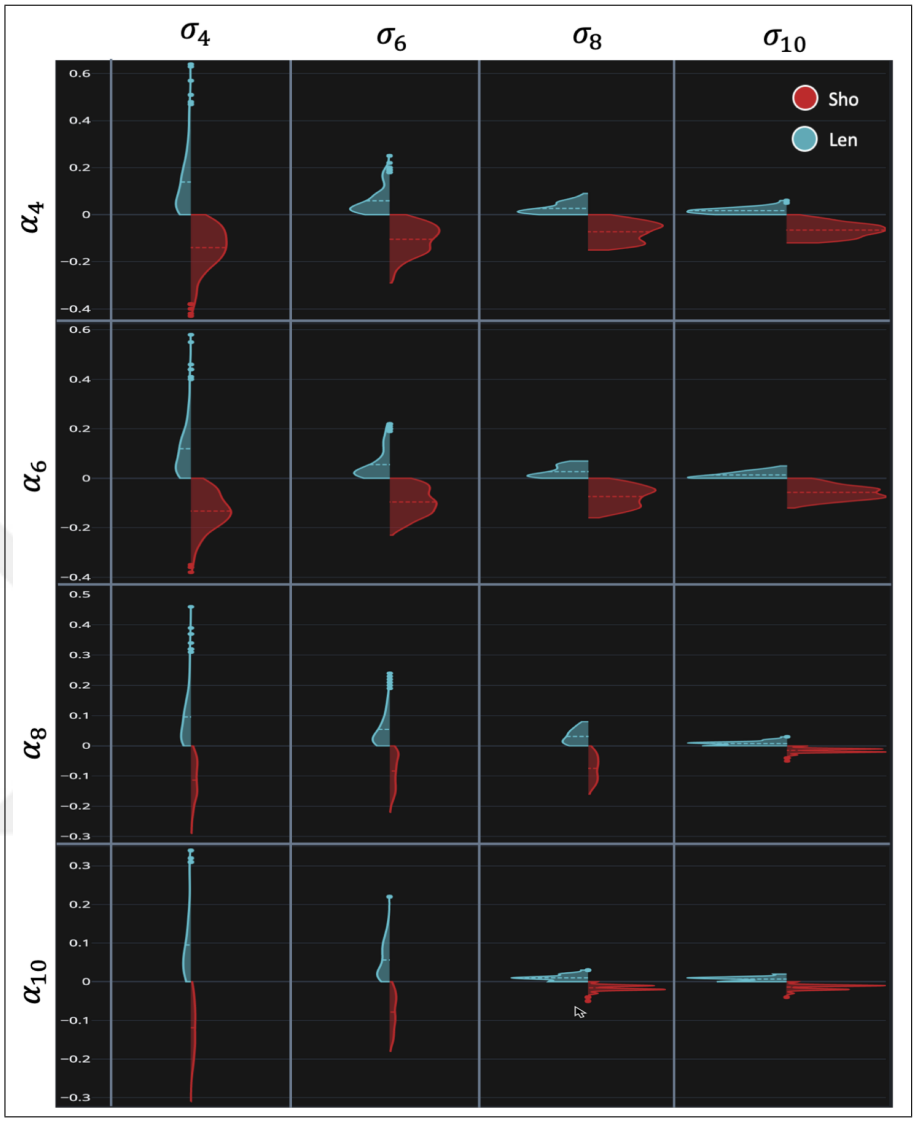

Figure C.1 Split-violin plot matrix visualizing the serial fiber direction shortening (red) and lengthening (turquoise) distributions yielded by paired alpha (rows) and sigma (columns) combinations. Suspected outliers (1.5 interquartile range far from the median) were represented by markers, whereas outliers were discarded from violin plots.

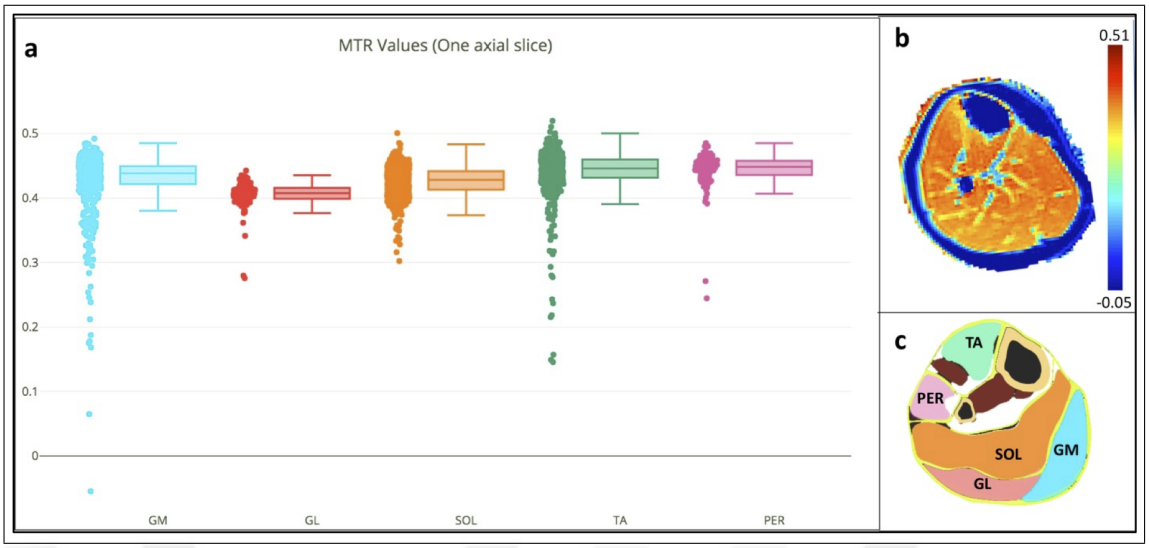

Figure C.2 (a) Box and whisker plots for magnetization transfer ratio (MTR) distribution in medial gastrocnemius (GM), lateral gastrocnemius (GL), soleus (SOL), tibialis anterior (TA) and peroneus (PER) muscles. (b) Axial cross-section of MTR map. (c) Region of interest (ROI) masks. Small interquartile ranges indicate low variability in the distribution of MTR vales in axial cross-sections for all ROIs. All target muscles appear to have a quite similar mean MTR value with noticeable number of outliers.

C.2 Velocimetry experiment

C.2.1 On the difference between VE-PC strain rates and registration-based strains

Velocity-encoded phase-contrast images map voxelwise velocity information based on a maximum flow rate set by the velocity encoding (VENC) parameter (e.g., 10cm/sec as in Table 4.3). Based on this set limit, flow information can be captured (and scaled) based on the phase shift induced (from -180°to 180°) at each voxel due to motion, including the direction of the flow (forward or reverse to the imaging plane). As a result, a 2D velocity field is obtained with the standard VE-PC sequence. Using compressed sensing acceleration, 3D velocity maps can be obtained.

The partial derivative in each direction of the velocity field $V(x, y)$ (i.e., the Jacobian of the velocity field $()\nabla V$) yields the velocity gradient tensor L. In 2D ($V(x) = ux + vy$), where x is the *current coordinate*, the velocity gradient tensor is

given as:

$$L = \frac{\partial v}{\partial x} = \nabla V = \begin{pmatrix} \frac{\partial u}{x} & \frac{\partial u}{y} \\ \frac{\partial v}{x} & \frac{\partial v}{y} \end{pmatrix} \tag{C.1}$$

The relationship between velocity and velocity gradient tensor is akin to that between the displacement and deformation gradient tensors. One essential difference is that the spatial derivative of L is taken with respect to the current location, not with respect to a reference coordinate as in the deformation gradient tensor which is expressed in the Lagrangian specification, where points are followed through time and the coordinates are fixed in the material. Hence, L is an Eulerian description (coordinates are fixed in space) of an instantanious *change of the speed* in each direction when a particle is moved within that field by a certain distance in a certain direction. Figure C.3 illustrates the key difference between these definitions.

If all points move in the same direction at the same speed, L equals zero. Deformation occurs only when the points attain different velocities. In this calse, L can be split into strain rate (D) and rotation (Ω) tensors, symmetric and assymetric parts of the L, respectively. The former defines the rate at which the deformation (stretching and shearing) occurs, whereas the letter defines the rate of rotation. The strain rate tensor is given by:

$$D = \begin{pmatrix} \frac{\partial u}{x} & \frac{1}{2}(\frac{\partial u}{x} + \frac{\partial u}{y}) \\ \frac{1}{2}(\frac{\partial u}{y} + \frac{\partial v}{x}) & \frac{\partial v}{y} \end{pmatrix} = \frac{1}{2}(L + L^T) \tag{C.2}$$

The diagonals of D represent stretching, whereas the non-diagonal components define shearing. Eigenspace decomposition yields eigenvalues and eigenvectors that define the principle magnitudes and orientations of D. In other words, eigenvalues (λ_1, λ_2,

λ_3) express the (either positive or negative) maximal values the diagonal components can take. The notation followed by Sinha et al. (2015) is that maximum positive eigenvalue (λ_2) corresponds to the extension rate, whereas the minimum negative eigenvalue is the contraction rate (λ_3). The intermediate component (λ_2) is expected in a much smaller magnitude, and could be either expansion or contraction. For further details on this convention, the reader is referred to [258].

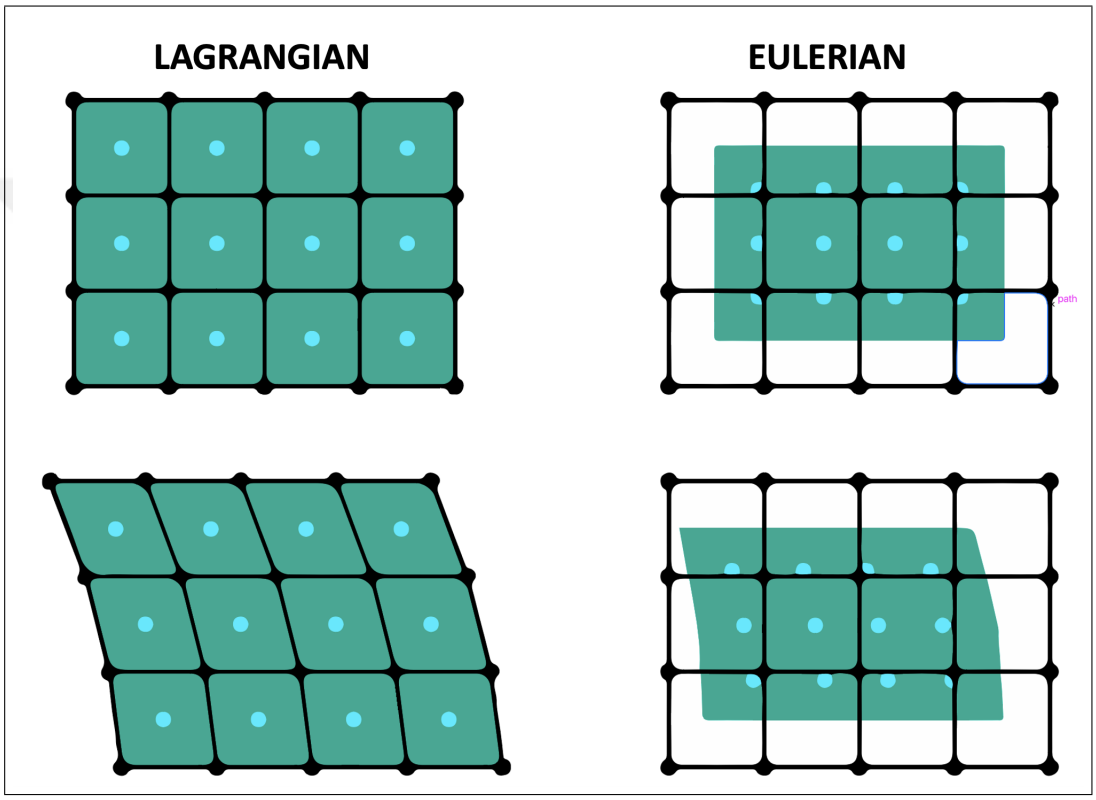

Figure C.3 Illustration of the difference between Lagrangian and Eulerian mesh descriptions. In Lagrangian coordinates, the relative position of material points (blue dots) remain stationary against the grid locations (black dots on the mesh) as the material deforms. In other words, the material coordinates are fixed, the mesh deforms with the material. In Eulerian coordinates, the material coordinates (blue dots) change in time, whereas the grid locations (black dots) remain constant.

It is worth noting that the mathemetical operations applied on VE-PC encoded images are borrowed from the field of fluid mechanics to study the kinematics of skeletal muscle. This approximates soft tissue as a continuos distribution of small fluid elements. For example, the local stifness of a solid described in the Lagrangian coordinates (more favorable for studying solids in a large deformation regime, see section 1.3.1) corresponds to the viscosity of a fluid element in Eulerian coordinate (more fa-

vorable for studying fluids). There are some drawbacks in studying muscle deformation using Eulerian descriptions, as muscle is a history-dependent material and boundary conditions are not easily applicable in Eulerian coordinates. When comparing SR from VE-PC to fiber direction strains derived from the displacement field, these fundamental differences should be bear in mind. The material derivative links such Eulerian and Lagrangian descriptions of continuum deformation. However, raw data for 2D and 4D PC images were not available to explore options for providing a more objective comparison basis for registration-based strains. Still, a side by side qualitative comparison of the distribution patterns of VE-PC based deformation trends and registration-based strains offers valuable information for testing the validity of fiber-direction strain heterogeneity.

REFERENCES

1. Raza, A., "What scientific term or concept ought to be more widely known?," 2022.

2. Yucesoy, C. A., "Epimuscular myofascial force transmission implies novel principles for muscular mechanics," *Exerc Sport Sci Rev*, Vol. 38, pp. 128--134, July 2010.

3. Morgan, S. C., and C. C. Parker, "Local treatment of metastatic cancer—killing the seed or disturbing the soil?," *Nature reviews Clinical oncology*, Vol. 8, no. 8, pp. 504–506, 2011.

4. Paget, S., "The distribution of secondary growths in cancer of the breast.," *The Lancet*, Vol. 133, no. 3421, pp. 571–573, 1889.

5. Langley, R. R., and I. J. Fidler, "The seed and soil hypothesis revisited—the role of tumor,Äêstroma interactions in metastasis to different organs," *International journal of cancer*, Vol. 128, no. 11, pp. 2527–2535, 2011.

6. Kinsey, D. L., "An experimental study of preferential metastasis," *Cancer*, Vol. 13, no. 4, pp. 674–676, 1960.

7. Schackert, G., and I. J. Fidler, "Site-specific metastasis of mouse melanomas and a fibrosarcoma in the brain or meninges of syngeneic animals," *Cancer research*, Vol. 48, no. 12, pp. 3478–3484, 1988.

8. Hawkins, D., and M. Bey, "Muscle and tendon forcelength properties and their interactions in vivo," *J Biomech*, Vol. 30, pp. 63--70, Jan. 1997.

9. Huijing, P. A., "Epimuscular myofascial force transmission: a historical review and implications for new research. international society of biomechanics muybridge award lecture, taipei, 2007," *J Biomech*, Vol. 42, pp. 9--21, Jan. 2009.

10. Rijkelijkhuizen, J. M., H. J. M. Meijer, G. C. Baan, and P. A. Huijing, "Myofascial force transmission also occurs between antagonistic muscles located within opposite compartments of the rat lower hind limb," *J Electromyogr Kinesiol*, Vol. 17, pp. 690--697, Dec. 2007.

11. Yucesoy, C. A., F. Ateş, U. Akgün, and M. Karahan, "Measurement of human gracilis muscle isometric forces as a function of knee angle, intraoperatively," *Journal of Biomechanics*, Vol. 43, no. 14, pp. 2665–2671, 2010.

12. Huijing, P. A., and G. C. Baan, "Extramuscular myofascial force transmission within the rat anterior tibial compartment: proximodistal differences in muscle force," *Acta Physiol. Scand.*, Vol. 173, pp. 297--311, Nov. 2001.

13. Berthier, C., and S. Blaineau, "Supramolecular organization of the subsarcolemmal cytoskeleton of adult skeletal muscle fibers. a review," *Biol. Cell*, Vol. 89, pp. 413--434, Oct. 1997.

14. Yucesoy, C. A., G. C. Baan, B. H. F. J. M. Koopman, H. J. Grootenboer, and P. A. Huijing, "Prestrained epimuscular connections cause muscular myofascial force transmission to affect properties of synergistic 'ehl' and 'edl' muscles of the rat," *J Biomech Eng*, Vol. 127, pp. 819--828, Oct. 2005.

15. Yucesoy, C. A., B. H. F. J. M. Koopman, G. C. Baan, H. J. Grootenboer, and P. A. Huijing, "Effects of inter and extramuscular myofascial force transmission on adjacent synergistic muscles: assessment by experiments and finiteelement modeling," *J Biomech*, Vol. 36, pp. 1797--1811, Dec. 2003.

16. Yucesoy, C. A., and P. A. Huijing, "Substantial effects of epimuscular myofascial force transmission on muscular mechanics have major implications on spastic muscle and remedial surgery," *J Electromyogr Kinesiol*, Vol. 17, pp. 664--679, Dec. 2007.

17. Yucesoy, C. A., B. H. F. J. M. Koopman, P. A. Huijing, and H. J. Grootenboer, "Three-dimensional finite element modeling of skeletal muscle using a twodomain approach: linked fibermatrix mesh model," *J Biomech*, Vol. 35, pp. 1253--1262, Sept. 2002.

18. Yucesoy, C. A., H. Maas, B. H. F. J. M. Koopman, H. J. Grootenboer, and P. A. Huijing, "Mechanisms causing effects of muscle position on proximo-distal muscle force differences in extra-muscular myofascial force transmission," *Medical Engineering & Physics*, Vol. 28, no. 3, pp. 214–226, 2006.

19. Turkoglu, A. N., P. A. Huijing, and C. A. Yucesoy, "Mechanical principles of effects of botulinum toxin on muscle lengthforce characteristics: an assessment by finite element modeling," *J Biomech*, Vol. 47, pp. 1565--1571, May 2014.

20. Turkoglu, A. N., and C. A. Yucesoy, "Simulation of effects of botulinum toxin on muscular mechanics in time course of treatment based on adverse extracellular matrix adaptations," *J Biomech*, Vol. 49, no. 7, pp. 1192--1198, 2016.

21. Yucesoy, C. A., O. Emre Arikan, and F. Ates, "Btx-a administration to the target muscle affects forces of all muscles within an intact compartment and epimuscular myofascial force transmission," *Journal of biomechanical engineering*, Vol. 134, no. 11, 2012.

22. Kaya, C. S., F. Bilgili, N. E. Akalan, and C. A. Yucesoy, "Intraoperative testing of passive and active state mechanics of spastic semitendinosus in conditions involving intermuscular mechanical interactions and gait relevant joint positions," *Journal of Biomechanics*, Vol. 103, 2020.

23. Yilmaz, E. O., C. S. Kaya, Z. D. Akdeniz-Doğan, and C. A. Yucesoy, "Long-term btx-a effects on bi-articular muscle: Higher passive force, limited length range of active force production and unchanged intermuscular interactions," *Journal of Biomechanics*, Vol. 126, p. 110627, 2021.

24. Huijing, P. A., H. Maas, and G. C. Baan, "Compartmental fasciotomy and isolating a muscle from neighboring muscles interfere with myofascial force transmission within the rat anterior crural compartment," *Journal of morphology*, Vol. 256, no. 3, pp. 306–321, 2003.

25. Huxley, A. F., "Muscle structure and theories of contraction," *Prog Biophys Biophys Chem*, Vol. 7, pp. 255--318, 1957.

26. Huxley, A. F., and R. Niedergerke, "Measurement of the striations of isolated muscle fibres with the interference microscope," *J. Physiol. (Lond.)*, Vol. 144, pp. 403--425, Dec. 1958.

27. Powers, K., G. SchappacherTilp, A. Jinha, T. Leonard, K. Nishikawa, and W. Herzog, "Titin force is enhanced in actively stretched skeletal muscle," *Journal of Experimental Biology*, Vol. 217, pp. 3629--3636, Oct. 2014.

28. Herzog, W., "Mechanisms of enhanced force production in lengthening (eccentric) muscle contractions," *Journal of Applied Physiology*, Vol. 116, pp. 1407--1417, June 2014.

29. Rassier, D. E., E.-J. Lee, and W. Herzog, "Modulation of passive force in single skeletal muscle fibres," *Biol. Lett.*, Vol. 1, pp. 342--345, Sept. 2005.

30. Herzog, W., and T. R. Leonard, "Force enhancement following stretching of skeletal muscle: a new mechanism," *J. Exp. Biol.*, Vol. 205, pp. 1275--1283, May 2002.

31. Rode, C., T. Siebert, and R. Blickhan, "Titininduced force enhancement and force depression: a 'stickyspring' mechanism in muscle contractions?," *J. Theor. Biol.*, Vol. 259, pp. 350--360, July 2009.

32. Tomalka, A., C. Rode, J. Schumacher, and T. Siebert, "The active forcelength relationship is invisible during extensive eccentric contractions in skinned skeletal muscle fibres," *Proc. Biol. Sci.*, Vol. 284, May 2017.

33. Nishikawa, K. C., J. A. Monroy, T. E. Uyeno, S. H. Yeo, D. K. Pai, and S. L. Lindstedt, "Is titin a 'winding filament'? a new twist on muscle contraction," *Proceedings of the Royal Society B: Biological Sciences*, Vol. 279, pp. 981--990, Mar. 2012.

34. Cankaya, A. O., U. Pamuk, and C. A. Yucesoy, "The effects of an activation-dependent increase in titin stiffness on whole muscle properties using finite element modeling," *Journal of Biomechanics*, Vol. 116, p. 110197, 2021.

35. Willems, M. E., and P. A. Huijing, "Heterogeneity of mean sarcomere length in different fibres: effects on length range of active force production in rat muscle," *Eur J Appl Physiol Occup Physiol*, Vol. 68, no. 6, pp. 489--496, 1994.

36. Sarvazyan, A. P., M. W. Urban, and J. F. Greenleaf, "Acoustic waves in medical imaging and diagnostics," *Ultrasound in medicine & biology*, Vol. 39, no. 7, pp. 1133–1146, 2013.

37. Ateş, F., F. Hug, K. Bouillard, M. Jubeau, T. Frappart, M. Couade, J. Bercoff, and A. Nordez, "Muscle shear elastic modulus is linearly related to muscle torque over the entire range of isometric contraction intensity," *Journal of Electromyography and Kinesiology*, Vol. 25, no. 4, pp. 703–708, 2015.

38. Glaser, K. J., A. Manduca, and R. L. Ehman, "Review of mr elastography applications and recent developments," *Journal of Magnetic Resonance Imaging*, Vol. 36, no. 4, pp. 757–774, 2012.

39. Ho, L. C., I. A. Sigal, N.-J. Jan, X. Yang, Y. Van Der Merwe, Y. Yu, Y. Chau, C. K. Leung, I. P. Conner, and T. Jin, "Non-invasive mri assessments of tissue microstructures and macromolecules in the eye upon biomechanical or biochemical modulation," *Scientific reports*, Vol. 6, no. 1, pp. 1–14, 2016.

40. Kakkad, S., J. Zhang, A. Akhbardeh, D. Jacob, B. Krishnamachary, M. Solaiyappan, M. A. Jacobs, V. Raman, D. Leibfritz, and K. Glunde, "Collagen fibers mediate mri-detected water diffusion and anisotropy in breast cancers," *Neoplasia*, Vol. 18, no. 10, pp. 585–593, 2016.

41. Ma, Y., E. Y. Chang, G. M. Bydder, and J. Du, "Can ultrashort,Äête (ute) mri sequences on a 3,Äêt clinical scanner detect signal directly from collagen protons: freeze–dry and d2o exchange studies of cortical bone and achilles tendon specimens," *NMR in Biomedicine*, Vol. 29, no. 7, pp. 912–917, 2016.

42. Martel, G., C. Couture, G. Gilbert, S. Bancelin, H. Richard, T. Moser, S. Kiss, F. Légaré, and S. Laverty, "Femoral epiphyseal cartilage matrix changes at predilection sites of equine osteochondrosis: quantitative mri, second,Äêharmonic microscopy, and histological findings," *Journal of Orthopaedic Research*, Vol. 34, no. 10, pp. 1743–1752, 2016.

43. Kawakami, Y., Y. Ichinose, and T. Fukunaga, "Architectural and functional features of human triceps surae muscles during contraction," *J. Appl. Physiol.*, Vol. 85, pp. 398--404, Aug. 1998.

44. Kinugasa, R., Y. Kawakami, and T. Fukunaga, "Muscle activation and its distribution within human triceps surae muscles," *Journal of Applied Physiology*, Vol. 99, pp. 1149–1156, 2022/07/21 2005.

45. Kinugasa, R., Y. Kawakami, S. Sinha, and T. Fukunaga, "Unique spatial distribution of in vivo human muscle activation," *Experimental Physiology*, Vol. 96, pp. 938–948, 2022/07/21 2011.

46. Maganaris, C. N., "Force–length characteristics of in vivo human skeletal muscle," *Acta Physiologica Scandinavica*, Vol. 172, no. 4, pp. 279–285, 2001.

47. Bojsen-Møller, J., P. Hansen, P. Aagaard, U. Svantesson, M. Kjaer, and S. P. Magnusson, "Differential displacement of the human soleus and medial gastrocnemius aponeuroses during isometric plantar flexor contractions in vivo," *Journal of applied physiology*, Vol. 97, no. 5, pp. 1908–1914, 2004.

48. BojsenMøller, J., S. Schwartz, K. K. Kalliokoski, T. Finni, and S. P. Magnusson, "Intermuscular force transmission between human plantarflexor muscles in vivo," *J. Appl. Physiol.*, Vol. 109, pp. 1608--1618, Dec. 2010.

49. Rana, M., G. Hamarneh, and J. M. Wakeling, "3d fascicle orientations in triceps surae," *J. Appl. Physiol.*, Vol. 115, pp. 116--125, July 2013.

50. Axel, L., and L. Dougherty, "Mr imaging of motion with spatial modulation of magnetization.," *Radiology*, Vol. 171, no. 3, pp. 841–845, 1989.

51. Bittoun, J., E. Bourroul, O. Jolivet, I. Idy,ÄêPeretti, E. Mousseaux, A. Tardivon, and P. Peronneau, "High,Äêprecision mr velocity mapping by 3d,Äêfourier phase encoding with a small number of encoding steps," *Magnetic resonance in medicine*, Vol. 29, no. 5, pp. 674–680, 1993.

52. Lustig, M., D. L. Donoho, J. M. Santos, and J. M. Pauly, "Compressed sensing mri," *IEEE signal processing magazine*, Vol. 25, no. 2, pp. 72–82, 2008.

53. Ma, D., V. Gulani, N. Seiberlich, K. Liu, J. L. Sunshine, J. L. Duerk, and M. A. Griswold, "Magnetic resonance fingerprinting," *Nature*, Vol. 495, no. 7440, pp. 187–192, 2013.

54. Mazzoli, V., L. M. Gottwald, E. S. Peper, M. Froeling, B. F. Coolen, N. Verdonschot, A. M. Sprengers, P. van Ooij, G. J. Strijkers, and A. J. Nederveen, "Accelerated 4d phase contrast mri in skeletal muscle contraction," *Magnetic Resonance in Medicine*, Vol. 80, pp. 1799–1811, 2022/07/29 2018.

55. Malis, V., U. Sinha, and S. Sinha, "Compressed sensing velocity encoded phase contrast imaging: Monitoring skeletal muscle kinematics," *Magnetic Resonance in Medicine*, Vol. 84, no. 1, pp. 142–156, 2020.

56. Malis, V., U. Sinha, and S. Sinha, "3d muscle deformation mapping at submaximal isometric contractions: applications to aging muscle," *Frontiers in physiology*, Vol. 11, p. 600590, 2020.

57. Yaman, A., C. Ozturk, P. A. Huijing, and C. A. Yucesoy, "Magnetic resonance imaging assessment of mechanical interactions between human lower leg muscles in vivo," *J Biomech Eng*, Vol. 135, p. 91003, Sept. 2013.

58. Gao, H., A. Allan, C. McComb, X. Luo, and C. Berry, "Left ventricular strain and its pattern estimated from cine cmr and validation with dense," *Phys Med Biol*, Vol. 59, pp. 3637--3656, July 2014.

59. Wang, H., L. Dong, J. O'Daniel, R. Mohan, A. S. Garden, K. K. Ang, D. A. Kuban, M. Bonnen, J. Y. Chang, and R. Cheung, "Validation of an accelerated 'demons' algorithm for deformable image registration in radiation therapy," *Phys Med Biol*, Vol. 50, pp. 2887--2905, June 2005.

60. Pamuk, U., and C. A. Yucesoy, "Mri analyses show that kinesio taping affects much more than just the targeted superficial tissues and causes heterogeneous deformations within the whole limb," *J Biomech*, Vol. 48, pp. 4262--4270, Dec. 2015.

61. Huijing, P. A., A. Yaman, C. Ozturk, and C. A. Yucesoy, "Effects of knee joint angle on global and local strains within human triceps surae muscle: Mri analysis indicating in vivo myofascial force transmission between synergistic muscles," *Surg Radiol Anat*, Vol. 33, pp. 869--879, Dec. 2011.

62. Jbabdi, S., and H. Johansen-Berg, "Tractography: where do we go from here?," *Brain connectivity*, Vol. 1, no. 3, pp. 169–183, 2011.

63. Maffei, C., G. Girard, K. G. Schilling, D. B. Aydogan, N. Adluru, A. Zhylka, Y. Wu, M. Mancini, A. Hamamci, and A. Sarica, "Insights from the irontract challenge: optimal methods for mapping brain pathways from multi-shell diffusion mri," *NeuroImage*, Vol. 257, p. 119327, 2022.

64. Steven, A. J., J. Zhuo, and E. R. Melhem, "Diffusion kurtosis imaging: an emerging technique for evaluating the microstructural environment of the brain," *American journal of roentgenology*, Vol. 202, no. 1, pp. W26–W33, 2014.

65. Lu, H., J. H. Jensen, A. Ramani, and J. A. Helpern, "Three,Äêdimensional characterization of non,Äêgaussian water diffusion in humans using diffusion kurtosis imaging," *NMR in Biomedicine: An International Journal Devoted to the Development and Application of Magnetic Resonance In vivo*, Vol. 19, no. 2, pp. 236–247, 2006.

66. Assaf, Y., and P. J. Basser, "Composite hindered and restricted model of diffusion (charmed) mr imaging of the human brain," *Neuroimage*, Vol. 27, no. 1, pp. 48–58, 2005.

67. Assaf, Y., T. Blumenfeld,ÄêKatzir, Y. Yovel, and P. J. Basser, "Axcaliber: a method for measuring axon diameter distribution from diffusion mri," *Magnetic Resonance in Medicine: An Official Journal of the International Society for Magnetic Resonance in Medicine*, Vol. 59, no. 6, pp. 1347–1354, 2008.

68. Zhang, H., T. Schneider, C. A. Wheeler-Kingshott, and D. C. Alexander, "Noddi: practical in vivo neurite orientation dispersion and density imaging of the human brain," *Neuroimage*, Vol. 61, no. 4, pp. 1000–1016, 2012.

69. Oudeman, J., A. J. Nederveen, G. J. Strijkers, M. Maas, P. R. Luijten, and M. Froeling, "Techniques and applications of skeletal muscle diffusion tensor imaging: a review," *Journal of Magnetic Resonance Imaging*, Vol. 43, no. 4, pp. 773–788, 2016.

70. Levin, D. I., B. Gilles, B. Mädler, and D. K. Pai, "Extracting skeletal muscle fiber fields from noisy diffusion tensor data," *Medical Image Analysis*, Vol. 15, no. 3, pp. 340–353, 2011.

71. Damon, B. M., "Effects of image noise in muscle diffusion tensor (dt)mri assessed using numerical simulations," *Magn Reson Med*, Vol. 60, pp. 934--944, Oct. 2008.

72. Froeling, M., A. J. Nederveen, K. Nicolay, and G. J. Strijkers, "Dti of human skeletal muscle: the effects of diffusion encoding parameters, signal,Äêto,Äênoise ratio and t2 on tensor indices and fiber tracts," *NMR in Biomedicine*, Vol. 26, no. 11, pp. 1339–1352, 2013.

73. Hooijmans, M. T., B. M. Damon, M. Froeling, M. J. Versluis, J. Burakiewicz, J. J. G. M. Verschuuren, E. H. Niks, A. G. Webb, and H. E. Kan, "Evaluation of skeletal muscle dti in patients with duchenne muscular dystrophy," *NMR in Biomedicine*, Vol. 28, pp. 1589–1597, 2022/07/30 2015.

74. Van Donkelaar, C. C., L. J. Kretzers, P. H. Bovendeerd, L. M. Lataster, K. Nicolay, J. D. Janssen, and M. R. Drost, "Diffusion tensor imaging in biomechanical studies of skeletal muscle function," *J. Anat.*, Vol. 194 (Pt 1), pp. 79--88, Jan. 1999.

75. Alexander, A. L., J. E. Lee, M. Lazar, and A. S. Field, "Diffusion tensor imaging of the brain," *Neurotherapeutics*, Vol. 4, no. 3, pp. 316–329, 2007.

76. Sinha, S., and U. Sinha, "Reproducibility analysis of diffusion tensor indices and fiber architecture of human calf muscles in vivo at 1.5 tesla in neutral and plantarflexed ankle positions at rest," *Journal of Magnetic Resonance Imaging*, Vol. 34, pp. 107--119, July 2011.

77. Heemskerk, A. M., T. K. Sinha, K. J. Wilson, Z. Ding, and B. M. Damon, "Quantitative assessment of dti,Äêbased muscle fiber tracking and optimal tracking parameters," *Magnetic Resonance in Medicine: An Official Journal of the International Society for Magnetic Resonance in Medicine*, Vol. 61, no. 2, pp. 467–472, 2009.

78. Berry, D. B., B. Regner, V. Galinsky, S. R. Ward, and L. R. Frank, "Relationships between tissue microstructure and the diffusion tensor in simulated skeletal muscle," *Magnetic Resonance in Medicine*, Vol. 80, pp. 317–329, 2022/07/30 2018.

79. Sigmund, E. E., D. Sui, O. Ukpebor, S. Baete, E. Fieremans, J. S. Babb, M. Mechlin, K. Liu, J. Kwon, and K. Mcgorty, "Stimulated echo diffusion tensor imaging and spair t2,Äêweighted imaging in chronic exertional compartment syndrome of the lower leg muscles," *Journal of Magnetic Resonance Imaging*, Vol. 38, no. 5, pp. 1073–1082, 2013.

80. Damon, B. M., Z. Ding, A. W. Anderson, A. S. Freyer, and J. C. Gore, "Validation of diffusion tensor mribased muscle fiber tracking," *Magn Reson Med*, Vol. 48, pp. 97--104, July 2002.

81. Bolsterlee, B., T. Finni, A. D'Souza, J. Eguchi, E. C. Clarke, and R. D. Herbert, "Three-dimensional architecture of the whole human soleus muscle in vivo," *PeerJ*, Vol. 6, p. e4610, 2018.

82. Pamuk, U., A. Karakuzu, C. Ozturk, B. Acar, and C. A. Yucesoy, "Combined magnetic resonance and diffusion tensor imaging analyses provide a powerful tool for in vivo assessment of deformation along human muscle fibers," *J Mech Behav Biomed Mater*, Vol. 63, pp. 207--219, 2016.

83. Schwenzer, N. F., G. Steidle, P. Martirosian, C. Schraml, F. Springer, C. D. Claussen, and F. Schick, "Diffusion tensor imaging of the human calf muscle: distinct changes in fractional anisotropy and mean diffusion due to passive muscle shortening and stretching," *NMR Biomed*, Vol. 22, pp. 1047--1053, Dec. 2009.

84. Zaraiskaya, T., D. Kumbhare, and M. D. Noseworthy, "Diffusion tensor imaging in evaluation of human skeletal muscle injury," *Journal of Magnetic Resonance Imaging: An Official Journal of the International Society for Magnetic Resonance in Medicine*, Vol. 24, no. 2, pp. 402–408, 2006.

85. Heemskerk, A. M., G. J. Strijkers, M. R. Drost, G. S. van Bochove, and K. Nicolay, "Skeletal muscle degeneration and regeneration after femoral artery ligation in mice: monitoring with diffusion mr imaging," *Radiology*, Vol. 243, no. 2, pp. 413–421, 2007.

86. Longwei, X., "Clinical application of diffusion tensor magnetic resonance imaging in skeletal muscle," *Muscles, ligaments and tendons journal*, Vol. 2, no. 1, p. 19, 2012.

87. Karakuzu, A., U. Pamuk, C. Ozturk, B. Acar, and C. A. Yucesoy, "Magnetic resonance and diffusion tensor imaging analyses indicate heterogeneous strains along human medial gastrocnemius fascicles caused by submaximal plantarflexion activity," *Journal of Biomechanics*, Vol. 57, pp. 69--78, May 2017.

88. Baete, S. H., G. Y. Cho, and E. E. Sigmund, "Dynamic diffusion,Äêtensor measurements in muscle tissue using the single,Äêline multiple,Äêecho diffusion,Äêtensor acquisition technique at 3t," *NMR in Biomedicine*, Vol. 28, no. 6, pp. 667–678, 2015.

89. Fouré, A., A. C. Ogier, A. Le Troter, C. Vilmen, T. Feiweier, M. Guye, J. Gondin, P. Besson, and D. Bendahan, "Diffusion properties and 3d architecture of human lower leg muscles assessed with ultra-high-field-strength diffusion-tensor mr imaging and tractography: Reproducibility and sensitivity to sex difference and intramuscular variability," *Radiology*, Vol. 287, pp. 592–607, 2022/07/30 2018.

90. Ashburner, J., and K. J. Friston, "Voxel-based morphometry—the methods," *Neuroimage*, Vol. 11, no. 6, pp. 805–821, 2000.

91. Fox, N. C., W. R. Crum, R. I. Scahill, J. M. Stevens, J. C. Janssen, and M. N. Rossor, "Imaging of onset and progression of alzheimer's disease with voxel-compression mapping of serial magnetic resonance images," *The Lancet*, Vol. 358, no. 9277, pp. 201–205, 2001.

92. Ashburner, J., "Spm: a history," *Neuroimage*, Vol. 62, no. 2, pp. 791–800, 2012.

93. Herbert, R. D., B. Bolsterlee, and S. C. Gandevia, "Passive changes in muscle length," *J. Appl. Physiol.*, Dec. 2018.

94. *Fast deformable registration on the GPU: A CUDA implementation of demons*, IEEE, 2008.

95. Vercauteren, T., X. Pennec, A. Perchant, and N. Ayache, "Diffeomorphic demons: efficient nonparametric image registration," *Neuroimage*, Vol. 45, pp. S61--72, Mar. 2009.

96. Bricault, I., G. Ferretti, and P. Cinquin, "Registration of real and ct-derived virtual bronchoscopic images to assist transbronchial biopsy," *IEEE transactions on medical imaging*, Vol. 17, no. 5, pp. 703–714, 1998.

97. Webb, J., A. Guimond, P. Eldridge, D. Chadwick, J. Meunier, J.-P. Thirion, and N. Roberts, "Automatic detection of hippocampal atrophy on magnetic resonance images," *Magnetic Resonance Imaging*, Vol. 17, no. 8, pp. 1149–1161, 1999.

98. *Understanding the demons algorithm: 3D non-rigid registration by gradient descent*, Springer, 1999.

99. Shi, J., J.-Y. Guo, S.-X. Hu, and Y.-P. Zheng, "Recognition of finger flexion motion from ultrasound image: A feasibility study," *Ultrasound in Medicine & Biology*, Vol. 38, pp. 1695--1704, Oct. 2012.

100. Latifi, K., G. Zhang, M. Stawicki, W. van Elmpt, A. Dekker, and K. Forster, "Validation of three deformable image registration algorithms for the thorax," *Journal of Applied Clinical Medical Physics*, Vol. 14, pp. 19--30, Jan. 2013.

101. Fedorov, A., E. Billet, M. Prastawa, G. Gerig, A. Radmanesh, S. K. Warfield, R. Kikinis, and N. Chrisochoides, "Evaluation of brain mri alignment with the robust hausdorff distance measures," in *Advances in Visual Computing* (Hutchison, D., T. Kanade, J. Kittler, J. M. Kleinberg, F. Mattern, J. C. Mitchell, M. Naor, O. Nierstrasz, C. Pandu Rangan, B. Steffen, M. Sudan, D. Terzopoulos, D. Tygar, M. Y. Vardi, G. Weikum, G. Bebis, R. Boyle, B. Parvin, D. Koracin, P. Remagnino, F. Porikli, J. Peters, J. Klosowski, L. Arns, Y. K. Chun, T.-M. Rhyne, and L. Monroe, eds.), Vol. 5358, pp. 594--603, Berlin, Heidelberg: Springer Berlin Heidelberg, 2008.

102. Chen, X., Y. Yang, X. Cai, D. A. Auger, C. H. Meyer, M. Salerno, and F. H. Epstein, "Accelerated two-dimensional cine dense cardiovascular magnetic resonance using compressed sensing and parallel imaging," *Journal of Cardiovascular Magnetic Resonance*, Vol. 18, no. 1, p. 38, 2016.

103. Samant, S., S. Lee, and S. Samant, *GPU-Based Unimodal Deformable Image Registration in Radiation Therapy*, Vol. 129, pp. 129–148. CRC Press, 2015.

104. Briem, K., H. Eythörsdöttir, R. G. Magnúsdóttir, R. Pálmarsson, T. Rúnarsdöttir, and T. Sveinsson, "Effects of kinesio tape compared with nonelastic sports tape and the untaped ankle during a sudden inversion perturbation in male athletes," *J Orthop Sports Phys Ther*, Vol. 41, pp. 328--335, May 2011.

105. Lee, M. H., C. R. Lee, J. S. Park, S. Y. Lee, T. G. Jeong, G. S. Son, J. Y. Lee, E. C. Kim, and Y. K. Kim, "Influence of kinesio taping on the motor neuron conduction velocity," *Journal of Physical Therapy Science*, Vol. 23, no. 2, pp. 313--315, 2011.

106. Vovk, U., F. Pernus, and B. Likar, "A review of methods for correction of intensity inhomogeneity in mri," *IEEE transactions on medical imaging*, Vol. 26, no. 3, pp. 405–421, 2007.

107. Belaroussi, B., J. Milles, S. Carme, Y. M. Zhu, and H. Benoit-Cattin, "Intensity non-uniformity correction in mri: existing methods and their validation," *Medical image analysis*, Vol. 10, no. 2, pp. 234–246, 2006.

108. Sled, J. G., and G. B. Pike, "Standing-wave and rf penetration artifacts caused by elliptic geometry: an electrodynamic analysis of mri," *IEEE transactions on medical imaging*, Vol. 17, no. 4, pp. 653–662, 1998.

109. Haase, A., "Snapshot flash mri. applications to t1, t2, and chemical,Äêshift imaging," *Magnetic Resonance in Medicine*, Vol. 13, no. 1, pp. 77–89, 1990.

110. Lieber, R. L., and J. Fridén, "Musculoskeletal balance of the human wrist elucidated using intraoperative laser diffraction," *Journal of Electromyography and Kinesiology*, Vol. 8, no. 2, pp. 93–100, 1998.

111. Mathewson, M. A., S. R. Ward, H. G. Chambers, and R. L. Lieber, "High resolution muscle measurements provide insights into equinus contractures in patients with cerebral palsy," *Journal of Orthopaedic Research*, Vol. 33, no. 1, pp. 33–39, 2015.

112. O'Connor, S. M., E. J. Cheng, K. W. Young, S. R. Ward, and R. L. Lieber, "Quantification of sarcomere length distribution in whole muscle frozen sections," *Journal of Experimental Biology*, Vol. 219, no. 10, pp. 1432–1436, 2016.

113. Yucesoy, C. A., B. H. F. J. M. Koopman, H. J. Grootenboer, and P. A. Huijing, "Finite element modeling of aponeurotomy: altered intramuscular myofascial force transmission yields complex sarcomere length distributions determining acute effects," *Biomech Model Mechanobiol*, Vol. 6, pp. 227--243, July 2007.

114. Yucesoy, C. A., and P. A. Huijing, "Specifically tailored use of the finite element method to study muscular mechanics within the context of fascial integrity: The linked fiber-matrix mesh model," *International Journal for Multiscale Computational Engineering*, Vol. 10, no. 2, pp. 155--170, 2012.

115. Yucesoy, C. A., and P. A. Huijing, "Assessment by finite element modeling indicates that surgical intramuscular aponeurotomy performed closer to the tendon enhances intended acute effects in extramuscularly connected muscle," *Journal of Biomechanical Engineering*, Vol. 131, no. 2, p. 021012, 2009.

116. Kinugasa, R., D. Shin, J. Yamauchi, C. Mishra, J. A. Hodgson, V. R. Edgerton, and S. Sinha, "Phasecontrast mri reveals mechanical behavior of superficial and deep aponeuroses in human medial gastrocnemius during isometric contraction," *J. Appl. Physiol.*, Vol. 105, pp. 1312--1320, Oct. 2008.

117. Shin, D. D., J. A. Hodgson, V. R. Edgerton, and S. Sinha, "In vivo intramuscular fascicleaponeuroses dynamics of the human medial gastrocnemius during plantarflexion and dorsiflexion of the foot," *J. Appl. Physiol.*, Vol. 107, pp. 1276--1284, Oct. 2009.

118. Pappas, G. P., D. S. Asakawa, S. L. Delp, F. E. Zajac, and J. E. Drace, "Nonuniform shortening in the biceps brachii during elbow flexion," *J. Appl. Physiol.*, Vol. 92, pp. 2381--2389, June 2002.

119. Blemker, S. S., P. M. Pinsky, and S. L. Delp, "A 3d model of muscle reveals the causes of nonuniform strains in the biceps brachii," *J Biomech*, Vol. 38, pp. 657--665, Apr. 2005.

120. Schenk, P., T. Siebert, P. Hiepe, D. Güllmar, J. R. Reichenbach, C. Wick, R. Blickhan, and M. Böl, "Determination of three-dimensional muscle architectures: validation of the dti-based fiber tractography method by manual digitization," *Journal of Anatomy*, Vol. 223, pp. 61–68, 2022/07/21 2013.

121. Lansdown, D. A., Z. Ding, M. Wadington, J. L. Hornberger, and B. M. Damon, "Quantitative diffusion tensor mri-based fiber tracking of human skeletal muscle," *Journal of Applied Physiology*, Vol. 103, pp. 673–681, 2022/07/21 2007.

122. Bolsterlee, B., H. E. J. D. Veeger, F. C. T. van der Helm, S. C. Gandevia, and R. D. Herbert, "Comparison of measurements of medial gastrocnemius architectural parameters from ultrasound and diffusion tensor images," *J Biomech*, Vol. 48, pp. 1133--1140, Apr. 2015.

123. Felton, S. M., T. A. Gaige, T. Benner, R. Wang, T. G. Reese, V. J. Wedeen, and R. J. Gilbert, "Associating the mesoscale fiber organization of the tongue with local strain rate during swallowing," *Journal of Biomechanics*, Vol. 41, no. 8, pp. 1782--1789, 2008.

124. Englund, E. K., C. P. Elder, Q. Xu, Z. Ding, and B. M. Damon, "Combined diffusion and strain tensor mri reveals a heterogeneous, planar pattern of strain development during isometric muscle contraction," *Am. J. Physiol. Regul. Integr. Comp. Physiol.*, Vol. 300, pp. R1079--1090, May 2011.

125. Wüst, R. C. I., C. I. Morse, A. De Haan, D. A. Jones, and H. Degens, "Sex differences in contractile properties and fatigue resistance of human skeletal muscle," *Experimental Physiology*, Vol. 93, pp. 843–850, 2022/07/21 2008.

126. Garland, S. J., R. M. Enoka, L. P. Serrano, and G. A. Robinson, "Behavior of motor units in human biceps brachii during a submaximal fatiguing contraction," *Journal of Applied Physiology*, Vol. 76, pp. 2411–2419, 2022/07/21 1994.

127. Weide, G., P. A. Huijing, J. C. Maas, J. G. Becher, J. Harlaar, and R. T. Jaspers, "Medial gastrocnemius muscle growth during adolescence is mediated by increased fascicle diameter rather than by longitudinal fascicle growth," *Journal of Anatomy*, Vol. 226, pp. 530–541, 2022/07/21 2015.

128. Thirion, J. P., "Image matching as a diffusion process: an analogy with maxwell's demons," *Med Image Anal*, Vol. 2, pp. 243--260, Sept. 1998.

129. *MRI modalitiy transformation in demon registration*, 2009.

130. Gallichan, D., J. Scholz, A. Bartsch, T. E. Behrens, M. D. Robson, and K. L. Miller, "Addressing a systematic vibration artifact in diffusionweighted mri," *Hum Brain Mapp*, Vol. 31, pp. 193--202, Feb. 2010.

131. Tench, C., P. Morgan, M. Wilson, and L. Blumhardt, "White matter mapping using diffusion tensor mri," *Magnetic Resonance in Medicine: An Official Journal of the International Society for Magnetic Resonance in Medicine*, Vol. 47, no. 5, pp. 967–972, 2002.

132. Yoldemir, B., B. Acar, Z. Firat, and O. Kilickesmez, "Smt: A reliability based interactive dti tractography algorithm," *IEEE Transactions on Medical Imaging*, Vol. 31, no. 10, pp. 1929–1940, 2012.

133. Froeling, M., A. J. Nederveen, D. F. R. Heijtel, A. Lataster, C. Bos, K. Nicolay, M. Maas, M. R. Drost, and G. J. Strijkers, "Diffusiontensor mri reveals the complex muscle architecture of the human forearm," *J Magn Reson Imaging*, Vol. 36, pp. 237--248, July 2012.

134. Descoteaux, M., R. Deriche, T. R. Knösche, and A. Anwander, "Deterministic and probabilistic tractography based on complex fibre orientation distributions," *IEEE Trans Med Imaging*, Vol. 28, pp. 269--286, Feb. 2009.

135. Chow, R. S., M. K. Medri, D. C. Martin, R. N. Leekam, A. M. Agur, and N. H. McKee, "Sonographic studies of human soleus and gastrocnemius muscle architecture: gender variability," *Eur. J. Appl. Physiol.*, Vol. 82, pp. 236--244, June 2000.

136. Fedorov, A., R. Beichel, J. KalpathyCramer, J. Finet, J.-C. FillionRobin, S. Pujol, C. Bauer, D. Jennings, F. Fennessy, M. Sonka, J. Buatti, S. Aylward, J. V. Miller, S. Pieper, and R. Kikinis, "3d slicer as an image computing platform for the quantitative imaging network," *Magn Reson Imaging*, Vol. 30, pp. 1323--1341, Nov. 2012.

137. Moglo, K. E., and A. ShiraziAdl, "Cruciate coupling and screwhome mechanism in passive knee joint during extensionflexion," *J Biomech*, Vol. 38, pp. 1075--1083, May 2005.

138. Wolf, S. L., and J. H. Kim, "Morphological analysis of the human tibialis anterior and medial gastrocnemius muscles," *Cells Tissues Organs*, Vol. 158, no. 4, pp. 287–295, 1997.

139. Henneman, E., "The size-principle: a deterministic output emerges from a set of probabilistic connections," *Journal of Experimental Biology*, Vol. 115, pp. 105–112, 7/21/2022 1985.

140. Garnett, R. A., M. J. O'Donovan, J. A. Stephens, and A. Taylor, "Motor unit organization of human medial gastrocnemius.," *The Journal of Physiology*, Vol. 287, pp. 33–43, 2022/07/21 1979.

141. Johnson, M. A., J. Polgar, D. Weightman, and D. Appleton, "Data on the distribution of fibre types in thirty-six human muscles: An autopsy study," *Journal of the Neurological Sciences*, Vol. 18, no. 1, pp. 111–129, 1973.

142. Vieira, T. M. M., I. D. Loram, S. Muceli, R. Merletti, and D. Farina, "Postural activation of the human medial gastrocnemius muscle: are the muscle units spatially localised?," *The Journal of Physiology*, Vol. 589, pp. 431–443, 2022/07/21 2011.

143. Avancini, C., L. F. de Oliveira, L. L. Menegaldo, and T. M. Vieira, "Variations in the spatial distribution of the amplitude of surface electromyograms are unlikely explained by changes in the length of medial gastrocnemius fibres with knee joint angle," *PLOS ONE*, Vol. 10, pp. e0126888–, 05 2015.

144. Hodson-Tole, E. F., J. M. Wakeling, and T. J. Dick, "Passive muscle-tendon unit gearing is joint dependent in human medial gastrocnemius," *Frontiers in physiology*, Vol. 7, p. 95, 2016.

145. Gallina, A., R. Merletti, and T. M. M. Vieira, "Are the myoelectric manifestations of fatigue distributed regionally in the human medial gastrocnemius muscle?," *Journal of Electromyography and Kinesiology*, Vol. 21, no. 6, pp. 929–938, 2011.

146. Hodson-Tole, E. F., I. D. Loram, and T. M. M. Vieira, "Myoelectric activity along human gastrocnemius medialis: Different spatial distributions of postural and electrically elicited surface potentials," *Journal of Electromyography and Kinesiology*, Vol. 23, no. 1, pp. 43–50, 2013.

147. Huxley, H. E., "The mechanism of muscular contraction," *Science*, Vol. 164, pp. 1356--1365, June 1969.

148. Meijer, H. J. M., G. C. Baan, and P. A. Huijing, "Myofascial force transmission is increasingly important at lower forces: firing frequency-related length–force characteristics of rat extensor digitorum longus," *Acta Physiologica*, Vol. 186, pp. 185–195, 2022/07/21 2006.

149. Ratkevičius, A., M. Mizuno, E. Povilonis, and B. Quistorff, "Energy metabolism of the gastrocnemius and soleus muscles during isometric voluntary and electrically induced contractions in man," *The Journal of Physiology*, Vol. 507, no. Pt 2, p. 593, 1998.

150. Oda, T., H. Kanehisa, K. Chino, T. Kurihara, T. Nagayoshi, T. Fukunaga, and Y. Kawakami, "In vivo behavior of muscle fascicles and tendinous tissues of human gastrocnemius and soleus muscles during twitch contraction," *Journal of Electromyography and Kinesiology*, Vol. 17, no. 5, pp. 587–595, 2007.

151. Dalmau-Pastor, M., B. Fargues-Polo, D. Casanova-Martínez, J. Vega, and P. Golanó, "Anatomy of the triceps surae: A pictorial essay," *Foot and Ankle Clinics*, Vol. 19, no. 4, pp. 603–635, 2014.

152. Cummins, E., and B. Anson, "The structure of the calcaneal tendon (of achilles) in relation to orthopedic surgery, with additional observations on the plantaris muscle," *Surgery, gynecology & obstetrics*, Vol. 83, pp. 107–116, 1946.

153. Maas, H., and T. G. Sandercock, "Are skeletal muscles independent actuators? force transmission from soleus muscle in the cat," *J. Appl. Physiol.*, Vol. 104, pp. 1557--1567, June 2008.

154. Tian, M., R. D. Herbert, P. Hoang, S. C. Gandevia, and L. E. Bilston, "Myofascial force transmission between the human soleus and gastrocnemius muscles during passive knee motion," *J. Appl. Physiol.*, Vol. 113, pp. 517--523, Aug. 2012.

155. Mathur, A. B., A. M. Collinsworth, W. M. Reichert, W. E. Kraus, and G. A. Truskey, "Endothelial, cardiac muscle and skeletal muscle exhibit different viscous and elastic properties as determined by atomic force microscopy," *Journal of Biomechanics*, Vol. 34, no. 12, pp. 1545–1553, 2001.

156. Yucesoy, C. A., B. Koopman, G. Baan, H. Grootenboer, and P. Huijing, "Extramuscular myofascial force transmission: experiments and finite element modeling," *Archives of physiology and biochemistry*, Vol. 111, no. 4, pp. 377–388, 2003.

157. Yucesoy, C. A., G. Baan, and P. A. Huijing, "Epimuscular myofascial force transmission occurs in the rat between the deep flexor muscles and their antagonistic muscles," *J Electromyogr Kinesiol*, Vol. 20, pp. 118--126, Feb. 2010.

158. Maas, H., G. C. Baan, P. A. Huijing, C. A. Yucesoy, B. H. Koopman, and H. J. Grootenboer, "The relative position of edl muscle affects the length of sarcomeres within muscle fibers: experimental results and finiteelement modeling," *J Biomech Eng*, Vol. 125, pp. 745--753, Oct. 2003.

159. Wakeling, J. M., "The recruitment of different compartments within a muscle depends on the mechanics of the movement," *Biology Letters*, Vol. 5, pp. 30–34, 2022/07/22 2009.

160. Ateş, F., Y. Temelli, and C. A. Yucesoy, "Intraoperative experiments show relevance of inter-antagonistic mechanical interaction for spastic muscle's contribution to joint movement disorder," *Clinical Biomechanics*, Vol. 29, no. 8, pp. 943–949, 2014.

161. Ateş, F., Y. Temelli, and C. A. Yucesoy, "The mechanics of activated semitendinosus are not representative of the pathological knee joint condition of children with cerebral palsy," *Journal of Electromyography and Kinesiology*, Vol. 28, pp. 130–136, 2016.

162. Garrett, W. E., "Muscle strain injuries," *The American Journal of Sports Medicine*, Vol. 24, pp. S2–S8, 2022/07/22 1996.

163. Shah, J. R., B. R. Shah, and A. S. Shah, "Pictorial essay: ultrasonography in tennis leg," *Indian Journal of Radiology and Imaging*, Vol. 20, no. 04, pp. 269–273, 2010.

164. Ramsey, R. W., and S. F. Street, "The isometric lengthtension diagram of isolated skeletal muscle fibers of the frog," *Journal of Cellular and Comparative Physiology*, Vol. 15, pp. 11--34, Feb. 1940.

165. Lichtwark, G. A., D. J. Farris, X. Chen, P. W. Hodges, and S. L. Delp, "Microendoscopy reveals positive correlation in multiscale length changes and variable sarcomere lengths across different regions of human muscle," *Journal of Applied Physiology*, Vol. 125, no. 6, pp. 1812–1820, 2018.

166. Moo, E. K., R. Fortuna, S. C. Sibole, Z. Abusara, and W. Herzog, "In vivo sarcomere lengths and sarcomere elongations are not uniform across an intact muscle," *Frontiers in Physiology*, Vol. 7, 2016.

167. Fiorentino, N. M., F. H. Epstein, and S. S. Blemker, "Activation and aponeurosis morphology affect in vivo muscle tissue strains near the myotendinous junction," *Journal of biomechanics*, Vol. 45, no. 4, pp. 647–652, 2012.

168. Wakeling, J. M., S. A. Ross, D. S. Ryan, B. Bolsterlee, R. Konno, S. Domínguez, and N. Nigam, "The energy of muscle contraction. i. tissue force and deformation during fixed-end contractions," *Frontiers in Physiology*, Vol. 11, p. 813, 2020.

169. Mechelli, A., C. J. Price, K. J. Friston, and J. Ashburner, "Voxel-based morphometry of the human brain: methods and applications," *Current Medical Imaging*, Vol. 1, no. 2, pp. 105–113, 2005.

170. Frisoni, G. B., C. Testa, A. Zorzan, F. Sabattoli, A. Beltramello, H. Soininen, and M. P. Laakso, "Detection of grey matter loss in mild alzheimer's disease with voxel based morphometry," *Journal of Neurology, Neurosurgery & Psychiatry*, Vol. 73, no. 6, pp. 657–664, 2002.

171. Focke, N. K., G. Helms, S. Kaspar, C. Diederich, V. Tóth, P. Dechent, A. Mohr, and W. Paulus, "Multi-site voxel-based morphometry—not quite there yet," *Neuroimage*, Vol. 56, no. 3, pp. 1164–1170, 2011.

172. Takao, H., N. Hayashi, and K. Ohtomo, "Effects of the use of multiple scanners and of scanner upgrade in longitudinal voxel,Äêbased morphometry studies," *Journal of Magnetic Resonance Imaging*, Vol. 38, no. 5, pp. 1283–1291, 2013.

173. De Bondt, T., P. Pullens, W. Van Hecke, Y. Jacquemyn, and P. M. Parizel, "Reproducibility of hormone-driven regional grey matter volume changes in women using spm8 and spm12," *Brain Structure and Function*, Vol. 221, no. 9, pp. 4631–4641, 2016.

174. Rajagopalan, V., and E. P. Pioro, "Disparate voxel based morphometry (vbm) results between spm and fsl softwares in als patients with frontotemporal dementia: which vbm results to consider?," *BMC neurology*, Vol. 15, no. 1, pp. 1–7, 2015.

175. Tudorascu, D. L., H. T. Karim, J. M. Maronge, L. Alhilali, S. Fakhran, H. J. Aizenstein, J. Muschelli, and C. M. Crainiceanu, "Reproducibility and bias in healthy brain segmentation: comparison of two popular neuroimaging platforms," *Frontiers in neuroscience*, Vol. 10, p. 503, 2016.

176. Jones, D. K., M. R. Symms, M. Cercignani, and R. J. Howard, "The effect of filter size on vbm analyses of dt-mri data," *Neuroimage*, Vol. 26, no. 2, pp. 546–554, 2005.

177. Radua, J., E. J. Canales-Rodríguez, E. Pomarol-Clotet, and R. Salvador, "Validity of modulation and optimal settings for advanced voxel-based morphometry," *Neuroimage*, Vol. 86, pp. 81–90, 2014.

178. Gorgolewski, K. J., F. Alfaro-Almagro, T. Auer, P. Bellec, M. Capotă, M. M. Chakravarty, N. W. Churchill, A. L. Cohen, R. C. Craddock, and G. A. Devenyi, "Bids apps: Improving ease of use, accessibility, and reproducibility of neuroimaging data analysis methods," *PLoS computational biology*, Vol. 13, no. 3, p. e1005209, 2017.

179. Poldrack, R. A., C. I. Baker, J. Durnez, K. J. Gorgolewski, P. M. Matthews, M. R. Munafò, T. E. Nichols, J.-B. Poline, E. Vul, and T. Yarkoni, "Scanning the horizon: towards transparent and reproducible neuroimaging research," *Nature reviews neuroscience*, Vol. 18, no. 2, pp. 115–126, 2017.

180. Ridgway, G. R., S. M. D. Henley, J. D. Rohrer, R. I. Scahill, J. D. Warren, and N. C. Fox, "Ten simple rules for reporting voxel-based morphometry studies," *Neuroimage*, Vol. 40, no. 4, pp. 1429–1435, 2008.

181. Tristán-Vega, A., and S. Aja-Fernández, "Dwi filtering using joint information for dti and hardi," *Medical image analysis*, Vol. 14, no. 2, pp. 205–218, 2010.

182. Norton, I., W. I. Essayed, F. Zhang, S. Pujol, A. Yarmarkovich, A. J. Golby, G. Kindlmann, D. Wassermann, R. S. J. Estepar, Y. Rathi, S. Pieper, R. Kikinis, H. J. Johnson, C.-F. Westin, and L. J. O'Donnell, "Slicerdmri: Open source diffusion mri software for brain cancer research," *Cancer Research*, Vol. 77, pp. e101–e103, 7/23/2022 2017.

183. Fedorov, A., R. Beichel, J. Kalpathy-Cramer, J. Finet, J. C. Fillion-Robin, S. Pujol, C. Bauer, D. Jennings, F. Fennessy, M. Sonka, J. Buatti, S. Aylward, J. V. Miller, S. Pieper, and R. Kikinis, "3d slicer as an image computing platform for the quantitative imaging network," *Magnetic Resonance Imaging*, Vol. 30, no. 9, pp. 1323–1341, 2012.

184. Yoldemir, B., B. Acar, Z. Firat, and Ö. Kiliçkesmez, "Smt: A reliability based interactive dti tractography algorithm," *IEEE Transactions on Medical Imaging*, Vol. 31, no. 10, pp. 1929–1940, 2012.

185. Leys, C., C. Ley, O. Klein, P. Bernard, and L. Licata, "Detecting outliers: Do not use standard deviation around the mean, use absolute deviation around the median," *Journal of experimental social psychology*, Vol. 49, no. 4, pp. 764–766, 2013.

186. Iglewicz, B., and D. C. Hoaglin, *How to detect and handle outliers*, Vol. 16, Asq Press, 1993.

187. Glira, P., N. Pfeifer, C. Briese, and C. Ressl, "A correspondence framework for als strip adjustments based on variants of the icp algorithm," *PFG Photogrammetrie, Fernerkundung, Geoinformation*, pp. 275–289, 2015.

188. Terrell, G. R., and D. W. Scott, "Variable kernel density estimation," *The Annals of Statistics*, pp. 1236–1265, 1992.

189. Kluyver, T., B. Ragan-Kelley, F. Pérez, B. E. Granger, M. Bussonnier, J. Frederic, K. Kelley, J. B. Hamrick, J. Grout, and S. Corlay, *Jupyter Notebooks-a publishing format for reproducible computational workflows*, Vol. 2016, 2016.

190. DOKSUM, K., "Some graphical methods in statistics: A review and some extensions," *Statistica Neerlandica*, Vol. 31, no. 2, pp. 53–68, 1977.

191. Rousselet, G., C. Pernet, and R. R. Wilcox, "A practical introduction to the bootstrap: a versatile method to make inferences by using data-driven simulations," 2019.

192. Hyndman, R. J., and Y. Fan, "Sample quantiles in statistical packages," *The American Statistician*, Vol. 50, no. 4, pp. 361–365, 1996.

193. Benjamini, Y., and Y. Hochberg, "Controlling the false discovery rate: a practical and powerful approach to multiple testing," *Journal of the Royal statistical society: series B (Methodological)*, Vol. 57, no. 1, pp. 289–300, 1995.

194. Karakuzu, A., "Reproducibility resources for fiber direction strain heterogeneity analysis," *Open Science Framework*, p. https://doi.org/10.17605/OSF.IO/2G9PH, 2021.

195. Nath, V., K. G. Schilling, P. Parvathaneni, Y. Huo, J. A. Blaber, A. E. Hainline, M. Barakovic, D. Romascano, J. Rafael,ÄêPatino, and M. Frigo, "Tractography reproducibility challenge with empirical data (traced): the 2017 ismrm diffusion study group challenge," *Journal of Magnetic Resonance Imaging*, Vol. 51, no. 1, pp. 234–249, 2020.

196. *On the reproducibility of MRI-DTI based passive length changes and the added implications of quantitative MRI*, (Calgary, Alberta, Canada), 2019.

197. Arnold, B., L. Bowler, S. Gibson, P. Herterich, R. Higman, A. Krystalli, A. Morley, M. O'Reilly, and K. Whitaker, "The turing way: a handbook for reproducible data science," *Zenodo*, 2019.

198. Kiar, G., "This is your brain on disk: The impact of numerical instabilities in neuroscience," 2021.

199. Gozubuyuk, O. B., A. Karakuzu, U. Pamuk, and C. A. Yucesoy, "The role of intra-,Äêand epimuscular fasciae beyond being passive structural elements: Mri analyses indicate that they interfere with, and affect muscle's active mechanics," *Journal of Bodywork and Movement Therapies*, Vol. 22, no. 4, pp. 852–853, 2018.

200. Karakuzu, A., U. Pamuk, C. Ozturk, B. Acar, and C. A. Yucesoy, "Magnetic resonance and diffusion tensor imaging analyses indicate heterogeneous strains along human medial gastrocnemius fascicles caused by submaximal plantar-flexion activity," *Journal of Biomechanics*, Vol. 57, pp. 69–78, 2017.

201. Gijsbertse, K., R. Goselink, S. Lassche, M. Nillesen, A. Sprengers, N. Verdonschot, N. van Alfen, and C. De Korte, "Ultrasound imaging of muscle contraction of the tibialis anterior in patients with facioscapulohumeral dystrophy," *Ultrasound in medicine & biology*, Vol. 43, no. 11, pp. 2537–2545, 2017.

202. Pamuk, U., A. O. Cankaya, and C. A. Yucesoy, "Principles of the mechanism for epimuscular myofascial loads leading to non-uniform strain distributions along muscle fiber direction: Finite element modeling," *Frontiers in Physiology*, Vol. 11, 2020.

203. Klein, A., J. Andersson, B. A. Ardekani, J. Ashburner, B. Avants, M.-C. Chiang, G. E. Christensen, D. L. Collins, J. Gee, P. Hellier, J. H. Song, M. Jenkinson, C. Lepage, D. Rueckert, P. Thompson, T. Vercauteren, R. P. Woods, J. J. Mann, and R. V. Parsey, "Evaluation of 14 nonlinear deformation algorithms applied to human brain mri registration," *NeuroImage*, Vol. 46, no. 3, pp. 786–802, 2009.

204. Bolsterlee, B., T. Finni, A. D'Souza, J. Eguchi, E. C. Clarke, and R. D. Herbert, "Three-dimensional architecture of the whole human soleus muscle in vivo," *PeerJ*, Vol. 6, p. e4610, 2018.

205. Turkoglu, A. N., P. A. Huijing, and C. A. Yucesoy, "Mechanical principles of effects of botulinum toxin on muscle length-force characteristics: An assessment by finite element modeling," *Journal of Biomechanics*, Vol. 47, no. 7, pp. 1565–1571, 2014.

206. Steegen, S., F. Tuerlinckx, A. Gelman, and W. Vanpaemel, "Increasing transparency through a multiverse analysis," *Perspectives on Psychological Science*, Vol. 11, no. 5, pp. 702–712, 2016.

207. The Turing Way Community, B. Arnold, L. Bowler, S. Gibson, P. Herterich, R. Higman, A. Krystalli, A. Morley, M. O'Reilly, and K. Whitaker, "The turing way: A handbook for reproducible data science," 2019.

208. Weinberger, D. R., and E. Radulescu, "Structural magnetic resonance imaging all over again," *JAMA psychiatry*, Vol. 78, no. 1, pp. 11–12, 2021.

209. Novikov, D. S., V. G. Kiselev, and S. N. Jespersen, "On modeling," *Magnetic resonance in medicine*, Vol. 79, no. 6, pp. 3172–3193, 2018.

210. Bratton, C. B., A. Hopkins, and J. W. Weinberg, "Nuclear magnetic resonance studies of living muscle," *Science*, Vol. 147, no. 3659, pp. 738–739, 1965.

211. Louie, E. A., D. F. Gochberg, M. D. Does, and B. M. Damon, "Transverse relaxation and magnetization transfer in skeletal muscle: effect of ph," *Magnetic Resonance in Medicine: An Official Journal of the International Society for Magnetic Resonance in Medicine*, Vol. 61, no. 3, pp. 560–569, 2009.

212. Arpan, I., S. C. Forbes, D. J. Lott, C. R. Senesac, M. J. Daniels, W. T. Triplett, J. K. Deol, H. L. Sweeney, G. A. Walter, and K. Vandenborne, "T2 mapping provides multiple approaches for the characterization of muscle involvement in neuromuscular diseases: a cross,Äêsectional study of lower leg muscles in 5–15,Äêyear,Äêold boys with duchenne muscular dystrophy," *NMR in biomedicine*, Vol. 26, no. 3, pp. 320–328, 2013.

213. Saab, G., R. T. Thompson, and G. D. Marsh, "Multicomponent t2 relaxation of in vivo skeletal muscle," *Magnetic Resonance in Medicine: An Official Journal of the International Society for Magnetic Resonance in Medicine*, Vol. 42, no. 1, pp. 150–157, 1999.

214. Cole, W. C., A. D. Leblanc, and S. G. Jhingran, "The origin of biexponential t2 relaxation in muscle water," *Magnetic resonance in medicine*, Vol. 29, no. 1, pp. 19–24, 1993.

215. Araujo, E. C. A., Y. Fromes, and P. G. Carlier, "New insights on human skeletal muscle tissue compartments revealed by in vivo t2 nmr relaxometry," *Biophysical Journal*, Vol. 106, no. 10, pp. 2267–2274, 2014.

216. Saab, G., R. T. Thompson, and G. D. Marsh, "Effects of exercise on muscle transverse relaxation determined by mr imaging and in vivo relaxometry," *Journal of Applied Physiology*, Vol. 88, pp. 226–233, 2022/08/05 2000.

217. Saab, G., G. D. Marsh, M. A. Casselman, and R. T. Thompson, "Changes in human muscle transverse relaxation following short-term creatine supplementation," *Experimental Physiology*, Vol. 87, no. 3, pp. 383–389, 2002.

218. *BOLD magnetic resonance imaging of skeletal muscle*, Vol. 7, Copyright©2002 by Thieme Medical Publishers, Inc., 333 Seventh Avenue, New . . . , 2003.

219. Jacobi, B., G. Bongartz, S. Partovi, A.-C. Schulte, M. Aschwanden, A. B. Lumsden, M. G. Davies, M. Loebe, G. P. Noon, S. Karimi, J. K. Lyo, D. Staub, R. W. Huegli, and D. Bilecen, "Skeletal muscle bold mri: From underlying physiological concepts to its usefulness in clinical conditions," *Journal of Magnetic Resonance Imaging*, Vol. 35, pp. 1253–1265, 2022/08/05 2012.

220. Bulte, D. P., J. Alfonsi, S. Bells, and M. D. Noseworthy, "Vasomodulation of skeletal muscle bold signal," *Journal of Magnetic Resonance Imaging: An Official Journal of the International Society for Magnetic Resonance in Medicine*, Vol. 24, no. 4, pp. 886–890, 2006.

221. Wigmore, D. M., B. M. Damon, D. M. Pober, and J. A. Kent-Braun, "Mri measures of perfusion-related changes in human skeletal muscle during progressive contractions," *Journal of Applied Physiology*, Vol. 97, no. 6, pp. 2385–2394, 2004.

222. Li, K., R. D. Dortch, E. B. Welch, N. D. Bryant, A. K. W. Buck, T. F. Towse, D. F. Gochberg, M. D. Does, B. M. Damon, and J. H. Park, "Multi-parametric mri characterization of healthy human thigh muscles at 3.0 t –relaxation, magnetization transfer, fat/water, and diffusion tensor imaging," *NMR in Biomedicine*, Vol. 27, pp. 1070–1084, 2022/08/05 2014.

223. Bryant, N. D., K. Li, M. D. Does, S. Barnes, D. F. Gochberg, T. E. Yankeelov, J. H. Park, and B. M. Damon, "Multi,Äêparametric mri characterization of inflammation in murine skeletal muscle," *NMR in biomedicine*, Vol. 27, no. 6, pp. 716–725, 2014.

224. Polak, J. F., F. A. Jolesz, and D. F. Adams, "Magnetic resonance imaging of skeletal muscle. prolongation of t1 and t2 subsequent to denervation.," *Investigative radiology*, Vol. 23, no. 5, pp. 365–369, 1988.

225. Varghese, J., D. Scandling, R. Joshi, A. Aneja, J. Craft, S. V. Raman, S. Rajagopalan, O. P. Simonetti, and G. Mihai, "Rapid assessment of quantitative t1, t2 and t2* in lower extremity muscles in response to maximal treadmill exercise," *NMR in Biomedicine*, Vol. 28, pp. 998–1008, 2022/08/05 2015.

226. Bull, S., S. K. White, S. K. Piechnik, A. S. Flett, V. M. Ferreira, M. Loudon, J. M. Francis, T. D. Karamitsos, B. D. Prendergast, M. D. Robson, S. Neubauer, J. C. Moon, and S. G. Myerson, "Human non-contrast t1 values and correlation with histology in diffuse fibrosis," *Heart*, Vol. 99, p. 932, 07 2013.

227. Hafyane, T., A. Karakuzu, C. Duquette, F.-P. Mongeon, J. Cohen-Adad, M. Jerosch-Herold, M. G. Friedrich, and N. Stikov, "Let's talk about cardiac t1 mapping," *bioRxiv*, p. 343079, 2018.

228. Gold, G. E., E. Han, J. Stainsby, G. Wright, J. Brittain, and C. Beaulieu, "Musculoskeletal mri at 3.0 t: relaxation times and image contrast," *American Journal of Roentgenology*, Vol. 183, no. 2, pp. 343–351, 2004.

229. Karakuzu, A., L. Biswas, J. Cohen,ÄêAdad, and N. Stikov, "Vendor,Äêneutral sequences and fully transparent workflows improve inter,Äêvendor reproducibility of quantitative mri," *Magnetic Resonance in Medicine*, Vol. 88, no. 3, pp. 1212–1228, 2022.

230. Novikov, D. S., E. Fieremans, S. N. Jespersen, and V. G. Kiselev, "Quantifying brain microstructure with diffusion mri: Theory and parameter estimation," *NMR in Biomedicine*, Vol. 32, no. 4, p. e3998, 2019.

231. Naughton, N. M., and J. G. Georgiadis, "Global sensitivity analysis of skeletal muscle dmri metrics: Effects of microstructural and pulse parameters," *Magnetic Resonance in Medicine*, Vol. 83, pp. 1458–1470, 2022/07/30 2020.

232. Porcari, P., M. G. Hall, C. A. Clark, E. Greally, V. Straub, and A. M. Blamire, "The effects of ageing on mouse muscle microstructure: a comparative study of time-dependent diffusion mri and histological assessment," *NMR in Biomedicine*, Vol. 31, p. e3881, 2022/07/30 2018.

233. Fieremans, E., G. Lemberskiy, J. Veraart, E. E. Sigmund, S. Gyftopoulos, and D. S. Novikov, "In vivo measurement of membrane permeability and myofiber size in human muscle using time-dependent diffusion tensor imaging and the random permeable barrier model," *NMR in Biomedicine*, Vol. 30, p. e3612, 2022/07/30 2017.

234. Lemberskiy, G., T. Feiweier, S. Gyftopoulos, L. Axel, D. S. Novikov, and E. Fieremans, "Assessment of myofiber microstructure changes due to atrophy and recovery with time-dependent diffusion mri," *NMR in Biomedicine*, Vol. 34, p. e4534, 2022/07/30 2021.

235. *Comparison of dMRI models for skeletal muscle microstructure estimation with numerical simulations and porcine phantom*, 2019.

236. Henkelman, R., G. Stanisz, and S. Graham, "Magnetization transfer in mri: a review," *NMR in Biomedicine: An International Journal Devoted to the Development and Application of Magnetic Resonance In Vivo*, Vol. 14, no. 2, pp. 57–64, 2001.

237. Wolff, S. D., and R. S. Balaban, "Magnetization transfer imaging: practical aspects and clinical applications.," *Radiology*, Vol. 192, no. 3, pp. 593–599, 1994.

238. Sinclair, C., J. Morrow, M. Miranda, I. Davagnanam, P. Cowley, H. Mehta, M. Hanna, M. Koltzenburg, T. Yousry, and M. Reilly, "Skeletal muscle mri magnetisation transfer ratio reflects clinical severity in peripheral neuropathies," *Journal of Neurology, Neurosurgery & Psychiatry*, Vol. 83, no. 1, pp. 29–32, 2012.

239. McDaniel, J. D., J. L. Ulmer, R. W. Prost, M. B. Franczak, S. Jaradeh, C. A. Hamilton, and L. P. Mark, "Magnetization transfer imaging of skeletal muscle in autosomal recessive limb girdle muscular dystrophy," *Journal of computer assisted tomography*, Vol. 23, no. 4, pp. 609–614, 1999.

240. *Correlation between muscle magnetization transfer ratio and muscle strength in chronic inflammatory demyelinating polyneuropathy*, 2009.

241. Zhu, X., S. Zhao, and I. Isherwood, "Magnetization transfer contrast (mtc) imaging of skeletal muscle at 0.26 tesla—changes in signal intensity following exercise," *The British Journal of Radiology*, Vol. 65, no. 769, pp. 39–43, 1992.

242. Sinclair, C. D., R. S. Samson, D. L. Thomas, N. Weiskopf, A. Lutti, J. S. Thornton, and X. Golay, "Quantitative magnetization transfer in in vivo healthy human skeletal muscle at 3 t," *Magnetic resonance in medicine*, Vol. 64, no. 6, pp. 1739–1748, 2010.

243. Ramani, A., C. Dalton, D. Miller, P. Tofts, and G. Barker, "Precise estimate of fundamental in-vivo mt parameters in human brain in clinically feasible times," *Magnetic resonance imaging*, Vol. 20, no. 10, pp. 721–731, 2002.

244. Campbell, J. S., I. R. Leppert, S. Narayanan, M. Boudreau, T. Duval, J. Cohen-Adad, G. B. Pike, and N. Stikov, "Promise and pitfalls of g-ratio estimation with mri," *Neuroimage*, Vol. 182, pp. 80–96, 2018.

245. Helms, G., H. Dathe, K. Kallenberg, and P. Dechent, "High,Äêresolution maps of magnetization transfer with inherent correction for rf inhomogeneity and t1 relaxation obtained from 3d flash mri," *Magnetic Resonance in Medicine: An Official Journal of the International Society for Magnetic Resonance in Medicine*, Vol. 60, no. 6, pp. 1396–1407, 2008.

246. Romero, I. O., and U. Sinha, "Magnetization transfer saturation imaging of human calf muscle: Reproducibility and sensitivity to regional and sex differences," *Journal of Magnetic Resonance Imaging*, Vol. 50, no. 4, pp. 1227–1237, 2019.

247. *In vivo inhomogeneous magnetization transfer (ihMT) outside the brain using radial ultra-short echo-time acquisitions*, 2019.

248. Sinha, U., V. Malis, R. Csapo, A. Moghadasi, R. Kinugasa, and S. Sinha, "Age-related differences in strain rate tensor of the medial gastrocnemius muscle during passive plantarflexion and active isometric contraction using velocity encoded mr imaging: Potential index of lateral force transmission," *Magnetic Resonance in Medicine*, Vol. 73, pp. 1852–1863, 2022/08/04 2015.

249. Oguz, I., M. Farzinfar, J. Matsui, F. Budin, Z. Liu, G. Gerig, H. J. Johnson, and M. Styner, "Dtiprep: quality control of diffusion-weighted images," *Frontiers in neuroinformatics*, Vol. 8, p. 4, 2014.

250. Bastin, M. E., "Correction of eddy current-induced artefacts in diffusion tensor imaging using iterative cross-correlation," *Magnetic resonance imaging*, Vol. 17, no. 7, pp. 1011–1024, 1999.

251. Fritzsche, K. H., P. F. Neher, I. Reicht, T. van Bruggen, C. Goch, M. Reisert, M. Nolden, S. Zelzer, H.-P. Meinzer, and B. Stieltjes, "Mitk diffusion imaging," *Methods of information in medicine*, Vol. 51, no. 05, pp. 441–448, 2012.

252. Karakuzu, A., M. Boudreau, T. Duval, T. Boshkovski, I. Leppert, J.-F. Cabana, I. Gagnon, P. Beliveau, G. Pike, J. Cohen-Adad, and N. Stikov, "qMRLab: Quantitative MRI analysis, under one umbrella," *Journal of Open Source Software*, Vol. 5, p. 2343, Sept. 2020.

253. Klein, S., M. Staring, K. Murphy, M. A. Viergever, and J. P. Pluim, "Elastix: a toolbox for intensity-based medical image registration," *IEEE transactions on medical imaging*, Vol. 29, no. 1, pp. 196–205, 2009.

254. Ger, R. B., J. Yang, Y. Ding, M. C. Jacobsen, C. E. Cardenas, C. D. Fuller, R. M. Howell, H. Li, R. J. Stafford, S. Zhou, and L. E. Court, "Synthetic head and neck and phantom images for determining deformable image registration accuracy in magnetic resonance imaging," *Medical Physics*, Vol. 45, pp. 4315--4321, Sept. 2018.

255. Clark, K., B. Vendt, K. Smith, J. Freymann, J. Kirby, P. Koppel, S. Moore, S. Phillips, D. Maffitt, M. Pringle, L. Tarbox, and F. Prior, "The cancer imaging archive (tcia): Maintaining and operating a public information repository," *Journal of Digital Imaging*, Vol. 26, pp. 1045--1057, Dec. 2013.

256. Ger, R., J. Yang, Y. Ding, M. Jacobsen, C. Cardenas, C. Fuller, R. Howell, H. Li, R. J. Stafford, S. Zhou, and L. Court, "Data from synthetic and phantom mr images for determining deformable image registration accuracy (mridir)," 2018.

257. Yoshitake, Y., D. Uchida, K. Hirata, D. L. Mayfield, and H. Kanehisa, "Mechanical interaction between neighboring muscles in human upper limb: Evidence for epimuscular myofascial force transmission in humans," *J Biomech*, Vol. 74, pp. 150--155, June 2018.

258. Salazar-Llano, L., and C. Bayona-Roa, "Visualization of the strain-rate state of a data cloud: Analysis of the temporal change of an urban multivariate description," *Applied Sciences*, Vol. 9, no. 14, p. 2920, 2019.